David Bernhard Steffelbauer, BSc

Andreev-Reflection in One-Dimensional Quantum Systems

MASTER THESIS

For obtaining the academic degree
Diplom-Ingenieur

Master Programme of
Technical Physics

Graz University of Technology

Graz University of Technology

Supervisor:
Ao.Univ.-Prof. Dipl.-Phys. Dr.rer.nat. Hans Gerd Evertz
Institute of Theoretical and Computational Physics

Graz, January 2014

TU Graz
Graz University of Technology
Senat

Deutsche Fassung:
Beschluss der Curricula-Kommission für Bachelor-, Master- und Diplomstudien vom 10.11.2008
Genehmigung des Senates am 1.12.2008

EIDESSTATTLICHE ERKLÄRUNG

Ich erkläre an Eides statt, dass ich die vorliegende Arbeit selbstständig verfasst, andere als die angegebenen Quellen/Hilfsmittel nicht benutzt, und die den benutzten Quellen wörtlich und inhaltlich entnommenen Stellen als solche kenntlich gemacht habe.

Graz, am …………………………… ………………………………………………..
(Unterschrift)

Englische Fassung:

STATUTORY DECLARATION

I declare that I have authored this thesis independently, that I have not used other than the declared sources / resources, and that I have explicitly marked all material which has been quoted either literally or by content from the used sources.

…………………………… ………………………………………………..
date (signature)

To Stephanie

Abstract

One-dimensional strongly correlated quantum systems have become a popular playground for theorists in the past, because of their sometimes completely different behavior compared to systems in higher dimensions. For example, superconductivity does not occur in one dimension according to the Mermin-Wagner theorem. On the other hand, there exist effects only observable in one-dimensional systems such as spin charge separation.

In this master's thesis, the dynamical behavior of one-dimensional quantum systems with open boundary conditions is simulated. Groundstates of the systems are obtained by the density matrix renormalization group algorithm, nowadays the most precise and efficient method, and time evolution is computed by time-evolving block decimation. Both methods can be represented as matrix product state approaches.

First, spin charge separation is investigated for a repulsive Hubbard model and compared to analytically obtained solutions from the famous Bethe ansatz. The results show good agreement.

Thereafter, simulations of Andreev reflection, an effect occurring for electrons crossing a normal metal to superconductor boundary. Since there exist no superconductors in one dimension, the observation of this special kind of reflection in one-dimensional systems is astonishing. Andreev reflection is simulated and observed for several model systems, containing spinless fermions, both repulsive and attractive Hubbard model and the s-wave Bardeen-Cooper-Schrieffer Hamiltonian.

Kurzfassung

Stark korrelierte Quantensysteme in einer Dimension entwickelten sich in der Vergangenheit zu einem beliebten Spielplatz für Theoretiker. Grund dafür ist ihr manchmal komplett unterschiedliches Verhalten im Vergleich zu Systemen in höheren Dimensionen. Supraleitung zum Beispiel taucht gemäß dem Mermin Wagner Theorem in einer Dimension nicht auf. Auf der anderen Seite existieren Effekte, die nur in eindimensionalen Systemen beobachtbar sind, wie die Spin-Ladungstrennung.

In dieser Masterarbeit wird das dynamische Verhalten von eindimensionalen Quantensystemen mit offenen Randbedingungen simuliert. Die Grundzustände der Systeme wurden mit Hilfe der Dichte-Matrix Renormierungsgruppe, dem heutzutage genauesten und leistungsfähigsten Algorithmus, berechnet. Für die Zeitentwicklung der Zustände wurde der Time-Evolving-Block-Decimation Algorithmus verwendet. Beide Algorithmen sind durch Matrix Produkt Zustände darstellbar.

Zuerst wurde die Spin-Ladungstrennung für ein repulsives Hubbardmodell untersucht. Die Simulationen wurden mit analytisch berechneten Ergebnissen, die aus dem Betheansatz erhaltenen wurden, verglichen und zeigten gute Übereinstimmung.

Danach folgen Simulationen zur Andreev-Reflexion, ein Effekt der für Elektronen, die eine Normalleiter-Supraleiter Grenzflächen passieren, auftritt. Überraschenderweise ist diese Art der Reflexion in einer Dimension beobachtbar, obwohl Supraleiter hier nicht existieren. Die Andreev-Reflektion wurde für verschiedenste Modellsysteme simuliert. Bei den untersuchten Systemen handelt es sich um Fermionen ohne Spin, sowohl das repulsive als auch das attraktive Hubbardmodell und das Bardeen-Cooper-Schrieffer Supraleitermodell.

Contents

1 Introduction

The rich physics of low dimensional strongly correlated quantum systems has attracted the attention of many theorists over the last half century. Although low- and especially one-dimensional systems behave highly different than one expects for normal systems in higher dimensions, the models are on the one hand simple enough to provide complete solutions, but on the other hand at least complex enough to contain various physical effects.

Even though the systems are only of one dimension they are still analytically and numerically hard to study. If one wants to analyze correlation effects, which emerge for example in spin chains, frustrated magnets or high temperature superconductors, perturbation theory fails due to the presence of strong interactions. Concerning the different behavior of one-dimensional systems, new theoretical tools have been developed in the 1970's, especially the Luttinger liquid theory, which is the one-dimensional counterpart to the three dimensional theory of Fermi-liquids. For some one-dimensional systems, solutions based on the Bethe ansatz could be found [1, 2], but regrettably not for all.

Also, numerical algorithms like exact diagonalization, quantum Monte Carlo (QMC), series expansion or coupled cluster methods were developed to gain deeper insight in these strongly correlated systems. Unfortunately these algorithms are either of limited precision, or the computational effort depends strongly on system size.

Suddenly in the year 1992 with Steve R. White's Density Matrix Renormalization Group (DMRG)[3, 4] everything changed, at least for one-dimensional systems. DMRG is currently the most powerful numerical method in the study of one-dimensional quantum lattices, with significant advantages. First, the computational effort only grows linearly with system size making simulations of several hundred if not thousand lattice sites possible. Second, in many DMRG applications the accuracy of the solution can be as high as ten digits, making it one of the most precise algorithms to date. Sadly, DMRG behaves totally different in higher dimensions, because of the influence of quantum entanglement. Its different behavior in one and more dimensions is described by the so called area laws [5]. Already in two-dimensions only relatively small systems can be simulated at high precision, since the numerical effort grows exponentially with system size, making large lattices one more time inaccessible.

First DMRG was used to calculate static properties of low-lying eigenstates, especially ground states of strongly correlated Hamiltonians like in the Heisenberg, the tJ- or the Hubbard model, but soon extensions for the study of dynamically properties were developed. This became possible by an originally unrelated development, the so-called matrix product states (MPS), usually used for analytic studies as an special class of quantum states.

Östlund and Rommer [6] were the first who discovered the connection between MPS and DMRG, as they noticed, that the block-growth step in an infinite size DMRG (iDMRG) (see section 3.8.1) is expressible by MPS. Immediately afterwards, J. Dukelsky and al.

[7] showed that finite system DMRG (section 3.8.2) also leads to MPS. The strong relation between MPS and DMRG opened up the way to impressive extensions invisible in the complex DMRG language, namely the efficient use of periodic boundary conditions, infinite-system algorithms, numerical renormalization group (NRG) [8] applications, treatment of continuous systems and also new developments in the analysis of systems with higher dimensions [9].

But the probably most important extension was made by White, Feiguin [10] and Vidal [11, 12]. They developed an efficient time evolution scheme for one-dimensional systems based on DMRG, the time-evolving block decimation (TEBD) respectively the real-time or time-dependent DMRG (tDMRG). This is substantial progress since the time evolution of strongly correlated quantum states opens up their full dynamical behavior.

So far, having a theoretical tool to calculate one-dimensional quantum systems at an incredible accuracy and being able to simulate the dynamics in these systems is magnificent, but do one-dimensional systems really bear a meaning in nature?

Initially, one-dimensional quantum systems were indeed just analytic toy systems for theoretical physicists, but since the late 1970's more and more experimental realizations of such systems appeared. The first experimental systems were bulk materials with one-dimensional structures inside.With advances in nanotechnology, isolated one-dimensional systems appeared, e.g. quantum wires, Josephson junction arrays, edge states in quantum Hall systems or nanotubes.

Quite recently [13, 14] some progress has been made in the trapping of ultra-cold quantum gases in optical lattices. With this technology it is possible to build highly controllable and tunable Hamiltonians of strongly interacting quantum systems in several dimensions. This enables the experimental study and investigation of formerly only theoretical known quantum models. In combination with the ability to simulate such systems by means of DMRG and its deduced algorithms this will result in a fruitful physical playground and will become an important field of investigation in the near future.

At our institute of Theoretical and Computational Physics at TU Graz one of the main areas of research has been DMRG theory and its applications. For example, Peter Pippan engaged in the application of DMRG to periodic boundary conditions [15]. Martin J. Ganahl concentrated on the spin transport in one-dimensional Heisenberg spin 1/2 systems in real time [16] and Valentin Zauner analyzed the propagation of local signals on infinite systems in a so-called comoving window [17]. The present master thesis is based on the master thesis of Elias Rabel [18], who simulated different effects in one-dimensional systems, mainly the spin-charge separation and the Andreev-reflection in the spinless fermion and the repulsive Hubbard model.

The thesis is structured in following way.

In **chapter 2** the model systems are introduced. One of them is the Heisenberg model, which one can transform with a Jordan-Wigner transformation to the spinless fermion Hamiltonian. Also both, the attractive and repulsive Hubbard model, are investigated. On top of that the Bardeen-Cooper-Schrieffer (BCS) superconductor Hamiltonian is presented. Besides the plain introduction of the models, some of their symmetries and physical properties are described. In this chapter also some theoretical tools like the Bethe ansatz, Luttinger liquid theory and the Bosonization of Hamiltonians are represented. And of course, the main research targets of this master thesis, the physics of spin-charge separation and the Andreev-effect are illustrated.

Chapter 3 starts with a short introduction on MPS. Based on the singular value decomposition (SVD) the Schmidt decomposition (SD) as a compact representation of bipartite quantum states is explained. This gives us the possibility to measure the entanglement entropy in such systems and makes the derivation of MPS achievable. Then its just a small step to the measurement of observables in the MPS language. Finally the infinite- and the finite size DMRG algorithms and the TEBD algorithm are explained.
The results for simulations of spin-charge separation and Andreev reflection for several model systems are presented extensively in **chapter 4**.
Finally, **chapter 5** contains a summary and conclusions.

2 Model systems and their physics

In this section, the model systems that are later used and some of their physical characteristics are presented. All of these systems have in common that they are one-dimensional[1], obey open boundary conditions (obc), and have only nearest neighbor interaction between their particles.

Going from one system to another, the complexity of the models will increase, but more physical interesting effects will appear.

First we will have a look at one of the easiest one-dimensional model systems, the Heisenberg model, analytically solvable for periodic boundary conditions (pbc) by help of the famous Bethe ansatz.

Application of the Jordan-Wigner transformation, which gives us the possibility to map spin operators onto fermionic creation and annihilation operators, opens the way to the second model we are going to analyze, the spinless fermion model. The introduction of Luttinger liquid theory and the bosonization technique reveals the first appearance of the effect of metal and superconductor interaction boundaries which this master thesis is all about, namely the Andreev reflection, although in this context only for spinless fermions. Since nature does not know fermions without spin at all[2], it would not be very satisfying to stop our investigation at this point. Adding spin to the fermions results in the famous Hubbard model[3]. Only small adaptations have to be made to apply the bosonization technique to this more complicated Hamiltonian, but we will be rewarded with new physical effects, namely spin charge separation and the Mott transition. Of course, Andreev reflection will also appear for fermions with spin.

Since Andreev reflection is an effect between metals and superconductors and superconductivity is an effect caused by the condensation of so-called Cooper pairs allowing two fermionic electrons to form a bosonic-like particle, the last model we will have a look at is the BCS model, able to describe s- and p-wave superconductors.

In this chapter, if not mentioned otherwise, especially concerning the physical properties of one-dimensional quantum systems, I will closely follow the book of Giamarchi [19].

---

[1] For reasons later explained in this master thesis (see section 3.6.2).

[2] Of course, there are systems, which can be treated like "spinless fermions". Just imagine a system consisting of fermions, which are all of the same spin species.

[3] Interestingly, the one-dimensional Hubbard model with pbc is also solvable by means of the algebraic Bethe ansatz, but this is not part of the following investigations. For the interested reader I refer to [20].

2.1 Heisenberg model

The first model we are going to discuss is the simplest model possible, a one-dimensional Heisenberg spin-1/2 chain. It is used for describing critical points and phase transitions in magnetic systems (ferromagnetic, anti-ferromagnetic). The model consists of L sites with either a spin up electron or one with spin down sitting on each site (see figure 2.1):

$$\hat{H}_{\mathrm{HEI}} = J^{xy} \sum_{i=1}^{L-1} \left(\hat{S}_i^x \hat{S}_{i+1}^x + \hat{S}_i^y \hat{S}_{i+1}^y \right) + J^z \sum_{i=1}^{L-1} \hat{S}_i^z \hat{S}_{i+1}^z - B \sum_{i=1}^{L} \hat{S}_i^z \tag{2.1}$$

J^α is the coupling constant in α-direction, which describes the exchange of spins, and B_i is an external field in z-direction. $\hat{S}_i^\alpha$ are the standard spin operators which obey the well-known commutation relations

$$\left[\hat{S}^\alpha, \hat{S}^\beta \right] = i \epsilon_{\alpha\beta\gamma} \hat{S}^\gamma \quad . \tag{2.2}$$

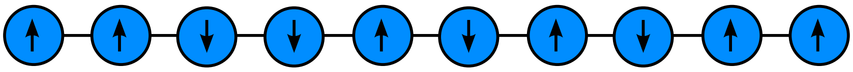

Figure 2.1: Heisenberg spin chain of length $L = 10$. Each site is occupied either by a spin up electron (blue circles with ↑) or a spin down electron (circles with ↓).

In this special Hamiltonian only nearest neighbor interaction is taken into account and it is rotational invariant in the xy-plane, but has a different coupling constant in the z-direction. This is the famous XXZ model[4].

Performing the simple transformation $\hat{S}^\pm = S^x \pm i S^y$ leads to

$$\hat{H}_{\mathrm{HEI}} = \frac{J^{xy}}{2} \sum_{i=1}^{L-1} \left(\hat{S}_i^+ \hat{S}_{i+1}^- + \hat{S}_{i+1}^+ \hat{S}_i^- \right) + J^z \sum_{i=1}^{L-1} \hat{S}_i^z \hat{S}_{i+1}^z - B \sum_{i=1}^{L} \hat{S}_i^z \tag{2.3}$$

If one chooses the parametrization $J^{xy} = J$, $J^z = J\Delta$, the system is isotropic in spin for $\Delta = 1$. We call this the spin isotropic point. Furthermore, the ground state of the system is always ferromagnetic for negative J^z and anti-ferromagnetic for a positive coupling constant. Needless to say this is only true if one does not consider any external field.

Performing a transformation by changing the sign of two components of the spin operators[5]

$$\hat{S}_i^x \to (-1)^i \hat{S}_i^x \tag{2.4}$$

$$\hat{S}_i^y \to (-1)^i \hat{S}_i^y \tag{2.5}$$

$$\hat{S}_i^z \to \hat{S}_i^z \tag{2.6}$$

leads to $J^{xy} \to -J^{xy}$, but $J^z \to J^z$. Thus it is enough to consider $J^{xy} > 0$ regardless of the sign of the couplings.

---

[4] The most general Heisenberg model is the XYZ-model with different coupling constants for every direction in space ($J^x \neq J^y \neq J^z$), but the XXZ-model is the most common one and therefore we introduced it straightaway.

[5] Note that changing the sign of all three components of the spin operator would violate the spin commutation relation in equation 2.2.

2.1.1 Bethe Ansatz

In 1932, Hans Bethe presented a method for obtaining the exact eigenvalues and eigenvectors of the one-dimensional spin-1/2 Heisenberg model with periodic boundary conditions, the famous Bethe ansatz. In this section I will follow the papers of Karbach and Müller on this topic [1, 2].

Let us take the Hamiltonian of equation 2.3 without an external magnetic field, a chain of length L with periodic boundary conditions ($L+1=1$) and set $J=-J^{xy}=-J^z$, i.e. the isotropic ferromagnet:

$$\hat{H}=-J\sum_i^L\left[\frac{1}{2}\left(\hat{S}_i^+\hat{S}_{i+1}^-+\hat{S}_i^-\hat{S}_{i+1}^+\right)+\hat{S}_i^z\hat{S}_{i+1}^z\right] \quad . \tag{2.7}$$

The basis vectors of the Heisenberg Hamiltonian in z-direction are a combination of up ($\uparrow$) and down ($\downarrow$) spins:

$$|\psi\rangle \;=\; |\sigma_1\dots\sigma_L\rangle \quad \text{with} \quad \sigma_j=\uparrow,\downarrow \quad . \tag{2.8}$$

Two symmetries of the one-dimensional Heisenberg model are essential for the Bethe ansatz. First the rotational symmetry around the z-axis and second the conservation of the z-component of the total spin S_T^z:

$$\left[\hat{H},S_T^z\right] \;=\; 0 \quad \text{with} \quad S_T^z=\sum_{j=1}^L\hat{S}_j^z \quad . \tag{2.9}$$

Therefore we can sort the basis vectors by their number of down spins r according to their quantum number $S_T^z=L/2-r$ and thus block diagonalize the Hamiltonian.

The easiest block is the one with $r=0$. Here all spins are aligned in the up direction and the block only consists of the vector $|F\rangle=|\uparrow\dots\uparrow\rangle$ with energy $E_0=-JL/4$. This will be the vacuum state for our consideration and excitations from this state will be spin flips at certain sites j.

For $r=1$ we get L basis vectors which we will label by the position of the flipped spin

$$|j\rangle \;=\; \hat{S}_j^-|F\rangle \quad j=1,\dots,L \quad . \tag{2.10}$$

Due to the translational invariance of the Hamiltonian $\hat{H}$ we get plane waves for our eigenvectors as a superposition of the basis vectors:

$$|\psi\rangle \;=\; \sum_{j=1}^L a(j)|j\rangle \;=\frac{1}{\sqrt{L}}\sum_{j=1}^L e^{ikj}|j\rangle \quad , \tag{2.11}$$

where k denotes the discrete wave numbers $k=2\pi m/L$ with $m=0,\dots,L-1$ because of the periodic boundary conditions. The eigenvectors $|\psi\rangle$ are spin wave excitations with wavelength $\lambda=2\pi/k$ called magnons with energy

$$E-E_0 \;=\; J\left(1-\cos k\right) \quad . \tag{2.12}$$

The case with $r = 2$ is a superposition of two magnon states. Therefore we take the ansatz

$$|\psi\rangle = \sum_{1\leq j_1<j_2\leq L} a(j_1,j_2)|j_1,j_2\rangle \tag{2.13}$$

$$a(j_1,j_2) = \alpha e^{i(k_1j_1+k_2j_2)} + \beta e^{i(k_1j_2+k_2j_1)} \tag{2.14}$$

$$|j_1,j_2\rangle = \hat{S}^-_{j_1}\hat{S}^-_{j_2}|F\rangle \quad , \tag{2.15}$$

where $|j_1,j_2\rangle$ are basisvectors in the subspace of dimension $N(N-1)/2$. As a result of the $\hat{S}^z_i\hat{S}^z_{i+1}$ coupling in the Heisenberg Hamiltonian, the spins feel a potential and thus can scatter. That is why we have to make a case distinction whether the two electrons of spin down are on neighboring sites or not. If they are not on neighboring sites ($j_1 + 1 < j_2$) we get the coefficients $a(j_1,j_2)$ by plugging in the wave function of equation 2.13 into the Heisenberg Hamiltonian in equation 2.3 :

$$\begin{aligned} a(j_1,j_2) = \frac{J}{2\,(E-E_0)}\Big(&4a(j_1,j_2) - a(j_1-1,j_2) - a(j_1+1,j_2) \\ &- a(j_1,j_2-1) - a(j_1,j_2+1)\Big) \quad . \end{aligned} \tag{2.16}$$

On neighbouring sites ($j_1 + 1 = j_2$) we get instead

$$a(j_1,j_2) = \frac{J}{2\,(E-E_0)}\left(2a(j_1,j_2) - a(j_1-1,j_2) - a(j_1,j_2+1)\right) \quad . \tag{2.17}$$

Comparing equations 2.16 and 2.17 one can see, that the terms $a(j_1+1,j_2)$ and $a(j_1,j_2-1)$ vanish, because the electrons can not hop onto the same site. However to obtain the same energy

$$E - E_0 = J\sum_{j=1,2}(1-\cos k_j) \tag{2.18}$$

for both cases, it requires a modification of the amplitude ratio which has to be added as a phase factor in the ansatz 2.14

$$\frac{\alpha}{\beta} \equiv e^{i\phi} = -\frac{e^{i(k_1+k_2)}+1-2e^{ik_1}}{e^{i(k_1+k_2)}+1-2e^{ik_2}} \tag{2.19}$$

$$a(j_1,j_2) = \alpha e^{i\left(k_1j_1+k_2j_2+\frac{1}{2}\phi_{12}\right)} + \beta e^{i\left(k_1j_2+k_2j_1+\frac{1}{2}\phi_{21}\right)} \quad . \tag{2.20}$$

For the phase factor, the following rule applies:

$$\phi_{12} = -\phi_{21} \equiv \phi \tag{2.21}$$

$$2\cot\frac{\phi}{2} = \cot\frac{k_1}{2} - \cot\frac{k_2}{2} \quad . \tag{2.22}$$

Because of the translational invariance of the wave function, implying that $a(j_1,j_2) = a(j_2,j_1+L)$, an additional relationship between k_1, k_2 and ϕ occurs for the coefficients in equation 2.20:

$$e^{ik_1N} = e^{i\phi}, \quad e^{ik_2N} = e^{-i\phi} \quad , \tag{2.23}$$

or rewritten by taking the logarithm

$$Nk_1 = 2\pi\lambda_1 + \phi, \quad Nk_2 = 2\pi\lambda_2 - \phi \quad . \tag{2.24}$$

The λ_i are integers called the Bethe quantum numbers.
Finally we get the solution of our problem by finding all the possible pairs (λ_1, λ_2) conforming to the equations 2.22 and 2.24.
We will now discuss only the results of this problem. For a detailed analysis I refer to [1] and [2].
The solution of the Bethe ansatz splits in two classes, the magnon bound states and the magnon scattered states and every class consists of two of these states for $r = 2$ overturned spins.
We get the first magnon state by setting one of the Bethe quantum numbers to zero, $\lambda_1 = 0, \lambda_2 = 0, 1, \dots, L-1$. These L states are called C_1.
The second magnon states C_2 occur for nonzero Bethe quantum numbers, which differ by two or more: $\lambda_1 > 0, \lambda_2 > 0$ and $\lambda_2 - \lambda_1 \geq 2$.
The remaining class C_3, the two magnon states, consists of nonzero Bethe quantum numbers, which are equal or differ by unity. Most of the Bethe quantum numbers of this class are complex. In figure 2.2 the energies of all possible wave vectors of the Bethe solution for two magnon states for a Heisenberg spin-1/2-chain of length $L = 32$ are depicted.

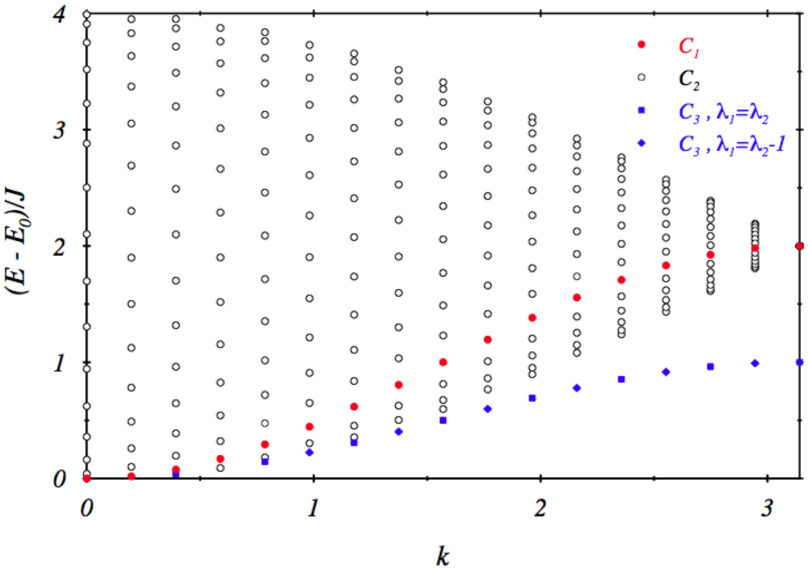

Figure 2.2: Excitation energy $(E - E_0)/J$ versus the wave number k of all $L(L-1)/2$ eigenstates in the invariant subspace with $r = 2$ overturned spins for a system with $L = 32$. States of class C_1 are denoted by red circles, states of class C_2 by open black circles, and states of class C_3 by blue squares if $\lambda_2 = \lambda_1$, or blue diamonds if $\lambda_2 = \lambda_1 + 1$ [1].

In general, r spins are flipped from the totally polarized vacuum state $|F\rangle$. We can write the eigenstates in a similar fashion as before for the case with $r = 1$ and $r = 2$ (without derivation):

$$
\begin{aligned}
|\psi\rangle &= \sum_{1\leq j_1<\ldots<j_r\leq L} a(j_1,\ldots,j_r)|j_1,\ldots,j_r\rangle && (2.25)\\
|j_1,\ldots,j_r\rangle &= \hat{S}^-_{j_1}\ldots\hat{S}^-_{j_r}|F\rangle \quad , && (2.26)
\end{aligned}
$$

For the coefficients we get the relation

$$
a(j_1,\ldots,j_r) = \sum_{\mathcal{P}} \exp\left(i\sum_{n=1}^{r} k_{\mathcal{P}_n} j_n + \frac{i}{2}\sum_{m<n}\phi_{\mathcal{P}_m\mathcal{P}_n}\right) \quad . \tag{2.27}
$$

where $\mathcal{P}$ denotes the $r!$ permutations of the labels $(1,\ldots,r)$ and ϕ_{mn} are the 2-body scattering phases satisfying the following equation

$$
2\cot\frac{\phi_{mn}}{2} = \cot\frac{k_m}{2} - \cot\frac{k_l}{2} \quad \text{, with} \quad m,n = 1,\ldots,r \quad . \tag{2.28}
$$

Translational invariance leads to the relation

$$
Lk_n = 2\pi\lambda_n + \sum_{m\neq n}\phi_{mn} \quad \text{, with} \quad n = 1,\ldots,r \quad , \tag{2.29}
$$

where λ_n are the Bethe quantum numbers going from 0 to $L-1$, which are related to the momentum of the eigenstates

$$
k = \frac{2\pi}{L}\sum_{n=1}^{r}\lambda_n \quad . \tag{2.30}
$$

The energy of the eigenstates is

$$
E = E_0 + J\sum_{n=1}^{r}(1 - cos(k_n)) \quad . \tag{2.31}
$$

2.1.2 Jordan-Wigner transformation

The one-dimensional Heisenberg model is closely related to another Hamiltonian. One can interpret the two dimensional Fock space with spin up ($|+1/2\rangle$) and down electrons ($|-1/2\rangle$) as a chain where a site is either occupied $|1\rangle$ or not $|0\rangle$. The $\hat{S}^+_i$ operator can be seen as the creation operator of a fermion on site i and $\hat{S}^-_i$ as its annihilation operator. Therefore the operators $\hat{S}^+_i$ and $\hat{S}^-_i$ should obey fermionic anti-commutation rules. While the operators fulfill the fermionic commutation relations on the same site, they do not on different sites. Pascual Jordan and Eugene Wigner discovered in 1928 [21] that adding a preceding phase factor to the ladder operators can solve this problem

$$
\begin{aligned}
\hat{c}_i &= e^{+i\Phi_i}\hat{S}^-_i && (2.32)\\
\hat{c}^\dagger_i &= e^{-i\Phi_i}\hat{S}^+_i && (2.33)\\
\Phi_i &= \pi\sum_{j<i}\hat{S}^+_j\hat{S}^-_j \quad . && (2.34)
\end{aligned}
$$

For every spin up electron preceding the electron on site i a phase factor of -1 is picked up. One can reformulate the phase factor above in a more simple form and one gets the Jordan-Wigner transformation:

$$\begin{aligned} \hat{c}_i &= \prod_{j<i}\left(1-2\hat{S}_j^+\hat{S}_j^-\right)\hat{S}_i^- = \prod_{j<i}\left(-2\hat{S}_j^z\right)\hat{S}_i^- && (2.35)\\ \hat{c}_i^\dagger &= \prod_{j<i}\left(1-2\hat{S}_j^+\hat{S}_j^-\right)\hat{S}_i^+ = \prod_{j<i}\left(-2\hat{S}_j^z\right)\hat{S}_i^+ \quad . && (2.36)\end{aligned}$$

So the transformed operators obey the fermionic anticommutation rules

$$\left\{\hat{c}_i, \hat{c}_j^\dagger\right\} = \delta_{ij} \quad . \tag{2.37}$$

Performing a Jordan-Wigner transformation on the Hamiltonian in equation 2.3 and considering $\hat{S}^z = \hat{S}^+\hat{S}^- - 1/2$ gives us

$$\hat{H} = \frac{J^{xy}}{2}\sum_i\left(\hat{c}_i^\dagger\hat{c}_{i+1} + \hat{c}_{i+1}^\dagger\hat{c}_i\right) + J^z\sum_i\hat{n}_i\hat{n}_{i+1} - J^z\sum_i\hat{n}_i - B\sum_i\hat{n}_i + \frac{L}{4} + \frac{LB}{2} \quad . \tag{2.38}$$

The first term can be interpreted as kinetic energy with the hopping integral $t = \frac{J^{xy}}{2}$, the second term is the electron-electron interaction controlled by $V_i = J_i^z$, the third term can be summarized in a chemical potential $\mu = -\epsilon = J^z + B$ and the last two terms are just an energy offset and can be neglected for that reason. This gives us the Hamiltonian for spinless fermions.

2.2 Spinless fermions

In the spinless fermion model, fermions can hop between neighboring sites with a hopping matrix element t. They experience a nearest neighbor interaction V. A local interaction is precluded of course by the Pauli principle. A magnetic field along the z axis for the spin chain is simply a chemical potential $-B\sum_i\hat{S}_i^z = -\epsilon\sum_i\left(\hat{n}_i - \frac{1}{2}\right)$ for spinless fermions

$$\hat{H}_{\text{SF}} = -t\sum_{i=1}^{L-1}\left(\hat{c}_i^\dagger\hat{c}_{i+1} + \hat{c}_{i+1}^\dagger\hat{c}_i\right) + V\sum_{i=1}^{L-1}\hat{n}_i\hat{n}_{i+1} + \epsilon\sum_{i=1}^{L}\hat{n}_i \quad . \tag{2.39}$$

The operator $\hat{c}_i^\dagger$ creates a particle in a Wannier state on site i, whereas the operator $\hat{c}_i$ destroys one. $\hat{n}_i = \hat{c}_i^\dagger\hat{c}_i$ is the number of particles on each site.

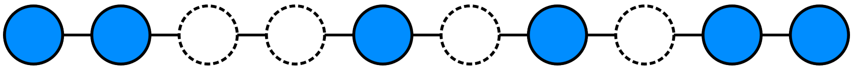

Figure 2.3: This figure represents a one-dimensional spinless fermion model with $L = 10$ sites. A site can either be occupied by a spinless electron (blue solid circle) or not (white dashed circle). Note that this model is exactly the Jordan-Wigner transform of the Heisenberg spin-1/2-chain state in figure 2.1, where a spin up electron corresponds to a fermion on site i, and a down electron corresponds to an empty site.

The configuration space is of dimension two with a site either being occupied by a fermion ($|1\rangle$) or unoccupied ($|0\rangle$) (see figure 2.3).
In the absence of an electromagnetic field in the Heisenberg Hamiltonian, the average magnetization is zero ($\langle \hat{S}^z \rangle = 0$), which means a half filled band $\langle \hat{n} \rangle = 1/2$ in the spinless fermions picture. A completely filled band for spinless fermions means a Heisenberg chain with all spin up, whereas an empty band corresponds to all spin down.
At $t = 0$, the model is equivalent to the Ising model and describes in the ground state a "frozen" electron distribution (Wigner crystal) depending on the specific form of V_i. At $V_i = 0$ (any t) we have the case of non-interacting electrons, which is the free fermion Hamiltonian. The ground state is then a filled Fermi sea, where all electrons occupy the lowest energy states till the Fermi energy and excitations from this ground state have definitely fermionic character.
If we perform the transformation

$$\hat{c}_i \;\rightarrow\; (-1)^i \tilde{c}_i^\dagger \tag{2.40}$$

we see that the terms of the Hamiltonian in equation 2.57 with t and V remain unchanged, whereas the chemical potential changes its sign $\epsilon_i = -\epsilon_i$ in the new variables $\tilde{c}_i$.
This is the particle-hole symmetry, which corresponds to the spin reversal symmetry in equation 2.3.

2.2.1 Luttinger Liquids and Bosonization

A Luttinger liquid describes interacting fermions (electrons) in a one-dimensional system. It is very different from Fermi liquid theory, which breaks down in one dimension. The elementary excitations of a Luttinger liquid are collective excitations of the whole one-dimensional chain instead of quasi-particle excitations in Fermi liquids, leading to an interesting effect only observable in one-dimensional systems, the spin charge separation. This means that spin and charge of an electron behave like independent particles, the spinon for spin and the holon for charge, and they can travel through the chain with different velocities.This effect is in some kind preposterous to common sense. Just imagine a system with low electron density. One can imagine that the charge velocity couples to the electrons traveling through the chain. But what is then the medium carrying the spin, if the charge has a different velocity? Should not the spin also be bound to the electrons? Then why are there different velocities?
To understand this effect in special and one-dimensional systems in general it is necessary to introduce a standard technique in one dimension, named bosonization.
Starting point for the bosonization technique is the density operator for a one-dimensional system

$$n(x) \;=\; \sum_{k=1}^{N} \delta(x - x_k) \qquad , \tag{2.41}$$

where x_k denotes the position of the k-th particle. We can label these particles by a monotonically increasing field $\Phi(x)$ that consists of a product of multiples of 2π and the particle positions x_k:

$$\Phi(x_k) \;=\; 2\pi x_k \qquad , \tag{2.42}$$

which is always possible in one dimension by labeling the particles from the left to the right starting at $x = -\infty$ (figure 2.4).

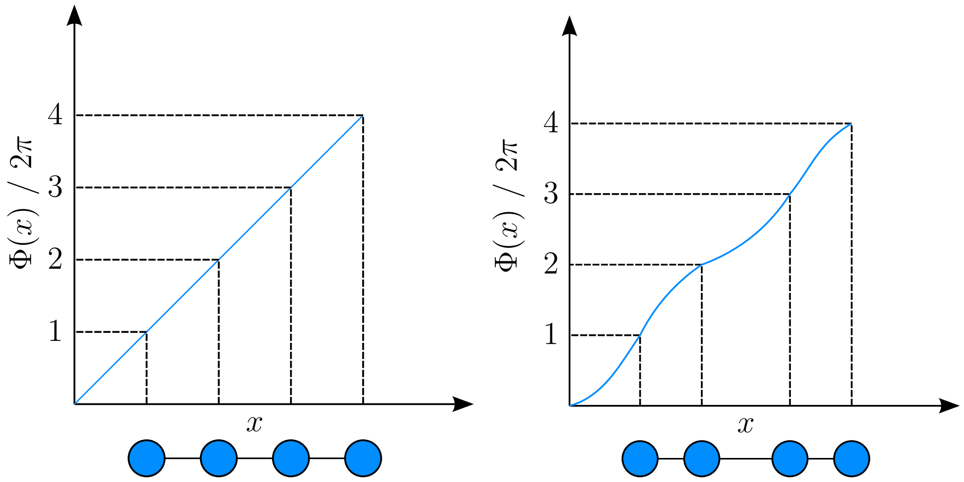

Figure 2.4: Two examples of the labeling field $\Phi(x)$. If the particles form a perfect lattice of lattice spacing 1, then $\Phi(x)$ is just a straight line (left). If the particles have different spacings between each other, we get a non linear behavior of the labeling function $\Phi(x)$ (right).

Using the identities for the transformation of delta functions and the before defined labeling field

$$\delta(f(x)) = \sum_{x_k\text{:zeros of f}} \frac{1}{|f'(x_k)|}\delta(x - x_k) \tag{2.43}$$

and the Poisson summation formula with the integer p

$$\sum_p e^{ipx} = 2\pi \sum_k \delta(x - 2\pi k) \quad , \tag{2.44}$$

we can rewrite the density operator

$$n(x) = \frac{\nabla\Phi(x)}{2\pi} \sum_p e^{ip\Phi(x)} \quad . \tag{2.45}$$

Then we define the particle positions in a more convenient way with respect to their crystalline rest positions $x_k^0 = n_0 k$ with the mean density $n_0 = \frac{N}{L}$. After introducing a field $2\Phi(x) = 2\pi n_0 x - \Phi(x)$ we transformed our starting point for bosonization to obtain the following form

$$n(x) = \left(n_0 - \frac{\nabla\Phi}{\pi}\right) \sum_p e^{2ip(\pi n_0 x - \Phi(x))} \quad . \tag{2.46}$$

Let us introduce field operators for the creation $\psi^\dagger(x)$, respectively for the annihilation $\psi(x)$ of a particle at site x. Note that these operators could be of bosonic or fermionic nature. Then we get for the density operator at site x in the language of this new operators

$$n(x) = \psi^\dagger(x)\psi(x) \quad . \tag{2.47}$$

A creation operator can always be transformed with an amplitude phase ansatz in terms of

$$\psi^\dagger(x) \;=\; \sqrt{n(x)}e^{-i\theta(x)} \quad , \tag{2.48}$$

where $\theta(x)$ is another field. Of course the field operators have to obey (anti-) commutation rules, e.g. bosonic ones:

$$\left[\psi(x), \psi^\dagger(x')\right] \;=\; \delta\left(x - x'\right) \quad . \tag{2.49}$$

This leads after some mathematics to the commutator rule:

$$\left[\nabla\Phi(x)/\pi, \theta(x')\right] \;=\; -i\delta\left(x - x'\right) \quad , \tag{2.50}$$

or after partial integration

$$\left[\Phi(x), \nabla\theta(x')/\pi\right] \;=\; i\delta\left(x - x'\right) \quad . \tag{2.51}$$

This can be interpreted as the commutator relation between a field and its canonical momentum. Therefore we define $\Pi(x) = \nabla\theta(x)/\pi$ as the canonical momentum of the labeling field $\Phi(x)$.

So we can rewrite the bosonic field creation operator for example

$$\psi_B^\dagger(x) \;=\; \sqrt{n_0 - \nabla\Phi(x)/\pi}\, \sum_p e^{2ip(\pi n_0 x - \Phi(x))} e^{-i\theta(x)} \quad . \tag{2.52}$$

For the fermionic field creation operator we have to add a factor of $+\frac{1}{2}$ to the integers p to obey fermionic anti-commutation rules

$$\psi_F^\dagger(x) \;=\; \sqrt{n_0 - \nabla\Phi(x)/\pi}\, \sum_p e^{(2p+1)i(\pi n_0 x - \Phi(x))} e^{-i\theta(x)} \quad . \tag{2.53}$$

With equations 2.46, 2.52 and 2.53 we have a dictionary to translate Hamiltonians like the Hamiltonian for spinless fermions in equation 2.57 in field operators, which obey bosonic commutation relations independently of their original statistics. That is why it is named bosonization.

An advantage of this method is that Hamiltonians which are translated with this method, are usually quadratic in the new fields instead of being typically quartic in the old ones, because of the interaction terms. That is what makes bosonization extremely attractive. Let us consider the low-energy limit, in which there is only a small variation in the fields. Thus only small p terms matter and in the limiting case we can ignore all higher terms, which leaves us only with the non-oscillating $p = 0$ term.

The potential energy of the Hamiltonian consisting of density-density interaction translates with our bosonization dictionary to the derivative squared of our labeling field

$$\int dx\; n(x)^2 \;\rightarrow\; \int dx\, \left(\nabla\Phi(x)\right)^2 \quad . \tag{2.54}$$

Similarly the kinetic energy term translates for the low-energy limit as

$$\int dx \nabla\psi^\dagger \nabla\psi \;\rightarrow\; \int dx\; n_0\left(\theta(x)\right)^2 \quad . \tag{2.55}$$

All in all we get for the most general low energy Hamiltonian for spinless fermions

$$H = \frac{u}{2\pi}\int dx \left[K\left(\pi\Pi(x)\right)^2 + \frac{1}{K}\left(\nabla\Phi(x)\right)^2\right] \quad , \tag{2.56}$$

where Φ is related to the long-wavelength component of the electron density through $\rho = -\nabla\Phi/\pi$, and Π is the canonical momentum conjugate to Φ, $[\Phi(x), \Pi(y)] = i\pi\delta(x-y)$. In this equation two new coefficients uK and u/K appear, where u is the velocity and K is the Luttinger liquid parameter, which characterizes the low-energy physics for all fermionic and bosonic one-dimensional systems. For $0 < K < 1$ the Luttinger liquid parameter describes repulsive interactions, for $K = 1$ we get the non-interacting case and for $K > 1$ attractive interaction occurs.

2.2.2 Andreev Reflection for spinless fermions

The Andreev reflection is named after Alexander F. Andreev, who first predicted it in 1964 [22]. It is an interface effect between a normal metal and a superconductor, describing the elementary mechanism for converting single electron states to Cooper pairs [23].
An incident electron coming from the metal hits the metal-superconductor interaction boundary. The electron can be transferred into the superconductor by forming a Cooper pair, consisting of two electrons, with another electron from the metal of opposite spin species than itself. Because of charge, conservation a hole then has to be reflected back into the metal (see figure 2.5).
The spin degree of freedom can be ignored, because an incident electron with spin up (down) forms a Cooper pair together with another electron with spin down (up) upon reflection of a hole with spin up (down).
This effect is reversible, so that an incident hole from the metal transfers a single Cooper pair out of the superconducting condensate upon the reflection of an electron.

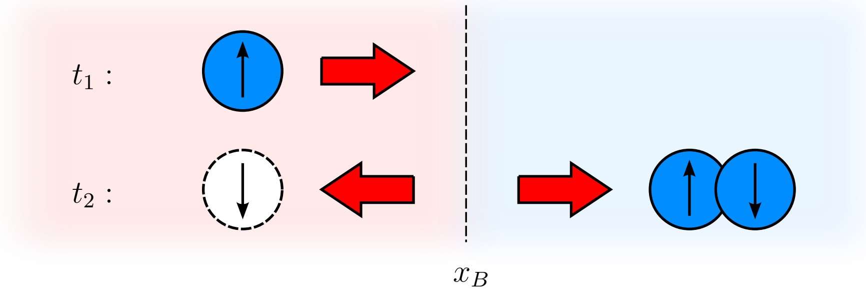

Figure 2.5: Schematic representation of the Andreev reflection. An incoming electron with spin up (↑) at time t_1 hitting the interface at x_B between a normal conductor (left, light red area) and a superconductor (right, light blue area) produces a Cooper pair with total spin 0 (↑ + ↓= 0) within the superconductor and a retroreflected hole (white) with spin up (↑) in the normal conductor at time t_2.

Andreev-like[6] reflections have been predicted in an inhomogeneous Luttinger liquid [24,

---

[6] In one-dimensional spinless fermion systems there exist no Cooper pairs, that is why the effect is named Andreev-like.

25]. We get such an inhomogeneous liquid by making the interactions site dependent. Let us introduce an interaction boundary x_B. On the left side of this boundary we have a different interaction V than on its right side:

$$\hat{H}_{\mathrm{SF}} = -t\sum_{i=1}^{L-1}\left(\hat{c}_i^{\dagger}\hat{c}_{i+1}+\hat{c}_{i+1}^{\dagger}\hat{c}_i\right)+\sum_{i=1}^{L-1}V_i\hat{n}_i\hat{n}_{i+1}+\sum_{i=1}^{L}\epsilon_i\hat{n}_i \quad , \tag{2.57}$$

$$\begin{aligned}\text{with}\quad V_i &= V_L \quad \text{for } i < x_B\\ V_i &= V_R \quad \text{for } i \geq x_B\end{aligned}$$

and $V_L \neq V_R$. Introducing a site dependence of the interaction parameter V also leads to a site dependence of the Luttinger liquid parameters $K \to K(x)$. For that reason we have two different interaction parameters K_L and K_R. When a propagating density excitation is incident from the left on the boundary x_B, the strength of the reflection is quantified by a reflection coefficient γ which has been calculated in a low excitation and long wavelength hydrodynamic limit [24] with smooth interaction border to be

$$\gamma = \frac{K_L - K_R}{K_L + K_R} \quad . \tag{2.58}$$

For $\gamma < 0$, excitations are transmitted with a larger amplitude $1-\gamma$, which is compensated by the reflection of a hole-like charge excitation with amplitude $|\gamma|$. This is analogous to Andreev reflection when an electron is incident on a normal metal-superconductor boundary.

So Andreev reflection has been predicted to occur for the transition from a more repulsive to a less repulsive region or for the transition from an attractive region to an even more attractive one.

2.3 Hubbard model

Adding another degree of freedom to the spinless fermion model, namely the spin[7], one gets the probably most famous model of strongly interacting fermions, the Hubbard model. It is used for describing transitions between conducting and insulating systems. This model is the simplest generalization to fermions with spin of the spinless model in equation 2.57:

$$\hat{H}_{\mathrm{HUB}} = -t\sum_{\substack{i=1\\ \sigma=\uparrow,\downarrow}}^{L-1}\left(\hat{c}_{i,\sigma}^{\dagger}\hat{c}_{i+1,\sigma}+\hat{c}_{i+1,\sigma}^{\dagger}\hat{c}_{i,\sigma}\right)+\sum_{i=1}^{L}U_i\hat{n}_{i,\uparrow}\hat{n}_{i,\downarrow}+\epsilon\sum_{\substack{i=1\\ \sigma=\uparrow,\downarrow}}\hat{n}_{i,\sigma} \quad . \tag{2.59}$$

Here, i labels the lattice sites which run from 1 to L and $\sigma =\uparrow,\downarrow$ labels the spin states. As usual $\hat{c}_{i,\sigma}^{\dagger}$ and $\hat{c}_{i,\sigma}$ are the creation and annihilation operators for an electron on site i with spin $\sigma =\uparrow,\downarrow$ and $\hat{n}_{i,\sigma}$ is the density or number operator on site i for spin σ. The configuration space is now 4-dimensional with the elements $\{|0\rangle, |\uparrow\rangle, |\downarrow\rangle, |\uparrow\downarrow\rangle\}$ (see figure 2.6). As one can see, double occupations of one site with fermions with opposite spin are now possible.

---

[7] What a surprise!

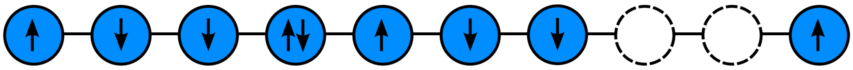

Figure 2.6: One-dimensional Hubbard model with $L = 10$ sites. There are four possibilities for the occupation of a site: a site can be occupied by one electron with either spin up (blue circles with ↑) or spin down (blue circles with ↓), a site can be empty (white dashed circles) or a double occupation with two electrons having opposite spin (blue circles with ↑↓) can occur. Due to the Pauli principle there are no states with more than two electrons, because then at least two particles would share the same set of quantum numbers.

In this model, electrons hop from site to site with a matrix element t. This is the standard tight binding kinetic energy. Electrons interact only if they are on the same site. Since the Pauli principle prevents two electrons of the same spin to be on the same site, it is enough to consider only the local coupling between electrons of opposite spin (Other terms would vanish because of the Pauli principle or simply become chemical potential terms). For this reason we can identify the second term as the on-site repulsion ($U > 0$) or on-site attraction ($U < 0$) term depending on its sign. For $U = 0$ we get again the free fermion Hamiltonian.

$\epsilon = -\mu$ is again a chemical potential as in equation 2.57. If one also wants to apply a magnetic field in z-direction, one has to add an additional term

$$H_h = -h \sum_{i=1}^{L} (\hat{n}_{i,\uparrow} - \hat{n}_{i,\downarrow}) \tag{2.60}$$

Let us have a look at the symmetries of the Hubbard model [26]. In the absence of a magnetic field h the system is spin rotational invariant (SU(2)-symmetry). For a generic filling the only charge symmetry is the U(1) symmetry, which is the multiplication of the operators by an arbitrary phase.

Obviously the Hubbard Hamiltonian is invariant under spatial reflections ($\vec{x} \to -\vec{x}$).

The Hubbard Hamiltonian also obeys particle-hole symmetry just as the spinless fermion Hamiltonian. Performing

$$c_{i,\sigma} \to (-1)^i c_{i,\sigma}^\dagger \tag{2.61}$$

leaves the kinetic energy t and the on-site repulsion U invariant and only changes the chemical potential $\epsilon \to -\epsilon$ and the external magnetic field $h \to -h$.

Another interesting symmetry is the particle-hole symmetry of just one spin species, called the asymmetric particle-hole symmetry, e.g.:

$$c_{i,\downarrow} \to (-1)^i c_{i,\downarrow}^\dagger \tag{2.62}$$

leaving the kinetic energy ($t \to t$) invariant, but changing the sign of the on-site repulsion ($U \to -U$) and transposes the chemical potential with the magnetic field and vice versa ($\epsilon \to -h$ and $h \to -\epsilon$). This transformation maps the spin sector on the charge sector and the charge sector on the spin while changing the repulsive system to an attractive one and

vice versa. At half-filling and in the absence of a magnetic field the transformation has only an effect on the on-site repulsion (attraction) U. With the spin sector becoming the charge sector and the other way around one has an additional charge symmetry (SU(2)) at half filling.
A sign change of the hopping matrix element t can be achieved by the following transformation:

$$\begin{aligned} \hat{c}^\dagger_{i,\sigma} &\to (-1)^i \ \hat{c}^\dagger_{i,\sigma} \quad \text{or} \\ \hat{c}_{i,\sigma} &\to (-1)^i \ \hat{c}_{i,\sigma} \quad . \end{aligned}$$

For repulsive interactions ($U > 0$), one expects the system to be dominated by antiferromagnetic exchange, because of the superexchange between spins. At half-filling (one particle per site) and for large U the system is equivalent to a Heisenberg chain with an exchange constant $J \approx \frac{4t^2}{U}$.
For attractive interactions ($U < 0$), on the other hand, one expects pairs of opposite spin to form a singlet on a site. These bound states behave like hard core bosons since they are made of two fermions. One could expect that these bosons condense and the system becomes superconducting.
In the non-interacting limit $U = 0$, we only have free independent particles like in a Fermi gas.
In the atomic limit $t = 0$ no hopping appears. For a repulsive model with an electron density below $L/2$, we only have empty states and single occupied sites at $T = 0$.
For $n \leq L/2$ and $U \to \infty$ again no double occupation occurs.
Large U results in the tJ-model

$$\hat{H}_{\mathrm{tJ}} = -t \sum_{i,\sigma} \left(\hat{c}^\dagger_{i,\sigma} \hat{c}_{i+1,\sigma} + \hat{c}^\dagger_{i+1,\sigma} \hat{c}_{i,\sigma} \right) - J \sum_i \left(\vec{S}_i \vec{S}_{i+1} - \frac{1}{4} \hat{n}_i \hat{n}_{i+1} \right)$$

with $J = 4t^2/U$.
At half filling ($n = L/2$) this is the Heisenberg model.

2.3.1 Bosonization of the Hubbard model

The bosonization technique in 2.2.1 can also be used for electrons with spin as well. All we have to do is to carry out the procedure with each spin species $\uparrow, \downarrow$ separately with different bosonic fields $\Phi_{\uparrow,\downarrow}$. If we introduce new bosonic fields for the charge part Φ_ρ respectively for the spin Φ_σ

$$\Phi_\rho = \frac{1}{\sqrt{2}} \left(\Phi_\uparrow + \Phi_\downarrow \right) \tag{2.63}$$

$$\Phi_\sigma = \frac{1}{\sqrt{2}} \left(\Phi_\uparrow - \Phi_\downarrow \right) \quad , \tag{2.64}$$

the charge and spin degrees of freedom decouple and we get two similar Hamiltonians for charge and spin of the exactly same form of 2.56

$$H = \frac{u_\nu}{2\pi} \int dx \left[K_\nu \left(\pi \Pi_\nu(x) \right)^2 + \frac{1}{K_\nu} \left(\nabla \Phi_\nu(x) \right)^2 \right] \quad , \tag{2.65}$$

where $\nu = \rho$ stands for the charge and $\nu = \sigma$ is for the spin with four different parameters u_ρ, u_σ, K_ρ and K_σ. The parameters u_ν are called the velocities whereas K_ν are called the Luttinger liquid parameters.

For half filling an additional term occurs in the Hamiltonian 2.65

$$H_u = \frac{2U}{(2\pi\alpha)^2} \int dx \cos\left(\sqrt{8}\Phi_\rho(x)\right) \quad . \tag{2.66}$$

This term is called the umklapp[8] term. For generic filling this term turns out to be irrelevant in a renormalization group study and can be neglected.

The velocities u_ν and the Luttinger liquid parameters K_ν are all functions of the local coupling parameter U with

$$\begin{aligned} \frac{u_\rho}{K_\rho} &= v_F\left(1 + \frac{U}{\pi v_F}\right) \\ \frac{u_\sigma}{K_\sigma} &= v_F\left(1 - \frac{U}{\pi v_F}\right) \quad . \end{aligned} \tag{2.67}$$

Introducing a site dependence of the coupling parameter U also leads to a site dependence of the Luttinger liquid parameters $K \to K(x)$. Implementing two regions of U, where U changes its value on an interaction boundary x_B, results in two different interaction parameters K_L and K_R, like we have seen in the spinless fermion case.

One can calculate the Luttinger parameters of the Hubbard model based on the Bethe ansatz, but this is quite a challenging task and would be going beyond the purposes of this master thesis. Nevertheless graphs which show the dependence of the Luttinger parameters on the parameters of the Hubbard model can be found in figures 2.7 to 2.10 taken from the work of Thierry Giamarchi and H. J. Schulz ([27, 28, 29]).

In the following figures the band-filling n is given as

$$n = \frac{n_\uparrow + n_\downarrow}{L} \quad ,$$

where $n_\uparrow$ is the number of particles with spin up, respectively $n_\downarrow$ is the number of particles with spin down and L is number of sites of the system. Naturally n goes from 0 to 2, where $n = 0$ corresponds to an empty Hubbard band, $n = 2$ stands for a completely filled band and $n = 1$ correlates to the Hubbard model at half-filling with interesting physical properties as seen later.

Looking at figure 2.7 one finds in agreement with the book of Giamarchi [19], where he theoretically deduces the limits of the Luttinger parameters, that K_ρ is always between $K_\rho = 1$ for $U \to 0$ and $K_\rho = \frac{1}{2}$ for $U \to \infty$ and K_σ is always equal to one.

In figure 2.8 the charge u_ρ and spin velocities u_σ for different U are shown as a function of the band-filling n. The charge and spin velocity is the same for the non-interacting ($U = 0$) Fermi gas. Then both velocities are equal to the Fermi velocity v_F:

$$U \to 0: \quad u_\rho = u_\sigma = v_F \quad \text{with} \quad v_F = 2t \sin\left(\frac{\pi n}{2}\right) \quad . \tag{2.68}$$

---

[8] This term is not named after the famous physicist Dr. Laurentius Umklapp, therefore it does not start with a capital letter.

For strong repulsive interactions the following relationship holds:

$$\begin{aligned} U \to \infty : \qquad\qquad & u_\rho = 2t \sin(\pi n) \\ & u_\sigma = \left(\frac{2\pi t^2}{U}\right)\left(1 - \frac{\sin(2\pi n)}{2\pi n}\right) \quad . \end{aligned} \tag{2.69}$$

The equations 2.68 and 2.69 for both limiting cases for the non-interacting and the strong repulsive interaction become apparent in figure 2.8 as the charge and the spin velocity is zero for $n = 0$. The charge velocity is also zero for half filling at $n = 1$, because the Hubbard model becomes insulating at this point for all values of U due to the Mott transition. The spin velocity on the other hand becomes a constant depending on U given by the super-exchange of the spins

$$u_\sigma \to J \quad \text{with} \quad J = \frac{4t^2}{U} \quad . \tag{2.70}$$

For $U \to \infty$ the spin velocity also vanishes ($u_\sigma(U \to 0) \to 0$) at half filling.

Another interesting quantity is the Wilson ratio R_W, which is defined as the ratio of the magnetic susceptibility to specific heat divided by temperature. This quantity has a simple relationship to the spin and the charge velocity (see [28])

$$R_W = \frac{\chi}{c_v/T} = \frac{2u_\rho}{u_\rho + u_\sigma} \tag{2.71}$$

and is represented in figure 2.10. The value of the ratio indicates interaction effects and quantifies spin fluctuations. For $U = 0$ the Wilson ratio is $R_W = 1$ and for $U \to \infty$ it approaches $R_W \to 2$.

Lets have a look on Andreev reflection in the Hubbard model. For a spin rotation invariant system such like the Hubbard model K_σ is always equal to one. So Andreev reflection can only occur for the charge part of the system, when the reflection coefficient γ calculated similar to equation 2.58 is negative [24]

$$\gamma = \frac{K_{\rho,L} - K_{\rho,R}}{K_{\rho,L} + K_{\rho,R}} \quad . \tag{2.72}$$

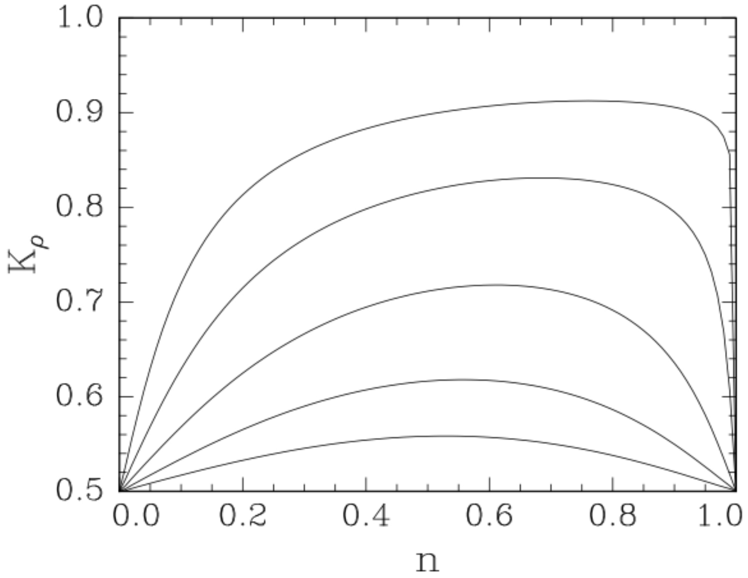

Figure 2.7: The correlation exponent K_ρ for the repulsive Hubbard model as a function of the bandfilling n for different values of U ($U/t = 1, 2, 4, 8, 16$ for the top to the bottom curves). Note the rapid variation near $n = 1$ for small U. [27]

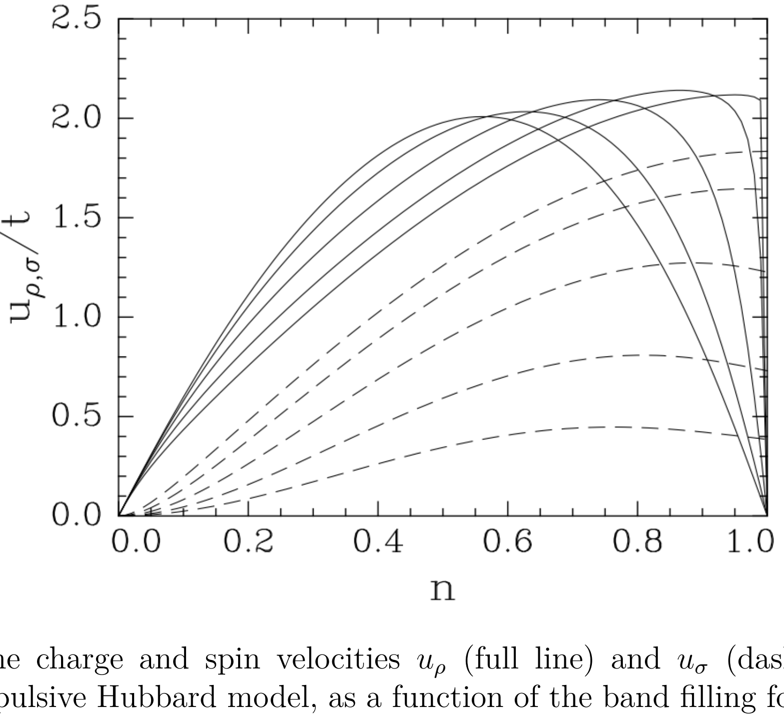

Figure 2.8: The charge and spin velocities u_ρ (full line) and u_σ (dashed line) for the repulsive Hubbard model, as a function of the band filling for different values of U/t: for u_σ $U/t = 1, 2, 4, 8, 16$ from top to bottom, for u_ρ $U/t = 16, 8, 4, 2, 1$ from top to bottom in the left part of the figure. [28]

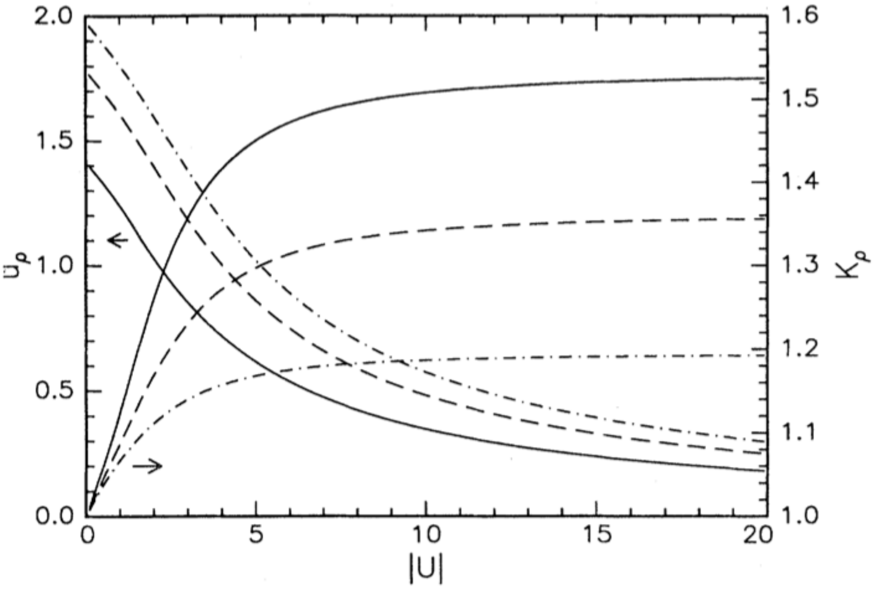

Figure 2.9: Luttinger parameters u_ρ and K_ρ for the attractive Hubbard model as a function of the interaction |U|. These values were obtained by a numerical integration of the Bethe ansatz equations on a system of $L = 200$ sites. Curves are for densities $n = 0.9$ (dash-dotted line), $n = 0.7$ (dashed line), $n = 0.5$ (full line). This figure is taken from [29].

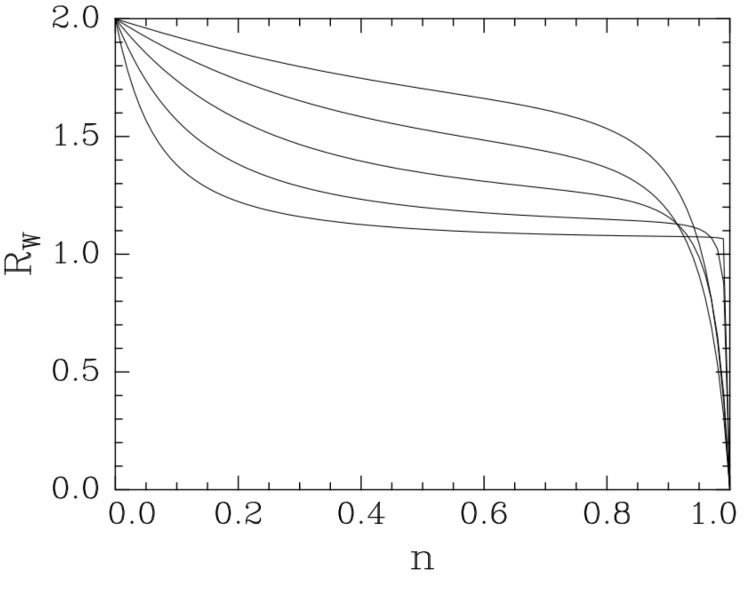

Figure 2.10: The Wilson ratio R_W for the one-dimensional Hubbard model, as a function of the band-filling for different values of U/t ($U/t = 16, 8, 4, 2, 1$ from top to bottom on the left side). Taken from [28].

2.3.2 Spin Charge Separation

If we take a closer look at the equations for the Luttinger parameters of the Hubbard model in 2.67, an interesting effect of one-dimensional systems almost hits our eye. By applying a particular interaction parameter U, we can see that the velocity of charge u_ρ differs from the velocity of spin u_σ. Therefore a charge excitation should propagate independently from a spin excitation.

Assuming that in higher dimension charge and spin are normally coupled to certain electrons propagating through the metal, this does obviously not apply to one-dimensional systems.

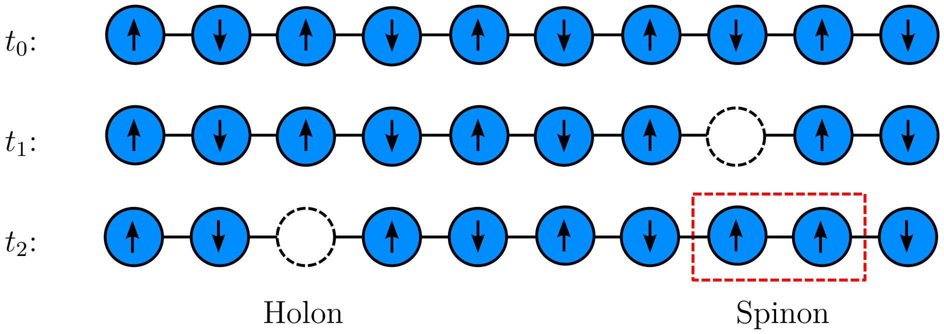

Figure 2.11: The one-dimensional system is in the Neel state at t_0. A single-particle excitation is created by removing a particle at time t_1. It is converted into two independent excitations, one containing only charge degrees of freedom (holon) and the other containing only spin degrees of freedom (spinon). These two excitations propagate with different velocities in the one-dimensional system, so that they are on different sites at time $t_2 > t_1$.

As we saw in equation 2.65 the Hamiltonian separates into two parts, a charge part and a spin part. As a result, single-particle fermionic excitations do not exist. The excitations are described by the fields ϕ_ρ and ϕ_σ. Let us represent the ground state by a state in which ϕ_ρ and ϕ_σ are constant at time t_0 (see figure 2.11). If we now remove a fermion at $t_1 > t_0$, it means that at a single site we create a kink both in ϕ_ρ and ϕ_σ. These excitations are free to propagate completely independently. After some time $t_2 > t_1$ one reaches a state, where at some site a charge is lacking but the spin environment around this hole is in its anti-ferromagnetic ground-state as before. This corresponds to an excitation that is a kink in ϕ_ρ but no disturbance in ϕ_σ. This excitation is called holon.

At another part of the system there is a place where no charge is missing but there are two neighboring sites with the same spin. This is a spin excitation with a spin 1/2 compared to the ground state. This excitation is known as spinon and corresponds to a kink in ϕ_σ. As we can see, these two excitations are free to move independently from each other in one dimension leading to the separation of spin and charge.

In higher dimensions the spinon and the holon would not separate because of the presence of neighboring chains which would lead to a string of frustrated bonds. This would cost the anti-ferromagnetic exchange energy that would grow linearly with distance.

Safi and Schulz showed in [30] that the spin charge separation also maintains if one connects a dirty wire, meaning a region with $U \neq 0$, with non-interacting leads with

$U = 0$ as shown schematically in figure 2.12. There a charge and spin excitation arrives from the left in a region consisting of a non-interacting lead connected at an interaction boundary to a dirty wire. Although the charge velocity equals the spin velocity at first, the charge and spin excitations become separated in the dirty wire through their different velocities. Curiously the separation is conserved when the two peaks enter the region with non-interacting lead on the very right.

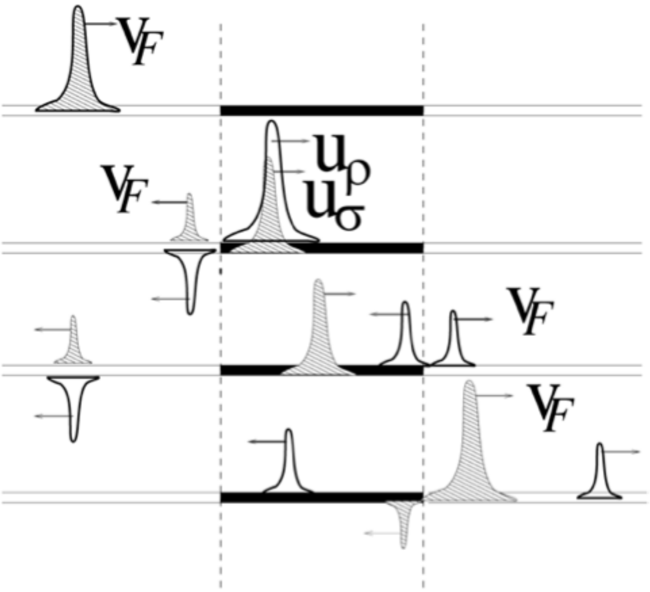

Figure 2.12: Dynamic transmission of an incident electron with spin up. The charge and spin (hatched) are separated even in the non-interacting leads at the very right. As an example, we consider here $u_\rho > u_\sigma$, $K_\sigma < 1$, $K_\rho > 1$ (taken from [30]). Note that for spin-invariant repulsive interactions ($K_\sigma = 1!$), the spin part is not reflected, while the charge undergoes reflections.

2.3.3 Mott transition in the one-dimensional Hubbard model

Note, that this little chapter is just a short, hand-waving, phenomenological paragraph on the Mott transition in the one-dimensional Hubbard model, since this effect does not play a role in the later investigations of this master thesis. It is just mentioned here for the sake of completeness. For the interested reader I refer to [19].
If we have a repulsion term larger than the kinetic energy ($U >> t$), then charge waves propagating through the chain are not energetically favorable any more, because this states experience an energy cost proportional to U. Minimizing the energy then leads to states, where the particles are localized on the lattice sites. For half filling ($n = L$) and large U one gets a chain with one particle on each site in the ground state. This is the reason, why no particle can travel through the lattice and the one-dimensional chain is an insulator. Actually, from the exact Bethe ansatz solution it is known, that large U is not needed for this effect [31]. At half-filling the one-dimensional Hubbard model is in the Mott phase at any finite value of U.

Doping the chain weakly away from half-filling either with holes ($n < L$) or with additional electrons ($n > L$) leads again to charge carriers proportional to the doping, because the holes/electrons can travel through the chain without feeling a repulsion and the chain is now a metal again.

The Mott phase transition also appears in figure 2.8. On the very right of this figure corresponding to half-filling at $n = 1$, one sees a rapid decrease of the charge velocities u_ρ to zero, indicating that the chain becomes insulating.

2.4 BCS model

2.4.1 History

As already mentioned before, Cooper pairs are responsible for superconductivity, where two fermions with half-integer, opposite spin characterized by the Fermi-Dirac statistics are bound together to form a boson, a particle with integer spin which obeys Bose-Einstein statistics and therefore admits superconductivity.

Since for the Andreev effect a metal-superconductor boundary is necessary, the last Hamiltonian presented in this master thesis is a Hamiltonian, which is capable of creating and annihilating such Cooper pairs, the Bardeen-Cooper-Schrieffer (BCS) Hamiltonian.

Although the phenomenon of superconductivity had been discovered in 1911 as Heike Kamerlingh Onnes[9] witnessed a sudden drop in the resistivity of mercury at low temperatures[10], a theoretical description of this effect had been a long time in coming. Another effect of superconductors, namely that they are perfect diamagnets, was discovered by Meissner and Ochsenfeld in 1933 [32]. In 1950 Maxwell and Reynolds found out, that the temperature T_c for the metal becoming a superconductor changes with its isotopic mass. An increase in the mass leads to a decrease in T_c [33, 34]. The finding of this isotope effect encouraged the assumption, that superconductivity depends on some interaction between electrons and phonons.

The BCS theory was introduced by J. Bardeen, L.N. Cooper and J.R. Schrieffer in 1957 [35] and has been the first consistent microscopic theory describing why superconductivity appears. The theory points out that binding of Cooper pairs will occur in the presence of an attractive potential, which is raised by lattice deformations, caused by phonon-electron interactions and therefore produced by the electrons themselves. Naturally this attractive force has to be greater than the repulsive Coulomb force, which two electrons experience under normal conditions.

2.4.2 Mathematical description

For the mathematical description of the BCS theory [35] we use second quantization. Since Cooper pairs consist of two electrons, which are fermionic particles, the creation/annihilation $\hat{c}^\dagger_{k\sigma}/\hat{c}_{k\sigma}$ operators of an electron with momentum k and spin σ obey fermionic anticom-

---

[9] Despite the uncommon first name Heike, H. K. Onnes is male.

[10] The transition temperature T_c of solid mercury is 4.2 K

mutation rules

$$\left\{\hat{c}_{k\sigma}, \hat{c}^\dagger_{k'\sigma'}\right\} = \hat{c}_{k\sigma}\hat{c}^\dagger_{k'\sigma'} + \hat{c}^\dagger_{k'\sigma'}\hat{c}_{k\sigma} = \delta_{k,k'}\ \delta_{\sigma,\sigma'} \tag{2.73}$$

$$\left\{\hat{c}_{k\sigma}, \hat{c}_{k'\sigma'}\right\} = \left\{\hat{c}^\dagger_{k\sigma}, \hat{c}^\dagger_{k'\sigma'}\right\} = 0 \quad . \tag{2.74}$$

The particle number operator $\hat{n}_{k,\sigma}$ counts electrons with momentum k and spin σ is again

$$\hat{n}_{k,\sigma} = \hat{c}^\dagger_{k\sigma}\hat{c}_{k\sigma} \quad . \tag{2.75}$$

We define a Pairing Hamiltonian

$$\hat{H} = \sum_{k\sigma}\epsilon_k\hat{n}_{k,\sigma} + \sum_{kl}V_{kl}\hat{c}^\dagger_{k\uparrow}\hat{c}^\dagger_{-k\downarrow}\hat{c}_{-l\downarrow}\hat{c}_{l\uparrow} \tag{2.76}$$

and identify the first term as the kinetic energy of the electrons and the second term as a phonon mediated electron-electron interaction. Despite the terms concerning not paired electrons are omitted, it should contain all the terms important for superconductivity.
Including a factor $-\mu N$, where μ is the chemical potential and N is the particle number, to shift the zero kinetic energy to μ (the Fermi energy E_F), leads to

$$\hat{H} - \mu N = \sum_{k\sigma}\xi_k\hat{n}_{k,\sigma} + \sum_{kl}V_{kl}\hat{c}^\dagger_{k\uparrow}\hat{c}^\dagger_{-k\downarrow}\hat{c}_{-l\downarrow}\hat{c}_{l\uparrow} \quad . \tag{2.77}$$

We perform a mean field approximation to simplify the matrix elements V_{kl}. For that reason we define

$$b_k \equiv \langle\hat{c}_{-k\downarrow}\hat{c}_{k\uparrow}\rangle \quad . \tag{2.78}$$

Due to the fact that there is large number of particles involved, fluctuations around this expectation value should be small. Now we express the product of the operators as

$$\hat{c}_{-k\downarrow}\hat{c}_{k\uparrow} = b_k + (\hat{c}_{-k\downarrow}\hat{c}_{k\uparrow} - b_k) \tag{2.79}$$

and neglect quantities which are bilinear in the presumably small fluctuation term in the parentheses above.
Plugging the equation above into equation 2.77 leads to the Hamiltonian

$$\hat{H} - \mu N = \sum_{k\sigma}\xi_k\hat{n}_{k,\sigma} + \sum_{kl}V_{kl}\left(\hat{c}^\dagger_{k\uparrow}\hat{c}^\dagger_{-k\downarrow}b_l + b^*_k\hat{c}_{-l\downarrow}\hat{c}_{l\uparrow} - b^*_k b_l\right) \quad . \tag{2.80}$$

Additionally inserting the gap energy Δ_k

$$\Delta_k = -\sum_l V_{kl}b_l = -\sum_l V_{kl}\langle\hat{c}_{-k\downarrow}\hat{c}_{k\uparrow}\rangle \quad , \tag{2.81}$$

one is left with the following equation

$$\hat{H} - \mu N = \sum_{k\sigma}\xi_k\hat{n}_{k,\sigma} - \sum_k\left(\Delta_k\hat{c}^\dagger_{k\uparrow}\hat{c}^\dagger_{-k\downarrow} + \Delta^*_k\hat{c}_{-l\downarrow}\hat{c}_{l\uparrow} - \Delta_k b^*_k\right) \quad . \tag{2.82}$$

Diagonalization of the Hamiltonian can be performed by the so-called Bogoliubov transformation [36]:

$$\hat{c}_{k\uparrow} = u^*_k\gamma_{k\uparrow} + v_k\gamma^\dagger_{-k\downarrow} \tag{2.83}$$

$$\hat{c}^\dagger_{-k\downarrow} = -v^*_k\gamma_{k\uparrow} + u_k\gamma^\dagger_{-k\downarrow} \tag{2.84}$$

with $|u_k|^2 + |v_k|^2 = 1$.
Inserting the new operators in equation 2.82 gives:

$$\begin{aligned}\hat{H} - \mu N = &\sum_k \xi_k \Big(\left(|u_k|^2 - |v_k|^2\right) \left(\gamma^\dagger_{k\uparrow}\gamma_{k\uparrow} + \gamma^\dagger_{-k\downarrow}\gamma_{-k\downarrow}\right) \\ &+ 2|v_k|^2 + 2u_k^* v_k^* \gamma_{-k\downarrow}\gamma_{k\uparrow} + 2u_k v_k \gamma^\dagger_{k\uparrow}\gamma^\dagger_{-k\downarrow}\Big) \\ &+ \sum_k \Big(\left(\Delta_k u_k v_k^* + \Delta_k^* u_k^* v_k\right) \left(\gamma^\dagger_{k\uparrow}\gamma_{k\uparrow} + \gamma^\dagger_{-k\downarrow}\gamma_{-k\downarrow} - 1\right) \\ &+ \left(\Delta_k v_k^{*2} - \Delta_k^* u_k^{*2}\right) \gamma_{-k\downarrow}\gamma_{k\uparrow} \\ &+ \left(\Delta_k^* v_k^{*2} - \Delta_k u_k^2\right) \gamma^\dagger_{k\uparrow}\gamma^\dagger_{-k\downarrow} + \Delta_k b_k^* \Big) \quad . \end{aligned} \tag{2.85}$$

If we choose u_k and v_k to eliminate terms with opposite spin ($\gamma_{-k\downarrow}\gamma_{k\uparrow}$ and $\gamma^\dagger_{k\uparrow}\gamma^\dagger_{-k\downarrow}$), we will find a formula for the new operators γ. This can be achieved, if the following term equals zero[11]

$$\begin{aligned} &2\xi_k u_k v_k + \Delta_k^* v_k^2 - \Delta_k u_k^2 = 0 \\ \Rightarrow\ &\frac{\Delta_k^* v_k}{u_k} = \sqrt{\xi_k^2 - |\Delta_k|^2} - \xi_k = E_k - \xi_k \quad , \end{aligned}$$

resulting in the coefficients

$$|v_k|^2 = 1 - |u_k|^2 = \frac{1}{2}\left(1 - \frac{\xi_k}{E_k}\right) \quad . \tag{2.86}$$

As ground state, Bardeen, Cooper and Schrieffer chose

$$|\Psi_G\rangle = \prod_k \left(u_k + v_k \hat{c}^\dagger_{k\uparrow}\hat{c}^\dagger_{-k\downarrow}\right)|0\rangle \quad . \tag{2.87}$$

In this equation one can identify $|v_k|^2$ as the occupation probability of a Cooper pair and $|u_k|^2 = 1 - |v_k|^2$ as its complementary probability, in other words, the probability of an unoccupied Cooper pair.
Taking a closer look at equation 2.87, one notices an explicit violation of the particle number conservation which is due to mean field approximation.

2.4.3 Model system

For later calculations we distinguish between the Hamiltonian of a s-wave and a p-wave BCS superconductor:

1. **s-wave superconductor**

$$\hat{H}_{\mathrm{BCS}} = \hat{H}_{\mathrm{HUB}} + \sum_{i=1}^{L} \gamma_i \left(\hat{c}^\dagger_{i,\uparrow}\hat{c}^\dagger_{i,\downarrow} + \hat{c}_{i,\uparrow}\hat{c}_{i,\downarrow}\right) \tag{2.88}$$

---

[11] If this term is zero, it holds also for its complex conjugated $2\xi_k u_k^* v_k^* + \Delta_k v_k^{*2} - \Delta_k^* u_k^{*2}$. Therefore all terms with opposite spin vanish in equation 2.85.

2. **p-wave superconductor**

$$\hat{H}_{\mathrm{BCS}} \;=\; \hat{H}_{\mathrm{HUB}} + \sum_{i=1}^{L-1} \Delta_i \left(\hat{c}^{\dagger}_{i,\uparrow}\hat{c}^{\dagger}_{i+1,\downarrow} + \hat{c}_{i+1,\downarrow}\hat{c}_{i,\uparrow}\right) \qquad (2.89)$$

As we can see, the s-wave Hamiltonian is capable of producing a Cooper pair on site i ($\hat{c}^{\dagger}_{i,\uparrow}\hat{c}^{\dagger}_{i,\downarrow}$) or destroying one ($\hat{c}_{i,\uparrow}\hat{c}_{i,\downarrow}$) with energy γ_i, whereas the p-wave Hamiltonian creates/annihilates ($\hat{c}^{\dagger}_{i,\uparrow}\hat{c}^{\dagger}_{i+1,\downarrow}/\hat{c}_{i+1,\uparrow}\hat{c}_{i,\downarrow}$) Cooper pairs on two sites in juxtaposition i and $i+1$ with energy Δ_i.
The configuration space is still the same as for the Hubbard model due to the Pauli principle, For every site it consists of an empty state, one state with spin up, one with spin down and a double occupied state consisting of two electrons with opposite spin($\{|0\rangle, |\uparrow\rangle, |\downarrow\rangle, |\uparrow\downarrow\rangle\}$). Analogous to the magnetic field term in the Hubbard Hamiltonian in 2.60 one can regard the parameters γ_i respectively Δ_i in equation 2.88 and 2.89 as some kind of a magnetic field for pair production.

3 Matrix Product States

This section starts at first with an introduction on MPS as a more local representation of general quantum states. Such MPS consist of a product of local matrices instead of a delocalized coefficient matrix.

Then a special matrix factorization, the singular value decomposition (SVD), is presented, followed by the Schmidt decomposition (SD) as a compact representation of bipartite quantum systems. The SD enables on the one hand a possibility for the calculation of the entanglement entropy of such bipartite systems and on the other hand a procedure, which makes the translation of the common representation of quantum states into the MPS representation possible.

Afterwards an other procedure to generate MPS by simply adding sites to a specific quantum state is showed, followed by the graphical representation of MPS, which makes the understanding of calculations in MPS language quite easier than just handling the plain and complex algebraic equations. This goes in hand with different normalization conditions fulfilled by diverse representations of MPS as right- and left-normalized MPS. Another representation is the canonical normal form, which reveals the Schmidt coefficients of all possible bipartitionings at once. It leads to a truncation procedure which keeps the computational cost linear with system size while still guaranteeing high accuracy at the same time.

After a short trip over the scaling of the entanglement with the dimension of the simulated system, showing that the computational effort is only bearable in one dimension, we see how to calculate norms, expectation values, the reduced density operator and how to apply operators on MPS. Then time is ready to present both DMRG algorithms, the one for infinite- and the one for finite-system sizes, and to perform time evolution with TEBD. Finally, two methods are outlined how to generate excitations to bring some dynamic for time evolution in the models.

To not reinvent the wheel the main part of this section is based on the more than helpful review on DMRG and MPS by Ulrich Schollwöck [9] and the former mentioned excellent master theses of my predecessors [16, 17, 18].

3.1 Short introduction to Matrix Product States

Consider an one-dimensional system with L-sites described by e.g. the Heisenberg (eq. 2.3) or the Hubbard (eq. 2.59) Hamiltonian with local Hilbert spaces $\{\sigma_i\}$ of dimension[1] d.

The most general pure quantum state will look like

$$|\psi\rangle = \sum_{\sigma_1,\ldots,\sigma_L} c_{\sigma_1,\ldots,\sigma_L} |\sigma_1,\ldots,\sigma_L\rangle \quad , \tag{3.1}$$

where $c_{\sigma_1,\ldots,\sigma_L}$ consists of exponentially many delocalized coefficients d^L.

The idea of matrix product states (MPS) is to find a more local representation of the state without destroying its quantum non-locality. This is possible by decomposing the d^L non-local coefficients $c_{\sigma_1,\ldots,\sigma_L}$ into a product of $d \cdot L$ local matrices A of dimension M:

$$|\psi\rangle = \sum_{\sigma_1,\ldots,\sigma_L} A^{\sigma_1} A^{\sigma_2} \cdots A^{\sigma_{L-1}} A^{\sigma_L} |\sigma_1,\ldots,\sigma_L\rangle \quad . \tag{3.2}$$

Here, A^{σ_1} and A^{σ_L} are just vectors, so that the complete product is a number. The benefit of this new representation of quantum states is that on the one hand it is possible to visualize complex calculations in graphical form. On the other hand it gives us the opportunity to a truncation procedure, which will keep the dimension of the $d \cdot L$ matrices fixed as we head to bigger and bigger system sizes. And last but not least it makes time evolution possible with so called quantum gates [12].

So how do we get the MPS-representation of the quantum state?

For that purpose we have to make an excursion to the field of linear algebra to get a mathematical tool, the Singular Value Decomposition (SVD), which opens the way for the conversion from equation 3.1 to equation 3.2.

3.2 Singular value and Schmidt decomposition

In linear algebra, SVD is a way to factorize a matrix. This matrix can be real or complex. Formally, the factorization of matrix M of size $(m \times n)$ is of the form

$$M = U \lambda V^\dagger \quad , \tag{3.3}$$

where U is a matrix of dimension $(m \times \min(m,n))$, $V^\dagger$ is a matrix of dimension $(\min(m,n) \times n)$ and λ is a diagonal square matrix of dimension $(\min(m,n) \times \min(m,n))$ with positive elements $\lambda_{ii} \in \mathbb{R}_0^+$, which are called the *singular values* of the matrix M. The number r of non-zero singular values is called the *rank of M* (see Figure 3.1). Furthermore U consists of orthogonal columns ($U^\dagger U = \mathbb{1}$), called *left singular vectors*, and $V^\dagger$ of orthonormal rows ($V^\dagger V = \mathbb{1}$), the so called *right singular vectors*.

---

[1] Remember that the local Hilbert space of the Heisenberg model has dimension $d = 2$ ($\{|\uparrow\rangle, |\downarrow\rangle\}$), whereas the Hubbard model is of local Hilbert space dimension $d = 4$ ($\{|0\rangle, |\uparrow\rangle, |\downarrow\rangle |\uparrow\downarrow\rangle\}$).

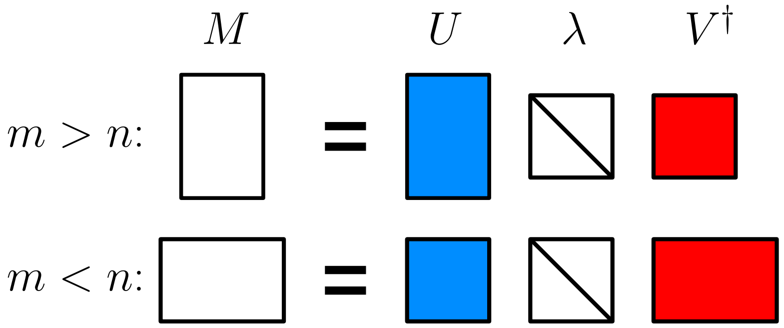

Figure 3.1: Resulting matrix shapes from a singular value decomposition (SVD), corresponding to the two rectangular shapes that can occur. The singular value diagonal serves as a reminder that in $M = U\lambda V^\dagger$ the matrix λ has a purely non-negative diagonal.

The SVD builds the basis for a compact representation of bipartite quantum states, the Schmidt decomposition (SD). Actually SD is only an SVD in a different context. Let us consider a many particle system consisting of two subsystems A and B. We can represent an arbitrary many body state ψ like in equation 3.1 in following way

$$|\psi\rangle = \sum_{\sigma_1,\ldots,\sigma_L} c_{\sigma_1,\ldots,\sigma_L}|\sigma_1,\ldots,\sigma_L\rangle = \sum_{\alpha\beta} c_{\alpha\beta}|\alpha\rangle|\beta\rangle \quad , \tag{3.4}$$

where $\{|\alpha\rangle\}$ and $\{|\beta\rangle\}$ are the orthonormal basis vectors of the subsystems A and B. This is always possible for a many body state as this is only an arbitrary virtual cut of the composite system $AB \Rightarrow A|B$ at a random site l and a relabeling of the indices $\alpha = (\sigma_1,\ldots,\sigma_l)$ and $\beta = (\sigma_{l+1},\ldots,\sigma_L)$.
The next step is an SVD of the coefficient matrix $c_{\alpha\beta}$ followed by a rearranging of the sums:

$$\begin{aligned}|\psi\rangle &= \sum_{\alpha\beta} c_{\alpha\beta}|\alpha\rangle|\beta\rangle \overset{\text{SVD}}{=} \sum_{\alpha\beta}\sum_{\gamma} U_{\alpha\gamma}\lambda_{\gamma\gamma}V^\dagger_{\gamma\beta}|\alpha\rangle|\beta\rangle = \\ &= \sum_{\gamma} \underbrace{\left(\sum_{\alpha} U_{\alpha\gamma}|\alpha\rangle\right)}_{|\Phi^A_\gamma\rangle} \lambda_{\gamma\gamma} \underbrace{\left(\sum_{\beta} V^\dagger_{\gamma\beta}|\beta\rangle\right)}_{|\Phi^B_\gamma\rangle} = \sum_{\gamma} \lambda_{\gamma\gamma}|\Phi^A_\gamma\rangle|\Phi^B_\gamma\rangle \quad .\end{aligned} \tag{3.5}$$

The sum over γ in equation 3.5 goes from $\gamma = 1$ to the minimum of the dimensions of the two subsystems $\gamma = \min(\dim A, \dim B)$. The basis $|\Phi^A_\gamma\rangle$ and $|\Phi^B_\gamma\rangle$ are orthonormal basis sets of A and B through the orthonormality of U respectively $V^\dagger$. Running the sum only over the r non-zero values of γ gives us the Schmidt decomposition of a quantum state

$$|\psi\rangle = \sum_{\gamma=1}^{r} \lambda_{\gamma\gamma}|\Phi^A_\gamma\rangle|\Phi^B_\gamma\rangle \quad , \tag{3.6}$$

where $r = 1$ gives us a product state and $r \geq 1$ leads to an entangled quantum state.
Furthermore, one can show that the Schmidt coefficients retain following normalization condition

$$\sum_{\gamma=1}^{r} (\lambda_{\gamma\gamma})^2 = 1 \quad . \tag{3.7}$$

First we have to show the orthonormality of the basis $|\Phi^A_\gamma\rangle$ for subsystem A:

$$\langle\Phi^A_{\gamma'}|\Phi^A_\gamma\rangle = \sum_{\alpha\alpha'} U^\dagger_{\gamma'\alpha'} U_{\alpha\gamma} \underbrace{\langle\alpha'|\alpha\rangle}_{\delta_{\alpha,\alpha'}} = \sum_{\alpha} U^\dagger_{\gamma'\alpha} U_{\alpha\gamma} = \delta_{\gamma,\gamma'} \quad . \tag{3.8}$$

$\langle\alpha'|\alpha\rangle = \delta_{\alpha,\alpha'}$ holds because of the orthonormality of the states $|\alpha\rangle$ and $|\beta\rangle$, whereas the last conversion holds due to the unity properties of the SVD. The basis of subsystem B is orthonormal too:

$$\langle\Phi^B_{\gamma'}|\Phi^B_\gamma\rangle = \sum_{\beta\beta'} V_{\beta'\gamma'} V^\dagger_{\gamma\beta} \underbrace{\langle\beta'|\beta\rangle}_{\delta_{\beta,\beta'}} = \sum_{\beta} V^\dagger_{\gamma\beta} V_{\beta\gamma'} = \delta_{\gamma,\gamma'} \quad . \tag{3.9}$$

Now we are able to deduce equation 3.7:

$$\langle\psi|\psi\rangle = \sum_{\gamma\gamma'} \lambda_{\gamma'\gamma'}\lambda_{\gamma\gamma} \underbrace{\left(\langle\Phi^B_{\gamma'}|\langle\Phi^A_{\gamma'}|\right)\left(|\Phi^A_\gamma\rangle|\Phi^B_\gamma\rangle\right)}_{\delta_{\gamma,\gamma'}} = \sum_\gamma \lambda^2_{\gamma\gamma} = 1 \quad . \tag{3.10}$$

3.3 Entanglement measurements in bipartite systems

As a measure for the uncertainty of the quantum state one can take the so called von Neumann or entanglement entropy S_N

$$S_N = -\operatorname{Tr}\rho\log\rho \quad , \tag{3.11}$$

with ρ the density matrix of the system and Tr the trace of the matrix. The von Neumann entropy is the extension of classical entropy concepts like the Shannon entropy to the field of quantum mechanics. For the logarithm we will use the logarithm of base 2.[2]

Our composite system consisting of the two subsystems A and B is described by the density matrix ρ_{AB}. It is possible to just describe parts of the quantum system if we take the partial trace over one subsystem. For example we get the state of subsystem A if we take the partial trace of the density matrix of the composite system ρ_{AB} only over subsystem B, and vice versa

$$\rho_A = \operatorname{Tr}_B \rho_{AB} \quad , \quad \rho_B = \operatorname{Tr}_A \rho_{AB} \quad . \tag{3.12}$$

Note that if we get the state of one subsystem, we don't have any information about the other.

By help of the Schmidt Decomposition of state $|\psi\rangle$ it is easy to read off the reduced density operators of the subsystems by only carrying out the partial traces

$$\rho_A = \sum_{\gamma=1}^{r} \lambda^2_{\gamma\gamma}|\Phi^A_\gamma\rangle\langle\Phi^A_\gamma| \quad , \quad \rho_B = \sum_{\gamma=1}^{r} \lambda^2_{\gamma\gamma}|\Phi^B_\gamma\rangle\langle\Phi^B_\gamma| \quad . \tag{3.13}$$

One can see that ρ_A and ρ_B share the same eigenvalues, which are the squares of the singular values, but don't have the same eigenstates.

---

[2] Note that in literature there is no standard convention on which logarithm one should use. So attention has to be paid, if one compares results involving entanglement entropy of different sources.

This gives us the possibility to calculate the von Neumann entropy for the subsystems A or B by performing a Schmidt decomposition

$$S_N \;=\; -\operatorname{Tr}\rho_A \log \rho_A \;=\; -\sum_{\gamma=1}^{r} \lambda_{\gamma\gamma}^2 \log \lambda_{\gamma\gamma}^2 \quad . \tag{3.14}$$

The entanglement entropy becomes maximal with equal eigenvalues. When the eigenvalues are all equal with equation 3.7 one obtains an upper bound for the entanglement entropy $\overline{S}_N$ depending on the rank r of the Schmidt decomposition

$$\overline{S}_N = \log(r) \quad . \tag{3.15}$$

This gives us the possibility to measure the entanglement entropy with the help of the singular values obtained by a Schmidt decomposition.

3.4 Construction of Matrix Product States

There are two possible ways to construct a matrix product state. First, one can decompose an arbitrary quantum state of an L-site one-dimensional quantum system by the Schmidt decomposition of its coefficient matrix (see 3.4.1).
And second, the construction of a matrix product state of a L site system is also possible by adding additional sites to a system with smaller system size $l < L$ (3.4.2) which has been decomposed before.

3.4.1 Schmidt decomposition of a quantum state

The starting point for the first way to construct an MPS is the quantum state in equation 3.1.
The first step is to rearrange the d^L-coefficients in a $(d \times d^{L-1})$-matrix and subsequently performing a singular value decomposition

$$c_{\sigma_1,\dots,\sigma_L} \;=\; c_{\sigma_1,(\sigma_2,\dots,\sigma_L)} \overset{\text{SVD}}{=} \sum_{a_1}^{r_1} U_{\sigma_1,a_1} \underbrace{\lambda_{a_1,a_1} V^\dagger_{a_1,(\sigma_2,\dots,\sigma_L)}}_{c_{a_1,\dots,\sigma_L}} \;\equiv\; \sum_{a_1}^{r_1} U_{\sigma_1,a_1} c_{a_1,\sigma_2,\dots,\sigma_L} \quad . \tag{3.16}$$

In the last step λ_{a_1,a_1} and $V^\dagger_{a_1,(\sigma_2,\dots,\sigma_L)}$ were multiplied and reshaped back into the vector $c_{a_1,\sigma_2,\dots,\sigma_L}$. The rank is now $r_1 \leq d$
For a more common representation of an MPS we just rename the matrix U_{σ_1,a_1} into a row vector $A^{\sigma_1}_{a_1}$

$$c_{\sigma_1,\dots,\sigma_L} \;=\; \sum_{a_1}^{r_1} A^{\sigma_1}_{a_1} c_{a_1,\sigma_2,\dots,\sigma_L} \quad . \tag{3.17}$$

Now we can apply the same steps as before on the new coefficient matrix $c_{a_1,\sigma_2,\dots,\sigma_L}$ by reshaping it into the $(r_1 d \times d^{L-2})$-matrix and performing again an SVD

$$c_{a_1,\sigma_2,\dots,\sigma_L} \;=\; c_{(a_1\sigma_2),(\sigma_3,\dots,\sigma_L)} = \sum_{a_2}^{r_2} A^{\sigma_2}_{a_1,a_2} c_{a_2,\sigma_3,\dots,\sigma_L} \quad . \tag{3.18}$$

Connecting equation 3.17 and 3.18 yields

$$c_{\sigma_1,\ldots,\sigma_L} = \sum_{a_1}^{r_1}\sum_{a_2}^{r_2} A^{\sigma_1}_{a_1} A^{\sigma_2}_{a_1,a_2}\, c_{a_2,\sigma_3,\ldots,\sigma_L} \quad . \tag{3.19}$$

Upon further SVDs we get the result

$$\begin{aligned} c_{\sigma_1,\ldots,\sigma_L} &= \sum_{a_1}^{r_1}\sum_{a_2}^{r_2}\cdots\sum_{a_{L-2}}^{r_{L-2}}\sum_{a_{L-1}}^{r_{L-1}} A^{\sigma_1}_{a_1} A^{\sigma_2}_{a_1,a_2}\ldots A^{\sigma_{L-1}}_{a_{L-2},a_{L-1}} A^{\sigma_L}_{a_{L-1}} && (3.20)\\ &\equiv A^{\sigma_1}A^{\sigma_2}\ldots A^{\sigma_{L-1}}A^{\sigma_L} \quad . && (3.21)\end{aligned}$$

In the last line we identified the sums over a_1 to a_L as simple matrix multiplications. The general non-local quantum state is now represented exactly as a product of L local matrices

$$|\psi\rangle = \sum_{\sigma_1,\ldots,\sigma_L} A^{\sigma_1}A^{\sigma_2}\ldots A^{\sigma_{L-1}}A^{\sigma_L}|\sigma_1,\ldots,\sigma_L\rangle \quad , \tag{3.22}$$

as we desired before. This is the matrix product state (MPS) representation of the arbitrary quantum state.
The dimension of the matrices for even L from the left to the right will maximally be

$$\underbrace{(1\times d)}_{A^{\sigma_1}},\underbrace{(d\times d^2)}_{A^{\sigma_2}},\ldots,\underbrace{(d^{\frac{L}{2}-1}\times d^{\frac{L}{2}})}_{A^{\sigma_{L/2}}},\underbrace{(d^{\frac{L}{2}}\times d^{\frac{L}{2}-1})}_{A^{\sigma_{L/2+1}}},\ldots,\underbrace{(d^2\times d)}_{A^{\sigma_{L-1}}},\underbrace{(d\times 1)}_{A^{\sigma_L}}$$

and for odd L:

$$\underbrace{(1\times d)}_{A^{\sigma_1}},\underbrace{(d\times d^2)}_{A^{\sigma_2}},\ldots,\underbrace{(d^{\frac{L}{2}}\times d^{\frac{L}{2}})}_{A^{\sigma_{L/2}}},\ldots,\underbrace{(d^2\times d)}_{A^{\sigma_{L-1}}},\underbrace{(d\times 1)}_{A^{\sigma_L}} \quad .$$

Because of the properties of the U-matrices due to the Schmidt decomposition

$$U^\dagger U = \mathbb{1}$$

following relationship holds for the A-matrices

$$\delta_{a_l,a_l'} = \sum_{a_{l-1},\sigma_l} U^\dagger_{a_l,(a_{l-1}\sigma_l)} U_{(a_{l-1}\sigma_l),a_l'} = \sum_{a_{l-1},\sigma_l} A^{\sigma_l\dagger}_{a_l,a_{l-1}} A^{\sigma_l}_{a_{l-1},a_l} = \sum_{\sigma_l}\left(A^{\sigma_l\dagger}A^{\sigma_l}\right)_{a_l,a_l'} \quad , \tag{3.23}$$

or more succinct

$$\sum_{\sigma_l} A^{\sigma_l\dagger}A^{\sigma_l} = \mathbb{1} \quad . \tag{3.24}$$

Due to the equation above and the fact that we have used only the left singular vectors U of the SVD, we will call the A-matrices *left-normalized* and an MPS, which only consist of *left-normalized* matrices, a *left-canonical* MPS.
We can also construct a matrix product state instead of decomposing the coefficients from left to right by decomposition from right to left. To this end, we have to start on the

right site of the coefficient matrix $c_{\sigma_1,\dots,\sigma_L}$ by rearranging it to a $(d^{L-1} \times d)$-matrix and performing an SVD and repeating these steps L times

$$\begin{aligned}
c_{\sigma_1,\dots,\sigma_L} &= c_{(\sigma_1,\dots,\sigma_{L-1}),\sigma_L} \overset{\text{SVD}}{=} \sum_{a_{L-1}}^{r_{L-1}} U_{(\sigma_1,\dots,\sigma_{L-1}),a_{L-1}} \lambda_{a_{L-1},a_{L-1}} V^\dagger_{a_{L-1},\sigma_L} \\
&= \sum_{a_{L-1}}^{r_{L-1}} c_{(\sigma_1,\dots,\sigma_{L-2}),(\sigma_{L-1},a_{L-1})} B^{\sigma_L}_{a_{L-1}} \\
&= \sum_{a_{L-2}}^{r_{L-2}} \sum_{a_{L-1}}^{r_{L-1}} U_{(\sigma_1,\dots,\sigma_{L-2}),a_{L-2}} \lambda_{a_{L-2},a_{L-2}} V^\dagger_{a_{L-2},(\sigma_{L-1}a_{L-1})} B^{\sigma_L}_{a_{L-1}} \\
&= \sum_{a_{L-2}}^{r_{L-2}} \sum_{a_{L-1}}^{r_{L-1}} c_{(\sigma_1,\dots,\sigma_{L-3}),(\sigma_{L-2},a_{L-2})} B^{\sigma_{L-1}}_{a_{L-2},a_{L-1}} B^{\sigma_L}_{a_{L-1}} \\
&= \dots = \sum_{a_1,\dots,a_{L-1}} B^{\sigma_1}_{a_1} B^{\sigma_2}_{a_1,a_2} \dots B^{\sigma_{L-1}}_{a_{L-2},a_{L-1}} B^{\sigma_{L-1}}_{a_{L-1}}
\end{aligned}$$

At each step, U and λ are multiplied before the product is reshaped into c, $V^\dagger_{a_{L-1},\sigma_L}$ is reshaped into d column vectors $B^{\sigma_L}_{a_{L-1}}$ and $V^\dagger_{a_{L-i},(a_{L-j},\sigma_j)}$ into d matrices $B^{\sigma_{L-j}}_{a_{L-i},a_{L-j}}$. Therefore we get for the overall quantum state the representation

$$|\psi\rangle = \sum_{\sigma_1,\dots,\sigma_L} B^{\sigma_1} B^{\sigma_2} \dots B^{\sigma_{L-1}} B^{\sigma_L} |\sigma_1,\dots,\sigma_L\rangle \quad . \tag{3.25}$$

Referring to equation 3.24, and since $V^\dagger V = \mathbb{1}$, we get following equation for the B-matrices

$$\sum_{\sigma_l} B^{\sigma_l} B^{\sigma_l \dagger} = \mathbb{1} \quad . \tag{3.26}$$

Accordingly we will call the B-matrices *right-normalized* and an MPS consisting only of *right-normalized* matrices a *right-canonical* MPS.
Furthermore, construction of an MPS from the left with A- matrices until site l and subsequently construction from the right with B-matrices from site L to site $l+1$ leads to a *mixed-canonical* MPS:

$$|\psi\rangle = \sum_{a_l} \left(\sum_{\sigma_1,\dots,\sigma_l} A^{\sigma_1} A^{\sigma_2} \dots A^{\sigma_l} \right)_{1,a_l} \lambda_{a_l,a_l} \left(\sum_{\sigma_{l+1},\dots,\sigma_L} B^{\sigma_{l+1}} B^{\sigma_{l+2}} \dots B^{\sigma_L} \right)_{a_l,1} |\sigma_1,\dots,\sigma_L\rangle \quad . \tag{3.27}$$

Due to rearranging and applying

$$\begin{aligned}
|\Phi^A_{a_l}\rangle &= \sum_{\sigma_1,\dots,\sigma_l} A^{\sigma_1} A^{\sigma_2} \dots A^{\sigma_l} |\sigma_1,\dots,\sigma_l\rangle \\
|\Phi^B_{a_l}\rangle &= \sum_{\sigma_{l+1},\dots,\sigma_L} B^{\sigma_{l+1}} B^{\sigma_{l+2}} \dots B^{\sigma_L} |\sigma_{l+1},\dots,\sigma_L\rangle
\end{aligned}$$

it is obvious that this is the Schmidt-decomposition of the Bipartite quantum system resulting from a cut at site l

$$|\psi\rangle = \sum_{a_l} \lambda_{a_l,a_l} |\Phi^A_{a_l}\rangle |\Phi^B_{a_l}\rangle \quad . \tag{3.28}$$

Note that MPS are not unique. This can be shown by inserting an identity $\mathbb{1} = M^{-1}M$:

$$A^{\sigma_l}A^{\sigma_{l+1}} = A^{\sigma_l}\mathbb{1}A^{\sigma_{l+1}} = A^{\sigma_l}\left(M^{-1}M\right)A^{\sigma_{l+1}} = \underbrace{\left(A^{\sigma_l}\ M^{-1}\right)}_{\tilde{A}^{\sigma_l}}\underbrace{\left(M\ A^{\sigma_{l+1}}\right)}_{\tilde{A}^{\sigma_{l+1}}} = \tilde{A}^{\sigma_l}\tilde{A}^{\sigma_{l+1}} \quad .$$

3.4.2 Adding sites to Hilbert space of dimension M

Suppose we have a set of basis vectors $\{|a_{l-1}\rangle\}$ on a $(l-1)$-site Hilbert space of dimension M. Now we want to add an orthonormal basis vector of a one-site subsystem of dimension d of the local Hilbert space to this set of basis vectors (see figure 3.2). This can be achieved by a general basis transformation:

$$|a_l\rangle = \sum_{(a_{l-1},\sigma_l)} U_{a_l,(a_{l-1},\sigma_l)}|a_{l-1}\rangle \otimes |\sigma_l\rangle \quad ,$$

where the resulting basis vectors $|a_l\rangle$ are of dimension dM.

If $|a_{l-1}\rangle$ and $|\sigma_l\rangle$ are orthonormal, the unitary condition $U^\dagger U = \mathbb{1}$ holds. We can rewrite the previous equation to get the familiar representation of a A-matrix in the language of MPS:

$$|a_l\rangle = \sum_{\sigma_l}^{d}\sum_{a_{l-1}}^{M} A^{\sigma_l}_{a_{l-1},a_l}|a_{l-1}\rangle \otimes |\sigma_l\rangle \quad .$$

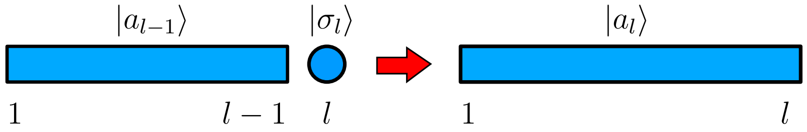

Figure 3.2: A block of length $l-1$ is grown towards the right to a block of length l by adding a site l.

If we start with a single site system and add site by site with this procedure we get the same MPS representation as in equation 3.22.

3.5 Graphical representation of an MPS

A tremendous advantage of MPS is the graphical representation of such states, which helps to understand calculations much easier than just looking at the plain formulas.

As seen before, an MPS consists of A- or B-matrices with several indices. We will call the indices written in Greek letters the *physical indices*, whereas the indices with Latin letters are called *virtual indices*. In figure 3.3 you can see the graphical representation of such A-matrices with physical and virtual indices at different positions of an MPS and also the complex conjugated $A^{\sigma_i *}$, which one gets by just flipping the normal MPS upside down.

In figure 3.4 one can see the graphical representation of a tensor contraction (i.e., a matrix multiplication), which is only the sum over a virtual index to connect two A-matrices[3]. Performing diverse tensor contractions leads to the MPS-representation in figure 3.5.

The graphical representation of equation 3.23 and the corresponding relation for B-matrices is presented in figure 3.7.

The iterative construction of an exact MPS representation from an arbitrary quantum state, as explained in section 3.4.1, is represented in figure 3.8.

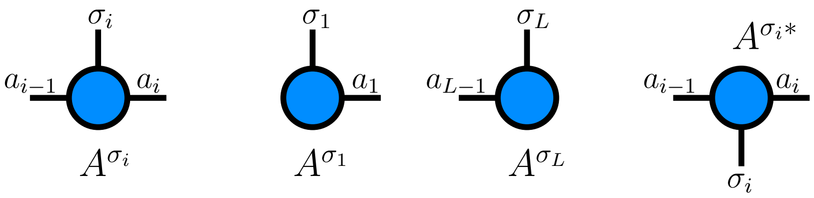

Figure 3.3: Graphical representation of MPS matrices on different sites of the MPS. A^{σ_i} is a matrix somewhere in the middle with one physical index (σ_i) and two virtual ones (a_{i-1}, a_i). A^{σ_1} and A^{σ_L} are the matrices on the boundaries with only one physical and virtual index and $A^{\sigma_i *}$ is the graphical representation of the complex conjugated of A^{σ_i}.

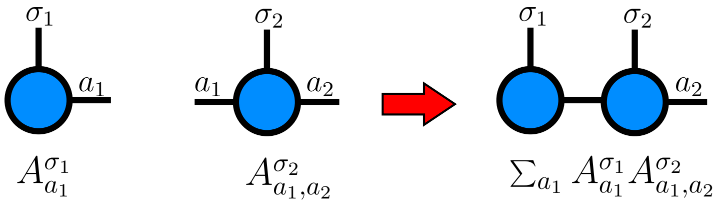

Figure 3.4: Graphical representation of a tensor contraction of matrices A^{σ_1} and A^{σ_2} over the virtual index a_1.

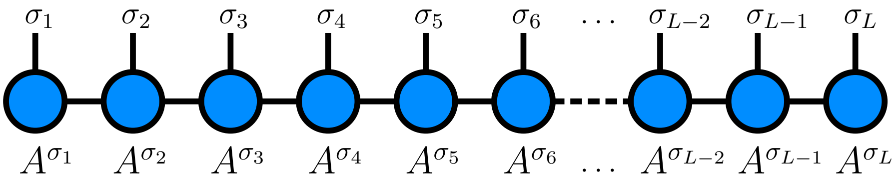

Figure 3.5: Graphical representation of an open boundary condition left-canonical MPS.

---

[3] Please note: Connecting two matrices over one index is always achieved by taking the sum over this index.

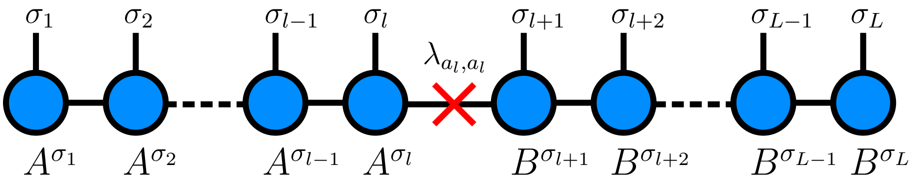

Figure 3.6: This figure shows a mixed-canonical state for open boundary conditions consisting of l left-normalized A-matrices, $L-l$ right-normalized B-matrices and the Schmidt-coefficient matrix λ in the middle (red cross).

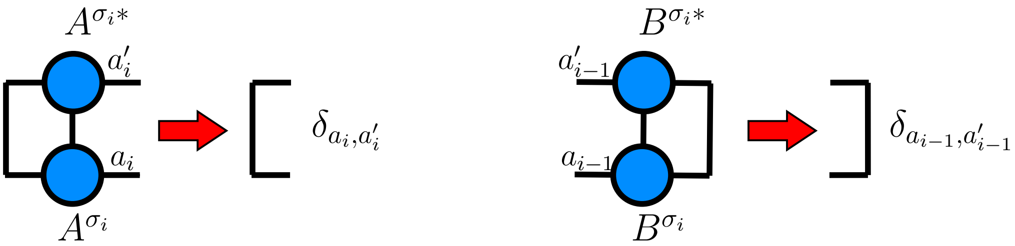

Figure 3.7: If two left-normalized A-matrices are contracted over their left index and the physical indices, a Kronecker delta δ_{a_i,a'_i} results. The same happens for the contraction of two right-normalized B-matrices over their right index.

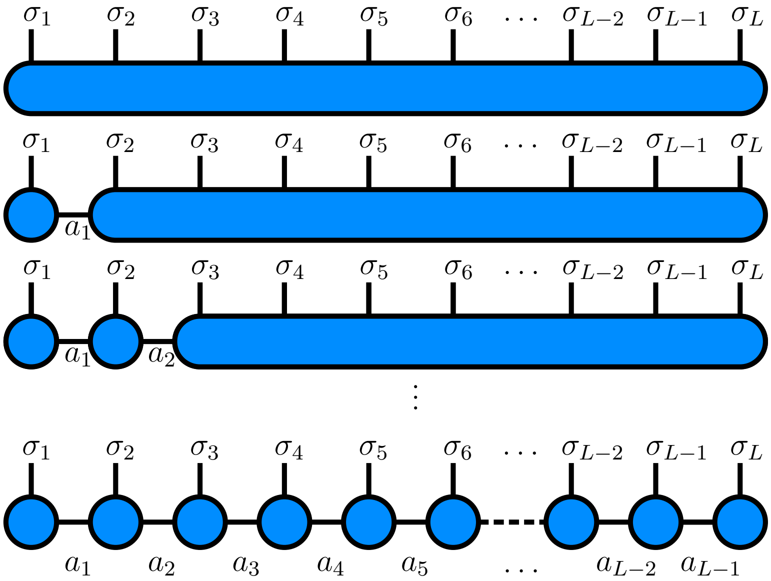

Figure 3.8: Graphical representation of an iterative construction of an exact MPS representation of an arbitrary quantum state by a sequence of singular value decompositions of the coefficient matrix $c_{\sigma_1 \ldots \sigma_L}$. The first row represents the coefficient matrix $c_{\sigma_1 \ldots \sigma_L}$ and in every line a A-matrix is projected out until one gets the MPS representation in the last line.

3.6 From MPS to the canonical normal form

In section 3.3 we saw that the entanglement entropy of a bipartite system S_N is related to the λ-values of the Schmidt decomposition (see equation 3.14). So a representation of a one-dimensional quantum system of length L, where one has the possibility to simply read off all $(L-1)$ bipartitionings of the system, would be highly convenient.
Such a representation was first introduced by Guifré Vidal in 2003 [11], the canonical normal form:

$$|\psi\rangle = \sum_{\sigma_1,\dots,\sigma_L} \Gamma^{\sigma_1}\lambda^{[1]}\Gamma^{\sigma_2}\lambda^{[2]}\Gamma^{\sigma_3}\lambda^{[3]}\dots\lambda^{[L-1]}\Gamma^{\sigma_L}|\sigma_1\dots\sigma_L\rangle \quad . \tag{3.29}$$

Γ^{σ_l} are a set of d matrices and $\lambda^{[l]}$ is a diagonal matrix containing the Schmidt coefficients on site l.
To derive this equation we start with a Schmidt decomposition at bond 1

$$|\psi\rangle = \sum_{a_1}^{\chi_1} \lambda^{[1]}_{a_1,a_1}|\Phi^{[1]}_{a_1}\rangle \otimes |\Phi^{[2\dots L]}_{a_1}\rangle \quad ,$$

where $\left\{|\Phi^{[1]}_{a_1}\rangle\right\}$ is the basis vector set of the first site on the left and $\left\{|\Phi^{[2\dots L]}_{a_1}\rangle\right\}$ is the basis vector set of the $(L-1)$ sites on the right. Now we rewrite the basis vectors on the left

$$|\Phi^{[1]}_{a_1}\rangle = \sum_{\sigma_1}^{d_1} \Gamma^{\sigma_1}_{a_1}|\sigma_1\rangle \quad .$$

This gives us

$$|\psi\rangle = \sum_{\sigma_1}^{d_1}\sum_{a_1}^{\chi_1} \Gamma^{\sigma_1}_{a_1}\lambda^{[1]}_{a_1,a_1}|\sigma_1\rangle \otimes |\Phi^{[2\dots L]}_{a_1}\rangle \quad . \tag{3.30}$$

On the other hand rewriting of the basis sets on the right site leads to

$$|\Phi^{[2\dots L]}_{a_1}\rangle = \sum_{\sigma_2}^{d_2} |\sigma_2\rangle \otimes |\tilde{\Phi}^{[3\dots L]}_{a_1,\sigma_1}\rangle \quad ,$$

where the basis vector set $\left\{|\tilde{\Phi}^{[3\dots L]}_{a_1,\sigma_1}\rangle\right\}$ corresponds to some unnormalized vectors.
The next step is the Schmidt decomposition at the second bond

$$|\tilde{\Phi}^{[3\dots L]}_{a_1,\sigma_1}\rangle = \sum_{a_2}^{\chi_2} \Gamma^{\sigma_2}_{a_1,a_2}\lambda^{[2]}_{a_2,a_2}|\Phi^{[3\dots L]}_{a_2}\rangle \quad .$$

Plugging this intermediate result into equation 3.30 gets us to

$$|\psi\rangle = \sum_{\sigma_1}^{d_1}\sum_{\sigma_2}^{d_2}\sum_{a_1}^{\chi_1}\sum_{a_2}^{\chi_2} \Gamma^{\sigma_1}_{a_1}\lambda^{[1]}_{a_1,a_1}\Gamma^{\sigma_2}_{a_1,a_2}\lambda^{[2]}_{a_2,a_2}|\sigma_1\rangle \otimes |\sigma_2\rangle \otimes |\Phi^{[3\dots L]}_{a_2}\rangle \quad .$$

In general we get for this procedure on bond l

$$|\Phi^{[l\dots L]}_{a_{l-1}}\rangle = \sum_{\sigma_l}^{d_l} |\sigma_l\rangle \otimes |\tilde{\Phi}^{[l\dots L]}_{a_{l-1},\sigma_l}\rangle$$

$$|\tilde{\Phi}^{[l+1\dots L]}_{a_{l-1},\sigma_l}\rangle = \sum_{a_l}^{\chi_l} \Gamma^{\sigma_l}_{a_{l-1},a_l}\lambda^{[l]}_{a_l,a_l}|\Phi^{[l+1\dots L]}_{a_l}\rangle \quad .$$

After iteration over all $(L-1)$ bonds we obtain as result the canonical normal form:

$$|\psi\rangle = \sum_{\sigma_1 \ldots \sigma_L} \left(\sum_{a_1}^{\chi_1} \sum_{a_2}^{\chi_2} \ldots \sum_{a_{L-1}}^{\chi_{L-1}} \Gamma^{\sigma_1}_{a_1} \lambda^{[1]}_{a_1,a_1} \Gamma^{\sigma_2}_{a_1,a_2} \lambda^{[2]}_{a_2,a_2} \ldots \lambda^{[L-1]}_{a_{L-1},a_{L-1}} \Gamma^{\sigma_L}_{a_{L-1}} \right) |\sigma_1 \sigma_2 \ldots \sigma_L\rangle \quad .$$

Performing the simple matrix multiplications represented as the inner sums of the equation above gives us exactly equation 3.29. □

Comparison with equation 3.2 or 3.25 and with $\lambda^{[0]} = \lambda^{[L]} = 1$ leads to the following equation

$$A^{\sigma_l} = \lambda^{[l-1]} \Gamma^{\sigma_l} \quad \text{resp.} \quad B^{\sigma_l} = \Gamma^{\sigma_l} \lambda^{[l]} \quad . \tag{3.31}$$

With the orthonormal basis sets $|\Phi^A_{a_l}\rangle$ and $|\Phi^B_{a_l}\rangle$ of the subsystems A and B resulting from a cut at bond l

$$|\Phi^A_{a_l}\rangle = \sum_{\sigma_1,\ldots,\sigma_l} \left(\Gamma^{\sigma_1} \lambda^{[1]} \Gamma^{\sigma_2} \ldots \lambda^{[l-1]} \Gamma^{\sigma_l} \right) |\sigma_1, \sigma_2, \ldots, \sigma_l\rangle$$

$$|\Phi^B_{a_l}\rangle = \sum_{\sigma_{l+1},\ldots,\sigma_L} \left(\Gamma^{\sigma_{l+1}} \lambda^{[l+1]} \Gamma^{\sigma_{l+2}} \ldots \lambda^{[L-1]} \Gamma^{\sigma_L} \right) |\sigma_{l+1}, \sigma_{l+2}, \ldots, \sigma_L\rangle$$

one can see that the $\lambda^{[l]}$-matrices are indeed the diagonal Schmidt-matrices

$$|\psi\rangle = \sum_{a_l}^{\chi_l} \lambda^{[l]}_{a_l,a_l} |\Phi^A_{a_l}\rangle |\Phi^B_{a_l}\rangle \quad ,$$

the squares of which are directly connected to the entanglement entropy S_N (equation 3.14). This is also the representation of a *mixed-canonical* MPS as represented in equation 3.28. In figure 3.9 one can find the graphical representation of a canonical MPS.

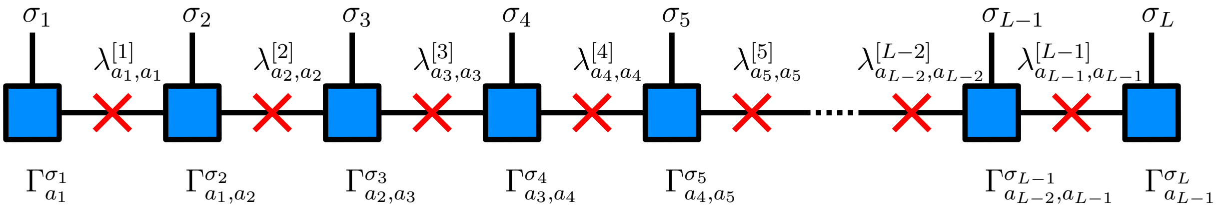

Figure 3.9: Graphical representation of the canonical normal form of an MPS. This representation contains on every bond l directly the Schmidt singular values $\lambda^{[l]}$ (red crosses) of a Schmidt decomposition and the Γ-matrices (blue squares).

Normalization conditions

With the left- and right normalization conditions in equation 3.24 and 3.26 and the connections between the A-, B-, Γ- and λ-matrices in equation 3.31, the normalization conditions simply translate to:

$$\mathbb{1} = \sum_{\sigma_l} A^{\sigma_l \dagger} A^{\sigma_l} = \sum_{\sigma_l} \left(\Gamma^{\sigma_l \dagger} \lambda^{[l-1] \dagger} \right) \left(\lambda^{[l-1]} \Gamma^{\sigma_l} \right) = \sum_{\sigma_l} \Gamma^{\sigma_l \dagger} \left(\lambda^{[l-1]} \right)^2 \Gamma^{\sigma_l} \tag{3.32}$$

$$\mathbb{1} = \sum_{\sigma_l} B^{\sigma_l} B^{\sigma_l \dagger} = \sum_{\sigma_l} \left(\Gamma^{\sigma_l} \lambda^{[l]} \right) \left(\lambda^{[l] \dagger} \Gamma^{\sigma_l \dagger} \right) = \sum_{\sigma_l} \Gamma^{\sigma_l} \left(\lambda^{[l]} \right)^2 \Gamma^{\sigma_l \dagger} \quad . \tag{3.33}$$

A graphical representation similar to figure 3.7 can be found in 3.10.

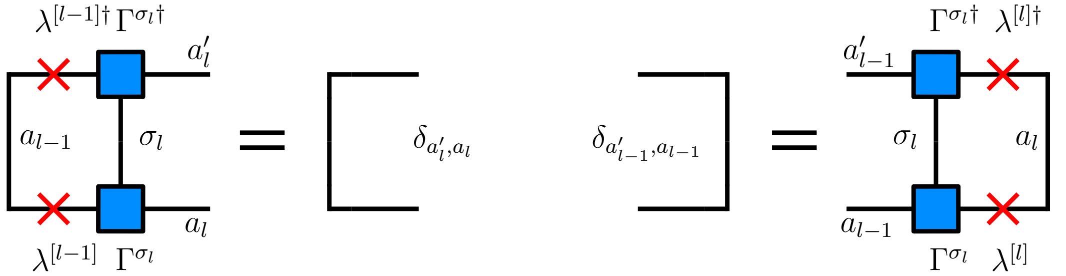

Figure 3.10: Normalization conditions of a canonical MPS similar to figure 3.7 for the A- and B-matrices. The left part of this figure is the representation of equation 3.32, the right part of 3.33.

3.6.1 Truncation process - truncated weight

Up to now every calculation was exact in the sense that there was no information loss when we transformed a quantum state like in equation 3.1 into an MPS, whether it is of *left*-, *right*-, *mixed-canonical* or *canonical-normal* form.
This was achieved with one big drawback, namely that the transformed basis sets $|\Phi^A_{a_l}\rangle$ and $|\Phi^B_{a_l}\rangle$ grow exponentially with system size L, to order $\mathcal{O}(d^{L/2})$ where d is the dimension of the single particle Hilbert space. As shown before in section 3.4.1 the matrices of an MPS grow from the boundary to the middle, so that the $l-$th matrix is of size $(d^{l-1} \times d^l)$. In general there are $2 \cdot L \cdot \sum_{i=1}^{L/2} d^{2i-1}$ single numbers to be saved for an exact MPS.
This means that to store an MPS, we need to store at least $\mathcal{O}(L \cdot d^L)$ numbers, which is in fact greater than the $\mathcal{O}(d^L)$ coefficients of equation 3.1. So what is the way out of this dilemma?
The idea is to limit the matrix dimension of the single matrices in an MPS by some upper bound χ , trimming all matrices of greater dimension to matrices of that desired maximum dimension. This can be achieved while performing an SVD, taking only the first χ left and right singular vectors *corresponding to the* χ *largest Schmidt values* and the first χ columns of U, respectively the first χ rows of $V^\dagger$. This means that the maximum size of a matrix in the MPS is χ, which means that the numerical effort drops from $\mathcal{O}(L \cdot d^L)$ to $\mathcal{O}(L \cdot \min(d^L, \chi^2))$ growing only linearly with system size contrary to exponentially as before (see figure 3.11).
Due to the fact that we have dumped the smallest Schmidt coefficients in the step before, one has to renormalize the surviving Schmidt coefficients:

$$\tilde{\lambda}^{[l]}_{a_l,a_l} = \frac{1}{Z}\lambda^{[l]}_{a_l,a_l} \quad , \tag{3.34}$$

with Z the euclidian norm over all remaining Schmidt coefficients

$$Z = \sqrt{\sum_{i=1}^{\chi} \left(\lambda^{[l]}_{i,i}\right)^2} \quad .$$

Since Z is a measure for the deviation of the truncation from the norm 1 it gives us also an useful quantity to estimate the size of the error induced by the truncation, the truncated weight w:

$$w = 1 - Z \quad . \tag{3.35}$$

The normalization conditions 3.24 and 3.26 respectively 3.32 and 3.33 still hold, because the matrices were retained by an SVD with orthonormal vectors as their columns and the orthonormality conditions displays only the orthonormality of the surviving states.

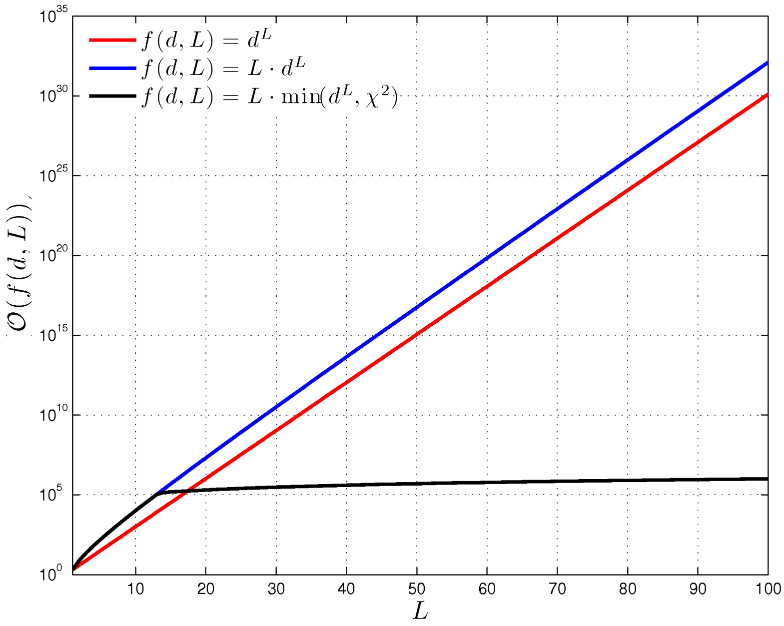

Figure 3.11: In this half-logarithmic plot one can see the amount of storage needed for one-dimensional system of size L and single site Hilbert dimension $d = 2$. The red line corresponds to the coefficients which have to be stored following equation 3.1. The blue line shows the storage amount for an exact MPS representation and the black line is the approximate representation with a truncated MPS with maximum matrix dimension χ of 100. As one can see, whereas the storage amount scales exponetially with system size L for the exact representations, it scales only linearly for the truncated MPS.

3.6.2 Area laws

Referring to the section above, one question arises: Is an MPS with a fixed matrix dimension χ capable of describing a quantum state?

Consider a bipartitioning of a system into two subsystems $A|B$, where the system AB is in the thermodynamic limit. The subsystem A is of the size L^D, where D is the spatial dimension. According to the area laws (see [5], [37]) the entanglement entropy for ground states of short range Hamiltonians with gap is proportional to the surface of the bipartition

$$S_N(A|B) \propto L^{D-1} \quad . \tag{3.36}$$

That means for one-dimensional systems the entanglement entropy is proportional to just a constant, whereas it scales directly proportional to L for two-dimensional systems (figure 3.12).
At criticality a more complex behavior appears, but for one-dimensional critical systems it is still only

$$S_N(A|B) \propto \log L \quad . \tag{3.37}$$

With the upper limit $\overline{S}_N$ of the entanglement entropy in equation 3.15 the connection of the entanglement entropy S_N and the Schmidt rank r follows

$$r \propto \exp(S_N) \quad . \tag{3.38}$$

That is why at for spatial dimensions larger than one the Schmidt rank has to grow exponentially with the system size. But the good news is that for one-dimensional non-critical systems a constant matrix dimension $r \approx \chi$ is capable of representing a quantum state in an efficient way.

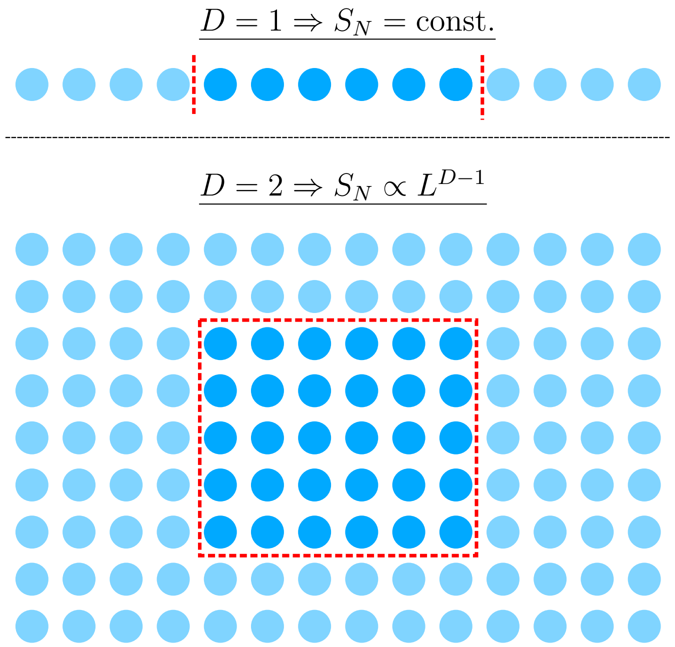

Figure 3.12: Graphical representation of the entropy scaling of a one- (top) and a two-dimensional (bottom) system for ground-states of non-critical local Hamiltonians. The entanglement entropy scales like L^{D-1}, where D is the spatial dimension.

3.7 Calculation of observables for MPS

Until now the whole chapter was just about a new representation of quantum states and certainly only transforming quantum states to other representations is a not satisfying activity and of no physical interest at all. That is why this section is about calculating overlaps, norms, expectation values and the effect of operators on MPS to put some physics in this by now just mathematical apparatus. So let us get straight down to the nitty-gritty.

3.7.1 Overlaps and Norms

For calculating the overlap of two MPS we first have to introduce an MPS representation independent of whether the single matrices are left- or right-normalized, called the *general* MPS. Starting point for this representation is the mixed-canonical MPS in equation 3.28:

$$|\psi\rangle = \sum_{\sigma_1,\dots,\sigma_L} A^{\sigma_1}\dots A^{\sigma_l}\lambda_{a_l,a_l}B^{\sigma_{l+1}}\dots B^{\sigma_L}|\sigma_1,\dots\sigma_L\rangle \tag{3.39}$$

Multiplying the matrix λ_{a_l,a_l} either on the matrix A^{σ_l} to the left or on the matrix $B^{\sigma_{l+1}}$ on the right leads to a representation called general MPS

$$|\psi\rangle = \sum_{\sigma_1,\dots,\sigma_L} M^{\sigma_1}\dots M^{\sigma_L}|\sigma_1,\dots,\sigma_L\rangle \quad , \tag{3.40}$$

with general matrices M^{σ_l} on each site without any implicit normalization conditions. Note, that we can always transform a general MPS to a left-canonical one:

$$\begin{aligned}
|\psi\rangle &= \sum_{\sigma_1,\dots,\sigma_L}\sum_{a_1,\dots,a_L} M^{\sigma_1}_{1,a_1}M^{\sigma_2}_{a_1,a_2}M^{\sigma_3}_{a_2,a_3}\dots|\sigma_1,\dots,\sigma_L\rangle \\
&= \sum_{\sigma_1,\dots,\sigma_L}\sum_{a_1,\dots,a_L} M_{(1,\sigma_1),a_1}M^{\sigma_2}_{a_1,a_2}M^{\sigma_3}_{a_2,a_3}\dots|\sigma_1,\dots,\sigma_L\rangle \\
&\overset{\text{SVD}}{=} \sum_{\sigma_1,\dots,\sigma_L}\sum_{a_1,\dots,a_L}\sum_{\gamma_1} A_{(1,\sigma_1),\gamma_1}\lambda_{\gamma_1,\gamma_1}V^\dagger_{\gamma_1,a_1}M^{\sigma_2}_{a_1,a_2}M^{\sigma_3}_{a_2,a_3}\dots|\sigma_1,\dots,\sigma_L\rangle \\
&= \sum_{\sigma_1,\dots,\sigma_L}\sum_{a_2,\dots,a_L}\sum_{\gamma_1} A_{(1,\sigma_1),\gamma_1}\underbrace{\left(\sum_{a_1}\lambda_{\gamma_1,\gamma_1}V^\dagger_{\gamma_1,a_1}M^{\sigma_2}_{a_1,a_2}\right)}_{\tilde{M}^{\sigma_2}_{a_1,a_2}}M^{\sigma_3}_{a_2,a_3}\dots|\sigma_1,\dots,\sigma_L\rangle \\
&= \sum_{\sigma_1,\dots,\sigma_L}\sum_{a_2,\dots,a_L}\sum_{\gamma_1} A^{\sigma_1}_{a_1}\tilde{M}^{\sigma_2}_{\gamma_1,a_2}M^{\sigma_3}_{a_2,a_3}\dots|\sigma_1,\dots,\sigma_L\rangle \\
&= \dots = \sum_{\sigma_1,\dots,\sigma_L}\sum_{\gamma_1,\dots,\gamma_{L-1}} A^{\sigma_1}_{a_1}\dots A^{\sigma_L}_{a_{L-1}}|\sigma_1,\dots,\sigma_L\rangle \quad .
\end{aligned}$$

The same procedure starting from the right could also be applied to construct a right-canonical MPS out of a general one.
The calculation of the overlap of two general MPS $|\phi\rangle$ and $|\psi\rangle$ can be obtained by simply taking the adjunct of one MPS, e.g. $\langle\phi|$, and calculate the scalar product:

$$\langle\phi|\psi\rangle = \sum_{\sigma_1,\dots,\sigma_L}(\tilde{M}^{\sigma_L\dagger}\dots\tilde{M}^{\sigma_1\dagger})\,(M^{\sigma_1}\dots M^{\sigma_L}) \quad . \tag{3.41}$$

Efficient evaluation of the contraction of equation 3.41 can be achieved by rearranging the L sums over the physical indices σ_i

$$\langle\phi|\psi\rangle = \sum_{\sigma_L}\tilde{M}^{\sigma_L\dagger}\left(\dots\left(\sum_{\sigma_2}\tilde{M}^{\sigma_2\dagger}\left(\sum_{\sigma_1}\tilde{M}^{\sigma_1\dagger}M^{\sigma_1}\right)M^{\sigma_2}\right)\dots\right)M^{\sigma_L} \quad , \tag{3.42}$$

so that the columns and the row vectors of $\tilde{M}^{\sigma_1\dagger}$ and M^{σ_1} are multiplied and then followed by the summation over the first physical index σ_1 and so forth. This reduces the necessary operation count from exponentially to weak polynomial. A graphical representation of this procedure can be found in figure 3.13.

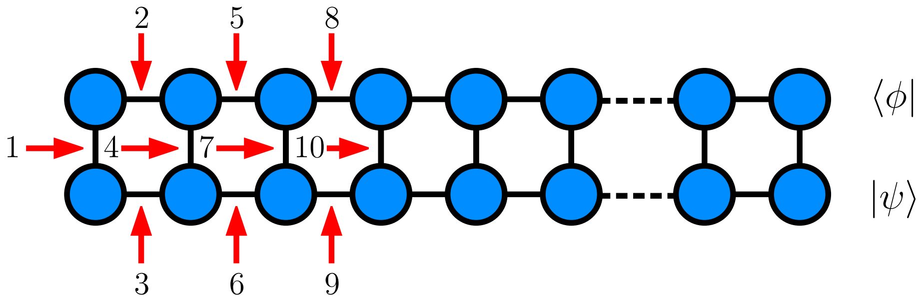

Figure 3.13: Overlap between two MPS states $|\psi\rangle$ and $|\phi\rangle$. The red arrows with the indices represent the most efficient way for the contraction of the MPS.

The norm is obtained by calculating the overlap of an MPS with itself ($\langle\psi|\psi\rangle$). Obviously the calculation of the norm of a left- or right-canonical MPS results in 1, because of the normalization condition 3.24 respectively 3.26 of the single matrices:

$$\langle\psi|\psi\rangle = \sum_{\sigma_L} A^{\sigma_L\dagger}\left(\dots\left(\sum_{\sigma_2} A^{\sigma_2\dagger}\underbrace{\left(\sum_{\sigma_1} A^{\sigma_1\dagger}A^{\sigma_1}\right)}_{\mathbb{1}}A^{\sigma_2}\right)\dots\right)A^{\sigma_L} \tag{3.43}$$

$$= \sum_{\sigma_L} A^{\sigma_L\dagger}\left(\dots\underbrace{\left(\sum_{\sigma_2} A^{\sigma_2\dagger}A^{\sigma_2}\right)}_{\mathbb{1}}\dots\right)A^{\sigma_L} = \dots = \underbrace{\sum_{\sigma_L} A^{\sigma_L\dagger}A^{\sigma_L}}_{\mathbb{1}} = 1 \quad . \tag{3.44}$$

Finally one interesting circumstance should be outlined here. If we consider a mixed-canonical MPS and sequentially calculate the norm in the above mentioned manner, we straightforward get the normalization condition for the Schmidt eigenvalues in equation 3.7

$$\langle\psi|\psi\rangle = \sum_{\sigma_1,\dots,\sigma_L}\left(B^{\sigma_L\dagger}\dots B^{\sigma_{l+1}\dagger}\lambda^{[l]}A^{\sigma_l\dagger}\dots A^{\sigma_1\dagger}\right)\left(A^{\sigma_1}\dots A^{\sigma_l}\lambda^{[l]}B^{\sigma_{l+1}}\dots B^{\sigma_L}\right) \tag{3.45}$$

$$\Rightarrow \langle\psi|\psi\rangle = \sum_{a_l}\lambda^2_{a_l,a_l} \quad . \tag{3.46}$$

Reduced density operator

As we saw for the entanglement entropy S_N in equation 3.14, it is connected to the reduced density matrix. To calculate ρ in the context of MPS, we first have to calculate the projector $|\psi\rangle\langle\psi|$, apply a bipartitioning by a virtual cut on site l and then trace out one of the two subsystem resulting from this cut.
The projection in MPS language of, for example, a left-normalized MPS is given by

$$|\psi\rangle\langle\psi| = \sum_{\sigma_1,\dots,\sigma_L}\sum_{\sigma'_1,\dots,\sigma'_L}\left(A^{\sigma_1}\dots A^{\sigma_L}\right)\left(A^{\sigma'_L\dagger}\dots A^{\sigma'_1\dagger}\right)|\sigma_1,\dots,\sigma_L\rangle\langle\sigma'_1,\dots,\sigma'_L| \quad . \tag{3.47}$$

Bipartition of system $A|B$ at site l, where A is the subsystem containing sites $i = 1$ to $i = l$ and B is the contrary subsystem, and tracing out the degrees of freedom for subsystem B results in

$$\hat{\rho}_A^{[l]} = \mathrm{Tr}_B\,|\psi\rangle\langle\psi| = \sum_{\sigma_1,\dots,\sigma_l}\sum_{\sigma'_1,\dots,\sigma'_l}\Big(A^{\sigma_1}\dots A^{\sigma_L}\Big)\rho_A^{[l]}\Big(A^{\sigma'_L\dagger}\dots A^{\sigma'_1\dagger}\Big)|\sigma_1,\dots,\sigma_L\rangle\langle\sigma'_1,\dots,\sigma'_L| \quad , \tag{3.48}$$

with

$$\rho_A^{[l]} = \sum_{\sigma_{l+1},\dots,\sigma_L}\Big(A^{\sigma_{l+1}}\dots A^{\sigma_L}\Big)\Big(A^{\sigma_L\dagger}\dots A^{\sigma_{l+1}\dagger}\Big) \quad . \tag{3.49}$$

Iteratively applying this procedure on every site from right to left leads to the recursion relation

$$\rho_A^{[l-1]} = \sum_{\sigma_l} A^{\sigma_l}\rho_A^{[l]}A^{\sigma_l\dagger} \quad . \tag{3.50}$$

The same can be done for right-canonical MPS starting from the left

$$\rho_B^{[l]} = \sum_{\sigma_l} B^{\sigma_l\dagger}\rho_B^{[l-1]}B^{\sigma_l} \quad . \tag{3.51}$$

Calculating the reduced density operator for mixed-canonical MPS

$$|\psi\rangle = \sum_{\sigma_1,\dots,\sigma_L} A^{\sigma_1}\dots A^{\sigma_l}\Psi B^{\sigma_{l+1}}\dots B^{\sigma_L}|\sigma_1,\dots,\sigma_L\rangle \tag{3.52}$$

results in

$$\rho_A^{[l]} = \Psi\Psi^\dagger \quad \text{resp.} \quad \rho_B^{[l]} = \Psi^\dagger\Psi \quad , \tag{3.53}$$

as can be seen in [9].

3.7.2 Expectation values

Now that we know how to calculate the norm of an MPS, we can go one step further and try to calculate the expectation value of one- and two-site operators applied to MPS.

One-site operator

One site operators in quantum mechanics are of the form

$$\hat{O}^{[l]} = \sum_{\sigma_l,\sigma'_l} O^{\sigma_l,\sigma'_l}|\sigma_l\rangle\langle\sigma'_l| \quad , \tag{3.54}$$

where O^{σ_l,σ'_l} are the matrix elements $\langle\sigma_l|\hat{O}^{[l]}|\sigma'_l\rangle$. If we extend the operator on every site[4] and are looking at the operator matrix elements $O^{\sigma_1\sigma'_1}O^{\sigma_2\sigma'_2}\dots O^{\sigma_L\sigma'_L}$, we realize that the main difference to the overlaps of two MPS is, that we have now to deal with double sums over local states.

---

[4] In practice an operator will not be applied on every site. This could be circumvented by applying the identity operator $\mathbb{1}$ on sites, where no operator should have an effect (e.g. local expectation values, two-site correlators).

Calculating the general matrix elements $\langle\phi|\hat{O}^{[1]}\hat{O}^{[2]}\dots\hat{O}^{[L]}|\phi\rangle$ leads to

$$\begin{aligned}\langle\phi|\hat{O}^{[1]}\hat{O}^{[2]}\dots\hat{O}^{[L]}|\phi\rangle &= \\ &= \sum_{\sigma_1,\dots,\sigma_L}\sum_{\sigma'_1,\dots,\sigma'_L}\left(\tilde{M}^{\sigma_L\dagger}\dots\tilde{M}^{\sigma_1\dagger}\right)\left(O^{\sigma_1\sigma'_1}O^{\sigma_2\sigma'_2}\dots O^{\sigma_L\sigma'_L}\right)\left(M^{\sigma'_1}\dots M^{\sigma'_L}\right) \\ &= \sum_{\sigma_L,\sigma'_L}O^{\sigma_L\sigma'_L}\tilde{M}^{\sigma_L\dagger}\left(\dots\left(\sum_{\sigma_2,\sigma'_2}O^{\sigma_2\sigma'_2}\tilde{M}^{\sigma_2\dagger}\left(\sum_{\sigma_1,\sigma'_1}O^{\sigma_1\sigma'_1}\tilde{M}^{\sigma_1\dagger}M^{\sigma'_1}\right)M^{\sigma'_2}\right)\dots\right)M^{\sigma'_L} \quad .\end{aligned} \tag{3.55}$$

The rearranging in the third line of the above equation makes the calculation again more efficient.

If we have to deal with expectation values of operators $\hat{O}^{[l]}$ operating just on one single site l the expectation value $\langle\psi|\hat{O}^{[l]}|\psi\rangle$ simplifies drastically. Imagine all matrices to the left are left-normalized, all to the right are right-normalized[5]. The normalization condition of site l does not play any role for the calculation. Now contracting the tensor network due to left- and right-normalization leads to an equation, where just two-matrices, the matrices on site l are left-over. This site can be simply calculated by

$$\langle\psi|\hat{O}^{[l]}|\psi\rangle = \sum_{\sigma_l,\sigma'_l}O^{\sigma_l,\sigma'_l}\,\mathrm{Tr}\left(\tilde{M}^{\sigma_l\dagger}M^{\sigma_l}\right) \quad . \tag{3.56}$$

The graphical representation of this procedure is found in figure 3.14.

To get the above formulas in canonical-normal form, one only has to insert

$$M^{\sigma_l}_{a_{l-1},a_l} := \lambda^{[l-1]}\Gamma^{\sigma_l}_{a_{l-1},a_l}\lambda^{[l]} \quad . \tag{3.57}$$

Lets have again a look in a different point of view at applying an operator $\hat{O}^{[l]}$ to an MPS. The operator changes the value at the physical index σ_l of the MPS. So applying it on a canonical MPS $|\psi\rangle$ leads to a new MPS $|\psi'\rangle$, which is only canonical, if the operator is also unitary:

$$\begin{aligned}&\sum_{\sigma_l}A^{\sigma\sigma_l}A^{\sigma\sigma_l\dagger} = \mathbb{1} \\ &\Rightarrow \sum_{\sigma_l,\sigma'_l,\sigma''_l}\left(O^{\sigma_l,\sigma'_l}A^{\sigma'_l}\right)\left(O^{\sigma_l,\sigma''_l}A^{\sigma''_l}\right)^\dagger \\ &\quad = \sum_{\sigma_l,\sigma'_l,\sigma''_l}A^{\sigma'_l}A^{\sigma''_l\dagger}\langle\sigma_l|O|\sigma'_l\rangle\langle\sigma''_l|O^\dagger|\sigma_l\rangle \\ &\quad = \sum_{\sigma'_l,\sigma''_l}A^{\sigma'_l}A^{\sigma''_l\dagger}\langle\sigma''_l|O^\dagger O|\sigma'_l\rangle \overset{!}{=} \mathbb{1} \quad .\end{aligned}$$

So we see, that the operator has to be right unitary to accomplish the left-normalization condition. For the right-normalization condition we get:

$$\sum_{\sigma_l}B^{\sigma\sigma_l\dagger}B^{\sigma\sigma_l} = \mathbb{1} \Rightarrow \sum_{\sigma'_l,\sigma''_l}B^{\sigma''^\dagger_l}B^{\sigma'_l}\langle\sigma''_l|OO^\dagger|\sigma'_l\rangle \overset{!}{=} \mathbb{1} \quad .$$

---

[5] This can be easily achieved. Remember section 3.7.1, where we have pointed out that it is always possible to cast a general MPS into a left- or right normalized one.

The operator has to be left unitary, which means the operator has to be unitary to guarantee, that the new MPS $|\psi'\rangle$ is canonical again. $\square$

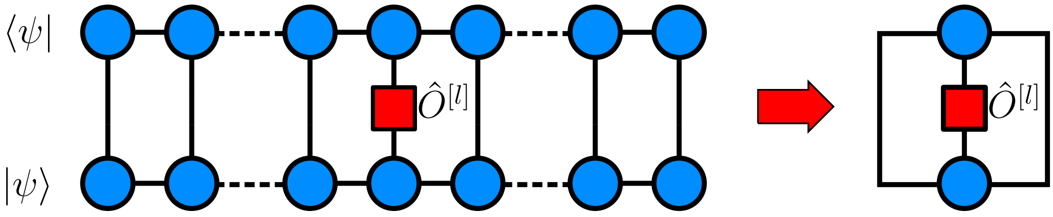

Figure 3.14: Calculating the expectation $\langle\psi|\hat{O}^{[l]}|\psi\rangle$ value of a single-site operator $\hat{O}^{[l]}$, one can easily see that sequentially applying the normalization condition for the A- and B-matrices results in a calculation of the form represented on the right side of this figure.

Two-site operator

For the present thesis, we will only need unitary two-site operators (for time evolution), thus we restrict the discussion to such operators. As we saw for one-site operators before, applying such an operator to a canonical MPS yields again a canonical MPS. A two-site operator looks like

$$\hat{O}^{[l,l+1]} = \sum_{\sigma_l,\sigma_{l+1},\sigma'_l,\sigma'_{l+1}} O^{\sigma'_l,\sigma'_{l+1}}_{\sigma_l\sigma_{l+1}} |\sigma_l,\sigma_{l+1}\rangle\langle\sigma'_l,\sigma'_{l+1}|$$

with $O^{\sigma'_l,\sigma'_{l+1}}_{\sigma_l\sigma_{l+1}}$ matrix elements $\langle\sigma_l,\sigma_{l+1}|\hat{O}^{[l,l+1]}|\sigma'_l,\sigma'_{l+1}\rangle$. Because two-site operators act on two neighboring sites, at first we have to find out which matrices in an MPS this sort of operator changes. Therefore we consider an MPS in canonical normal form and bracket out the part where the two-site operator acts:

$$|\psi\rangle = \sum_{\sigma_1,\ldots,\sigma_L} \left(\Gamma^{\sigma_1}\lambda^{[1]}\ldots\Gamma^{\sigma_{l-1}}\right)\left(\lambda^{[l-1]}\Gamma^{\sigma_l}\lambda^{[l]}\Gamma^{\sigma_{l+1}}\lambda^{[l+1]}\right)\left(\Gamma^{\sigma_{l+2}}\lambda^{[l+2]}\ldots\lambda^{[L-1]}\Gamma^{\sigma_L}\right)|\sigma_1\ldots\sigma_L\rangle \quad . \tag{3.58}$$

If one also brings out the matrix multiplication over the virtual index a_l, one can identify the sphere of action of the operator

$$\Psi^{\sigma_l,\sigma_{l+1}}_{a_{l-1},a_{l+1}} := \sum_{a_l} \lambda^{[l-1]}\Gamma^{\sigma_l}_{a_{l-1},a_l}\lambda^{[l]}\Gamma^{\sigma_{l+1}}_{a_l,a_{l+1}}\lambda^{[l+1]} \quad . \tag{3.59}$$

Renaming the untouched part on the left

$$|\Phi^{[1,\ldots,l-1]}_{a_{l-1}}\rangle = \sum_{\sigma_1,\ldots,\sigma_{l-1}} \left(\Gamma^{\sigma_1}\lambda^{[1]}\ldots\lambda^{[l-2]}\Gamma^{\sigma_{l-1}}\right)_{a_{l-1}} |\sigma_1,\ldots,\sigma_{l-1}\rangle \tag{3.60}$$

and the untouched part to the right of the MPS

$$|\Phi^{[l+2,\ldots,L]}_{a_{l+2}}\rangle = \sum_{\sigma_{l+2},\ldots,\sigma_L} \left(\Gamma^{\sigma_{l+2}}\lambda^{[l+2]}\ldots\lambda^{[L-1]}\Gamma^{\sigma_L}\right)_{a_{l+1}} |\sigma_{l+2},\ldots,\sigma_L\rangle \tag{3.61}$$

one gets

$$|\psi\rangle = \sum_{\sigma_l,\sigma_{l+1}} \sum_{a_{l-1},a_{l+1}} \Psi^{\sigma_l,\sigma_{l+1}}_{a_{l-1},a_{l+1}} |\Phi^{[1,\dots,l-1]}_{a_{l-1}}\rangle \otimes |\sigma_l\rangle \otimes |\sigma_{l+1}\rangle \otimes |\Phi^{[l+2,\dots,L]}_{a_{l+2}}\rangle \quad .$$

Applying operator O concerns only the part around site l and $l+1$

$$|\psi'\rangle = \sum_{\sigma_l,\sigma_{l+1}} \sum_{a_{l-1},a_{l+1}} \Theta^{\sigma_l,\sigma_{l+1}}_{a_{l-1},a_{l+1}} |\Phi^{[1,\dots,l-1]}_{a_{l-1}}\rangle \otimes |\sigma_l\rangle \otimes |\sigma_{l+1}\rangle \otimes |\Phi^{[l+2,\dots,L]}_{a_{l+2}}\rangle \quad ,$$

where $\Theta^{\sigma_l,\sigma_{l+1}}_{a_{l-1},a_{l+1}}$ stands for

$$\Theta^{\sigma_l,\sigma_{l+1}}_{a_{l-1},a_{l+1}} := \sum_{a_l} O^{\sigma'_l,\sigma'_{l+1}}_{\sigma_l\sigma_{l+1}} \lambda^{[l-1]} \Gamma^{\sigma_l}_{a_{l-1},a_l} \lambda^{[l]} \Gamma^{\sigma_{l+1}}_{a_l,a_{l+1}} \lambda^{[l+1]} \quad .$$

To apply two site operator, all we have to do is to update the Γ- and λ-matrices in Θ to obtain new ones. To achieve this, there are two possibilities, either one makes an SVD of Θ, or one diagonalizes the reduced density operator ρ on the sites from $l+1$ to L.

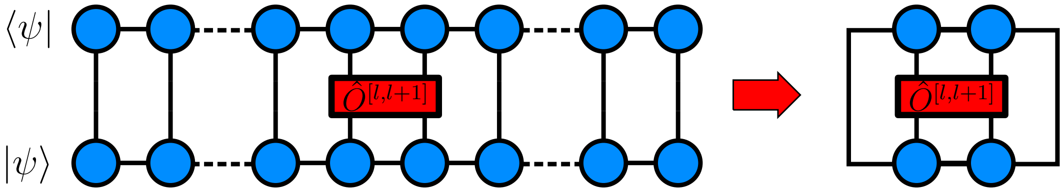

Figure 3.15: To calculate the expectation value $\langle\psi|\hat{O}^{[l,l+1]}|\psi\rangle$ of a two-site operator acting on site l and $l+1$, just sequantially apply the normalization condition for the A- and B-matrices, which will result in a calculation of the form represented on the right side. This operator then acts on the $\lambda^{[l-1]}$-, Γ^{σ_l}-,$\lambda^{[l]}$-, $\Gamma^{\sigma_{l+1}}$- and $\lambda^{[l+1]}$-matrices of an MPS in canonical normal form, where an updating procedure can be achieved by an SVD of the product of these few matrices or by diagonalizing the reduced density operator ρ.

a.) Diagonalization of ρ:

The first technique to update the Γ- and λ-matrices starts with the reduced density matrix of a many particle system consisting of two subsystems A and B

$$\rho^B = \mathrm{Tr}^A \left(|\psi'\rangle\langle\psi'|\right) \quad . \tag{3.62}$$

The plan is to compute ρ and after the diagonalization of the reduced density operator one obtains the eigenvalues, which are equal to the new Schmidt eigenvalues, and an unitary matrix U, which basically contains the new Γ-matrix for site $l+1$

$$\rho^B = \sum_{\substack{\sigma_{l+1}\sigma'_{l+1}\\ a_{l+1}a'_{l+1}}} \underbrace{\left(\sum_{\sigma_n a_{l-1}} \Theta^{\sigma_l,\sigma_{l+1}}_{a_{l-1},a_{l+1}} \left(\Theta^{\sigma_l,\sigma'_{l+1}}_{a_{l-1},a'_{l+1}}\right)^* \right)}_{M_{(\sigma_{l+1}a_{l+1}),(\sigma'_{l+1}a'_{l+1})}} |\sigma_{l+1},\Phi^{[l+2,\dots,L]}_{a_{l+2}}\rangle\langle\sigma_{l+1},\Phi^{[l+2,\dots,L]}_{a_{l+2}}| \quad . \tag{3.63}$$

Afterwards, diagonalization of M results in the new $\tilde{\lambda}^{[l]}$ values

$$M_{(\sigma_{l+1}a_{l+1}),(\sigma'_{l+1}a'_{l+1})} = \sum_{\gamma} U_{(\sigma_{l+1}a_{l+1}),a_l} D_{a_l,a_l} U^{\dagger}_{a_l,(\sigma_{l+1}{}',a'_{l+1})} \quad , \tag{3.64}$$

where the matrix D contains the absolute squares of the Schmidt eigenvalues $D_{a_l,a_l} = |\tilde{\lambda}^{[l]}_{a_l}|^2$ of site l. Plugging equation 3.64 into equation 3.63 leads to

$$\rho^B = \sum_{\substack{\sigma_{l+1}\sigma'_{l+1}\\ a_{l+1}a'_{l+1}}} \sum_{a_l} U_{(\sigma_{l+1}a_{l+1}),a_l} D_{a_l,a_l} U^{\dagger}_{a_l,(\sigma_{l+1}{}',a'_{l+1})} |\sigma_{l+1},\Phi^{[l+2,\dots,L]}_{a_{l+2}}\rangle\langle\sigma_{l+1},\Phi^{[l+2,\dots,L]}_{a_{l+2}}| \quad . \tag{3.65}$$

Comparing the equation above simply with the trace over subsystem B

$$\begin{aligned} &\mathrm{Tr}^A\left(|\psi'\rangle\langle\psi'|\right) = \\ &\sum_{a_l} |\tilde{\lambda}^{[l]}_{a_l}|^2 \sum_{\substack{\sigma_{l+1}\sigma'_{l+1}\\ a_{l+1}a'_{l+1}}} \tilde{\Gamma}^{\sigma_{l+1}}_{a_l,a_{l+1}} \lambda^{[l+1]}_{a_{l+1}} \left(\Gamma^{\sigma'_{l+1}}_{a_l,a'_{l+1}} \lambda^{[l+1]}_{a'_{l+1}}\right)^* |\sigma_{l+1},\Phi^{[l+2,\dots,L]}_{a_{l+2}}\rangle\langle\sigma_{l+1},\Phi^{[l+2,\dots,L]}_{a_{l+2}}| \end{aligned} \tag{3.66}$$

one can see that the new $\tilde{\Gamma}$ on site $l+1$ are equal to

$$\tilde{\Gamma}^{\sigma_{l+1}}_{a_l,a_{l+1}} = \frac{U_{(\sigma_{l+1}a_{l+1}),a_l}}{\lambda^{[l+1]}_{a_{l+1}}} \quad . \tag{3.67}$$

The new $\tilde{\Gamma}$-matrices on site l are then obtained from the scalar product resulting from $|\psi'\rangle = \lambda_{a_l}|\Phi^A_{a_l}\rangle|\Phi^B_{a_l}\rangle$:

$$\lambda_{a_l}|\Phi^A_{a_l}\rangle = \langle\Phi^B_{a_l}|\psi'\rangle \tag{3.68}$$

$$= \sum_{a_{l-1}\sigma_l} \left(\sum_{\sigma_{l+1}a_{l+1}} \Theta^{\sigma_l\sigma_{l+1}}_{a_{l-1},a_{l+1}} \left(\tilde{\Gamma}^{\sigma_{l+1}}_{a_l,a_{l+1}} \lambda^{[l+1]}_{a_{l+1}}\right)^* \right) |\Phi^A_{a_l}\rangle \otimes |\sigma_l\rangle \tag{3.69}$$

$$= \tilde{\lambda}^{[l]}_{a_l} \sum_{a_{l-1}\sigma_l} \lambda^{[l-1]}_{a_{l-1}} \tilde{\Gamma}^{\sigma_l}_{a_{l-1}a_l} |\Phi^A_{a_l}\rangle \otimes |\sigma_l\rangle \quad . \tag{3.70}$$

Finally one gets the missing matrix $\tilde{\Gamma}$ by transforming the equation above

$$\tilde{\Gamma}^{\sigma_l}_{a_{l-1}a_l} = \frac{1}{\tilde{\lambda}^{[l]}_{a_l}\lambda^{[l-1]}_{a_{l-1}}} \sum_{\sigma_{l+1}a_{l+1}} \left(\tilde{\Gamma}^{\sigma_{l+1}}_{a_l,a_{l+1}} \lambda^{[l+1]}_{a_{l+1}}\right)^* \Theta^{\sigma_l\sigma_{l+1}}_{a_{l-1},a_{l+1}} \quad . \tag{3.71}$$

b.) SVD of Θ:

The second method to obtain the new Γ and λ matrices is far easier and favorable due to the existence of fast SVD algorithms. One drawback of this method is that implementation of quantities which are conserved during the simulation like for example the total number of particles $N = \sum_l \hat{n}_l$ or the total spin $\vec{S} = \sum_i \vec{S}_i$, is more complicated than the update procedure with the reduced density operator.

The second method is based on an SVD of the whole Θ matrix. If one reshapes the matrix and performs an SVD, one gets directly the new Schmidt eigenvalues $\tilde{\lambda}$.

From the *left singular vectors* U and the *right singular vectors* $V^\dagger$ the desired new $\tilde{\Gamma}$-matrices can easily be calculated by help of the Schmidt eigenvalues on the left $\lambda^{[l-1]}$ and on the right $\lambda^{[l+1]}$

$$\Theta_{(\sigma_l a_{l-1}),(\sigma_{l+1} a_{l+1})} \overset{\text{SVD}}{=} \sum_{a_l} U_{(\sigma_l a_{l-1}),a_l} \tilde{\lambda}^{[l]}_{a_l,a_l} V^\dagger_{a_l,(\sigma_{l+1} a_{l+1})} \tag{3.72}$$

$$\tilde{\Gamma}^{\sigma_l}_{a_{l-1}a_l} = \frac{U_{(\sigma_l a_{l-1}),a_l}}{\lambda^{[l-1]}_{a_l,a_l}} \tag{3.73}$$

$$\tilde{\Gamma}^{\sigma_{l+1}}_{a_l a_{l+1}} = \frac{V^\dagger_{a_l,(\sigma_{l+1} a_{l+1})}}{\lambda^{[l+1]}_{a_l,a_l}} \quad . \tag{3.74}$$

The division has to be performed as a so-called pseudoinverse. Elements of λ_{a_l,a_l} beneath a certain small value ϵ (e.g. $\epsilon = 10^{-8}$) are set to zero. This means, that one neglects those directions in the space of the indices a_l, which contribute only a little to ψ, because of there small values. The necessity of this pseudoinverse is a disadvantage of this variant.

A graphical representation of this procedure is outlined in figure 3.16.

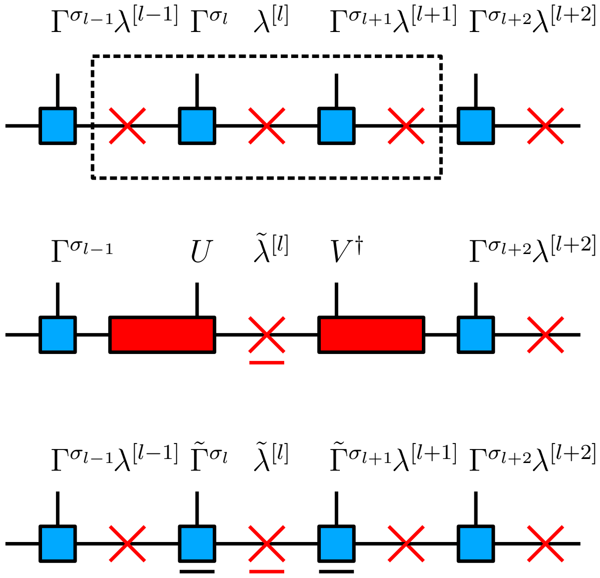

Figure 3.16: Graphical representation of the update procedure after application of a two-site operator to obtain the new $\tilde{\Gamma}$- and $\tilde{\lambda}$-matrices of an MPS in canonical normal form by performing an SVD of the Θ matrix. In the first row the Θ-matrix is depicted by the dashed square consisting of the matrices $\lambda^{[l-1]}, \Gamma^{\sigma_l}, \lambda^{[l]}, \Gamma^{\sigma_{l+1}}, \lambda^{[l+1]}$, on which the operator acts. The second row represents the MPS after an SVD, where one gets the new matrix $\tilde{\lambda}^{[l]}$ containing the new Schmidt eigenvalues on site l and the *left-* and *right- singular vectors* U and $V^\dagger$. Division of U and $V^\dagger$ by $\lambda^{[l-1]}$ and $\lambda^{[l+1]}$ leads to the new $\tilde{\Gamma}$-matrices. All new obtained matrices are represented in this figure with an extra line underneath.

3.8 Density Matrix Renormalization Group

In physics, Renormalization Group methods (RG) are an mathematical instrument for describing dependencies of physical observables on length scales. They first appeared in 1953 in the work of E. C. G. Stueckelberg, Andre Petermann, Francis Low and Murray Gell-Mann in the treatment of quantum electrodynamically problems. Originally an instrument for solving problems in quantum field theory, nowadays they have various fields of application like solid state physics, continuum mechanics or cosmology.

In 1975 K.G. Wilson, a former PhD student of Gell-Mann, solved the Kondo problem with a numerical renormalization group method, today known as Wilson's Numerical Renormalization Group (NRG) [8]. Since then, NRG has been very successful in solving many-body problems, in which impurities play a leading part like the Kondo or the Anderson impurity model. In appreciation of his work Wilson was awarded in 1982 with the Nobel Prize in Physics, like his PhD supervisor twelve years before.

In 1992, Steven R. White invented today's most efficient method to find ground and low energy states in one-dimensional strongly correlated quantum systems, the Density Matrix Renormalization Group (DMRG) [3]. It is a variational method that minimizes the energy expectation value

$$E = \frac{\langle\psi|\hat{H}|\psi\rangle}{\langle\psi|\psi\rangle}$$

and has many applications, where the accuracy of the results can be as large as, e.g., 10 decimal digits.

The key aspect of DMRG is the truncation of the total Hilbert space of a system to a reduced Hilbert space, but with the property that the approximated state has a very large overlap with the original not truncated state, as we will see later.

One major advantage is that DMRG does not know the fermionic sign problem and can therefore be applied to bosonic or fermionic systems equally.

DMRG prefers open boundary conditions (OBC) as we premised in the Hamiltonians in the chapter before. With periodic boundary conditions, the necessary computational effort is considerably larger [38].

DMRG can be formulated in MPS terms, as Östlund and Rommer discovered first (see [39]).

In the following sections we will first start with the infinite size DMRG (iDMRG), because it is conceptually easier to understand than the finite case and it bears all the important aspects of the algorithm. Then we will handle the finite case.

For the DMRG algorithms we assume Hamiltonians of the form:

$$\hat{H} = \sum_i \hat{h}_i \hat{h}_{i+1} \quad ,$$

where i denotes the index of the lattice site. It is obvious that this is the case for the Heisenberg Hamiltonian $\hat{H}_{HEI}$ in equation 2.3, the spinless fermion Hamiltonian $\hat{H}_{SF}$ in 2.57 , the Hamiltonian of the Hubbard model $\hat{H}_{HUB}$ (equation 2.59) and the s-wave and p-wave Hamiltonians of the BCS superconductor $\hat{H}_{BCS}$ (equations 2.88 and 2.89).

As before mentioned, DMRG is an iterative process, which enables a system to converge to its ground state.

Both, finite and infinite DMRG, share the same structure at each iteration step. The wave function consists of a block on the left A, called the system block consisting of n states $|\Phi_A\rangle$, followed by two blocks in the middle consisting of one site $|\sigma_i\rangle$ and $|\sigma_{i+1}\rangle$ with Hilbert space dimension d and one block on the right with m states $|\Phi_B\rangle$, called the environmental block B.

The principle of DMRG is that the system block A and/or the environment block B grow(s) by adding the sites in the middle. Then the groundstate of the extended system is calculated.

Due to the enlarging of one or both blocks by the adding of sites, the Hilbert space of the whole system has to grow exponentially. Therefore the keystone of the DMRG algorithm is not only the growing procedure, but also a truncation step, which keeps the relevant part of the whole Hilbert space to approximate the enlarged basis by the most relevant states.

3.8.1 Infinite size DMRG

In the infinite size DMRG (iDMRG) both, the system block A and the environment block B grow by adding one of the middle sites to each.

The iDMRG algorithm looks as follows:

1. The iteration starts with a state on the system block A consisting of l (Initially just one site) sites with basis states $|\Phi_A\rangle$. These basis states are usually expressed as an MPS, with dimension χ far below d^l.

2. Construct a similar block B called the environmental block by simply mirroring the system block A with basis states $|\Phi_B\rangle$.

3. Insert two sites between the system and the environment block $|\sigma_{l+1}\rangle$ and $|\sigma_{l+2}\rangle$.

4. Enlarge block $A = |\Phi_A\rangle$ by adding the first single site σ_{l+1} to form a block $A' = A\bullet = |\Phi_{A'}\rangle$ of size $l' = l+1$ by growing the Hilbert space dimension from $M = d^l$ to $M' = d \cdot M$. Further calculate the Hamiltonian $\hat{H}_\mathrm{A}$ of block A and the Hamiltonian $\hat{h}_{l,l+1}$ of the single site $|\sigma_{l+1}\rangle$ consisting of the operators $\hat{h}_l$ on the surface of block A and the operators $\hat{h}_{l+1}$ of the single site to get the Hamiltonian $\hat{H}_{A'} = \hat{H}_\mathrm{A} + \hat{h}_{l,l+1}$ of the enlarged block . Do the same for the environment block B and the second single site $|\sigma_{l+2}\rangle$ to get $B' = \bullet B$ and $\hat{H}_{B'} = \hat{h}_{l+2,l+3} + \hat{H}_\mathrm{B}$.

5. Form the so called superblock S by connecting block A and B with the two single sites in between $S = A \bullet \bullet B$ with overall $2l+2$ sites. Construct also the superblock Hamiltonian $\hat{H}_\mathrm{S} = \hat{H}_{A'} + \hat{h}_{A',B'} + \hat{H}_{B'}$ by connecting blocks A' and B'.

6. Use for example the Lanczos algorithm to calculate the groundstate of the superblock S

$$|\Psi\rangle = \sum_{i,j} c_{i,j} |\Phi_{A'}\rangle |\Phi_{B'}\rangle$$

7. Then calculate the reduced density operator $\rho^{A'} = \mathrm{Tr}_{B'} |\Psi\rangle\langle\Psi|$ respectively $\rho^{B'} = \mathrm{Tr}_{A'} |\Psi\rangle\langle\Psi|$ and diagonalize it. Keep the eigenvectors $|\alpha\rangle$ belonging to the χ largest eigenvalues λ_α. These vectors are the new basis vectors.
8. Transform all Hamiltonians and basis states $|\Phi_{A'}\rangle$ and $|\Phi_{B'}\rangle$ in the new basis and start the iteration all over again from step 3 with $A = A'$ and $B = B'$ until the system has the desired length L.

Adaptation of the infinite size DMRG to finite system sizes is the topic of the next chapter. The procedure with different blocks growing by adding single sites stays the same, but the growing procedure is slightly different. A graphical representation of the iDMRG algorithm can be found in figure 3.17 on the left.

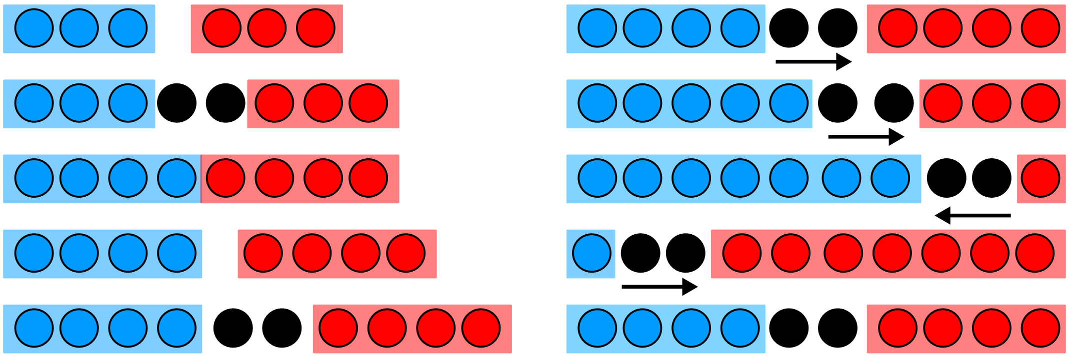

Figure 3.17: Graphical representation of the iDMRG algorithm (left) and finite-size DMRG algorithm (right). Both algorithm share the same block structure, with the system block A on the left site (blue square), two single sites in the middle (black circles) and the environmental block B on the right (red square). Only the block growth procedure is different for the two algorithms. Whereas for the iDMRG the system block A and the environmental block B are of the same size and growing at each iteration step resulting in a growing of both blocks and the total system size, in the finite-size DMRG either the system or the environmental block grows at the expense of the other, depending on wether the sweep of the current iteration goes from left to right (first two rows on the right) or from right to left (third line on the right). The algorithm is terminated in the middle, resulting in block A and block B of the same size, once the calculation is converged in energy.

3.8.2 Finite size DMRG

Starting point for the finite size DMRG is a system of size L obtained by the iDRMG algorithm. In this algorithm there is also a grow procedure, but now one block, e.g. system block A, grows on the expenses of environmental block B, which has to shrink as opposed to this, to keep the system size L constant. After one reaches the end of the system, the environmental block consist only of one site. Then one has to reverse the procedure, so that block B grows at the cost of block A until in turn block A is of size 1. Then reverse the growing direction again. This procedure is stopped at the starting point, after the energy has converged.

Here is the scheme of the finite size DMRG algorithm:

1. First perform the iDMRG algorithm to obtain a system of size L and then store the Hamiltonians and the operators for each block.
2. Cut the system in the middle and remove a single site at the contact area of every resulting block to obtain blocks in the form $A{\bullet}{\bullet}B$ similar to the iDMRG algorithm.
3. Like in iDMRG, compute and diagonalize the superblock Hamiltonian.
4. Calculate the reduced density matrix of $A\bullet$ and diagonalize it. Keep the eigenvectors $|\alpha\rangle$ belonging to the χ largest eigenvalues λ_α. These vectors are the new basis vectors. Project all operators to this basis and store them and the block $A\bullet$.
5. Shrink block B by taking out the site on the contact area with the single site remaining in the middle.
6. Repeat steps 3 to 5 until block B is of size 1.
7. Reverse the growing direction, so that block B grows on cost of block A in the same manner, but just in the other direction as in steps 3 to 5. Repeat until you reach the state, where block A is of size 1.
8. Reverse the growing direction again and start again from step 3. End the procedure after the energy has converged.

Graphically, the finite-size DMRG is shown in figure 3.17 on the right side.

3.9 Time Evolving Block Decimation

3.9.1 Time evolution of quantum systems

In quantum mechanics, the starting point for the time evolution of states is usually the time dependent Schrödinger equation:

$$i\frac{\partial}{\partial t}|\psi(t)\rangle = \hat{H}|\psi(t)\rangle \quad , \tag{3.75}$$

where $|\psi(t)\rangle$ is a time dependent state of the system and $\hat{H}$ is the normally time dependent system Hamiltonian.
The time evolution operator $\hat{U}$ is unitary and describes the evolution of a system from time t_0 to time t:

$$i\frac{\partial}{\partial t}\hat{U}(t,t_0) = \hat{H}\hat{U}(t,t_0) \tag{3.76}$$

$$|\psi(t)\rangle = \hat{U}(t,t_0)|\psi(t_0)\rangle \quad . \tag{3.77}$$

For the time operator following composition property is satisfied for the evolution of a system from the initial time t_0 to an intermediate time t_1 and subsequently to a final time t_2

$$\hat{U}(t_2,t_0) = \hat{U}(t_2,t_1)\hat{U}(t_1,t_0) \quad \text{with} \quad t_2 > t_1 > t_0 \quad . \tag{3.78}$$

In the most general form the time evolution operator $\hat{U}$ looks like

$$\hat{U}(t,t_0) = \hat{\mathcal{T}}\left[e^{-i\int_{t_0}^{t}\hat{H}(\tau)d\tau}\right] \quad , \tag{3.79}$$

where $\hat{\mathcal{T}}$ is the time ordering operator. This operator, as the name says, just orders quantum mechanical operators by their occurrence in time from the very right to the left:

$$\hat{\mathcal{T}}\left[\hat{A}(t_1)\hat{B}(t_2)\right] = \theta(t_1-t_2)\hat{A}(t_1)\hat{B}(t_2) + \theta(t_2-t_1)\hat{B}(t_2)\hat{A}(t_1) \quad . \tag{3.80}$$

$\theta(x)$ is the step function. If the Hamiltonian of the system commutes for different times, one can neglect the time ordering operator $\hat{\mathcal{T}}$

$$\left[\hat{H}(t_1),\hat{H}(t_2)\right] = 0 \quad \Rightarrow \quad \hat{U}(t,t_0) = e^{-i\int_{t_0}^{t}\hat{H}(\tau)d\tau} \quad . \tag{3.81}$$

If the Hamiltonian is not explicitly time dependent ($\hat{H}(t) = \hat{H} \;\; \forall t$) one can integrate the exponent in a trivial way and is only left with

$$\hat{U}(t,t_0) = e^{-i\hat{H}(t-t_0)} \quad . \tag{3.82}$$

Without loss of generality we can set the starting time t_0 to 0 and omit this variable subsequently. Of course it is possible to split the time evolution in N smaller equally spaced time steps τ with $N = t/\tau$

$$\hat{U}(t) = \underbrace{\hat{U}(\tau)\hat{U}(\tau)\ldots\hat{U}(\tau)\hat{U}(\tau)}_{N \text{ times}} = \hat{U}(\tau)^N = \left(e^{-i\hat{H}\tau}\right)^N \quad . \tag{3.83}$$

3.9.2 Suzuki-Trotter decomposition

All Hamiltonians we are going to investigate have only nearest neighbor interaction and are therefore of the form

$$\hat{H} = \sum_i \hat{h}_{i,i+1} \quad . \tag{3.84}$$

It should be noted that these Hamiltonians will in general not commute. So if we think of equation 3.83, it could be very handy, if we can transform the sum in the exponent into a product of exponentials, but because of the non-commuting Hamiltonian, this is not possible.

Instead, we can rearrange the Hamiltonian in even and odd Hamiltonians with respect to the bonds between the sites

$$\hat{H} = \hat{H}_{\text{odd}} + \hat{H}_{\text{even}} \tag{3.85}$$

$$\hat{H}_{\text{odd}} = \sum_i \hat{h}_{2i-1,2i} = \sum_i \hat{h}_i^o \tag{3.86}$$

$$\hat{H}_{\text{even}} = \sum_i \hat{h}_{2i,2i+1} = \sum_i \hat{h}_i^e \quad . \tag{3.87}$$

These single even or odd Hamiltonians commute with themselves but unfortunately they will not commute if even and odd Hamiltonians are mixed together like in the general Hamiltonian in equation 3.84:

$$\left[\hat{h}_i^o, \hat{h}_j^o\right] = \left[\hat{h}_i^e, \hat{h}_j^e\right] = 0 \tag{3.88}$$

$$\left[\hat{h}_i^o, \hat{h}_j^e\right] \neq 0 \quad . \tag{3.89}$$

The time evolution operator for even and odd Hamiltonians is of the form:

$$\hat{U}(t) = e^{i\hat{H}t} = e^{-i\left(\hat{H}_{\mathrm{odd}}+\hat{H}_{\mathrm{even}}\right)t} = \left[e^{-i\left(\hat{H}_{\mathrm{odd}}+\hat{H}_{\mathrm{even}}\right)\tau}\right]^N \quad . \tag{3.90}$$

Although this can not be decomposed in an exact way, it can be approximated by the so called Suzuki-Trotter decomposition (STD). The STD of first order for usually non-commuting operators $\hat{A}$ and $\hat{B}$ is

$$e^{-i\left(\hat{A}+\hat{B}\right)\tau} = e^{-i\hat{A}\tau}e^{-i\hat{B}\tau} + \mathcal{O}(\tau^2) \quad . \tag{3.91}$$

After applying the STD to term on the left side in the square brackets of equation 3.90 one gets:

$$e^{-i\left(\hat{H}_{\mathrm{odd}}+\hat{H}_{\mathrm{even}}\right)\tau} = e^{-i\hat{H}_{\mathrm{odd}}\tau}e^{-i\hat{H}_{\mathrm{even}}\tau} + \mathcal{O}(\tau^2) \tag{3.92}$$

$$= e^{-i\sum_i \hat{h}_i^o\tau}e^{-i\sum_i \hat{h}_i^e\tau} + \mathcal{O}(\tau^2) \tag{3.93}$$

$$= \prod_i e^{-i\hat{h}_i^o\tau}\prod_i e^{-i\hat{h}_i^e\tau} + \mathcal{O}(\tau^2) \tag{3.94}$$

As we see, the right equation consists only of a product of two site operators.
Unfortunately, every timestep adds an error of $\mathcal{O}(\tau^2)$, called the Trotter error. However this error can be regulated by the size of the equally spaced timesteps τ and therefore by the number N of intermediate timesteps between $t_0 = 0$ and t. In the limit $\tau \to 0$, results become exact.
One can also choose a Suzuki-Trotter decomposition of higher order. Then the time step error $\mathcal{O}(\tau^2)$ will become smaller at cost of a more complicated structure of the equation. For example one could use the STD of second order:

$$e^{-i\left(\hat{A}+\hat{B}\right)\tau} = e^{-i\hat{A}\tau/2}e^{-i\hat{B}\tau}e^{-i\hat{A}\tau/2} + \mathcal{O}(\tau^3) \quad , \tag{3.95}$$

which is very simple and where the error is of one power smaller. An more complicated Suzuki-Trotter decomposition of order 5 is given by the Forest-Ruth formula [40]

$$e^{-i\left(\hat{A}+\hat{B}\right)\tau} = e^{-i\hat{A}\theta\tau/2}e^{-i\hat{B}\theta\tau}e^{-i\hat{A}(1-\theta)\tau/2}e^{-i\hat{B}(1-2\theta)\tau}e^{-i\hat{A}(1-\theta)\tau/2}e^{-i\hat{B}\theta\tau}e^{-i\hat{A}\theta\tau/2} + \mathcal{O}(\tau^5) \quad , \tag{3.96}$$

where θ is the Forest-Ruth parameter, which is given by $\theta \equiv 1/(2-2^{1/3})$.

3.9.3 TEBD algorithm

As we have seen before, time evolution can be achieved by applying the right side of equation 3.94, which consists only of two-site operators to an MPS, in the best case of canonical normal form, because then all Schmidt coefficients are easily accessible. How to apply an two-site operator to a canonical MPS was explained in section 3.7.2.
The TEBD algorithm looks as follows:

1. Compute the exponentials of the Hamiltonians $\hat{h}_i^e$ for all even bonds between sites $2i$ and $2i+1$
2. Calculate the new Γ-matrices and Schmidt eigenvalues λ for all even bonds by applying the former constructed two-site operators to the canonical MPS
3. Repeat the first two steps, but now for the odd bonds
4. After the application of an even and an odd operator to the MPS measurements of the system can be performed if necessary

This schematic algorithm contains one timestep $\tau = t/N$. To perform a full evolution over the whole simulation time t the TEBD algorithm has to be applied N times on the MPS.
Error sources are on the one hand the former mentioned Trotter error, which can be reduced by smaller timesteps τ or STD of higher order and on the other hand the so called Schmidt error. This error has its roots in the division through small Schmidt values due to computer arithmetic, which has to be done in the application of the two-site operators on the MPS. A schematic representation of the algorithm is in figure 3.18.

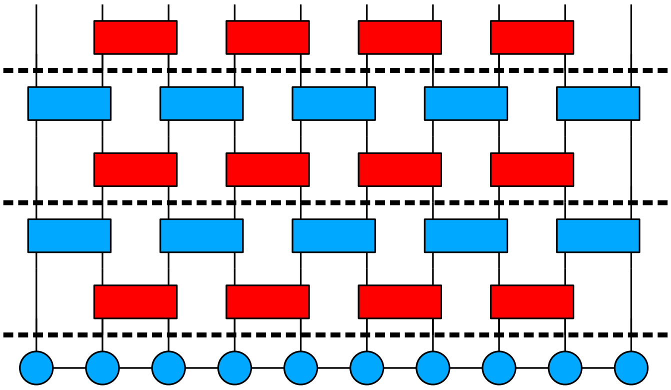

Figure 3.18: Schematic representation of the time evolution of an MPS via the TEBD algorithm. Starting from an MPS (chain with circles), first the two-site operators for the even bonds are applied (red squares) subsequently followed by the application of the operators for the odd bonds (blue squares). This yields a time evolution of time $\tau = t/N$. Repeat this N times to obtain an evolution of the desired time t. At each horizontal dashed line a measurement can be performed.

3.10 Excitations

To bring the theoretical part of this master thesis to a conclusion, the final part is about how to generate excitations from the ground state to see some dynamics in the time evolution[6]. In general two different approaches were realized.
First, an external field could be applied at the initial timestep, to generate a density fluctuation. When starting the simulation the external field is turned off.
Second, one could insert a particle with momentum k.

a.) Applying an external field at $t = 0$:
One can create an initial perturbation of the charge or the spin by applying an external field respectively a chemical potential to the system at time $t = 0$. This fields will result in a local increase or decrease in the particle or the spin density. Then the ground state of the system with the field is calculated with DMRG. Afterwards one turns the external fields off, leading to a non-equilibrium state interesting for time evolution. The time evolution will yield a propagation of the excitations.

In the spinless fermion case due the absence of the spin degree of freedom one only has to deal with an electrically field of the former mentioned (see section 2.2) form

$$\hat{H}_{\mathrm{EF}} = \sum_{i=1}^{L} \epsilon_i \hat{n}_i \quad , \tag{3.97}$$

where $\hat{H}_{\mathrm{EF}}$ is the external field Hamiltonian, L is the systems size, ϵ_l is the electric field on site i and $\hat{n}$ is the number operator. For the models also containing spin, like the Hubbard model or BCS-superconductor, the external field Hamiltonian $\hat{H}_{\mathrm{EF}}$ now looks like

$$\hat{H}_{\mathrm{EF}} = \sum_{i=1}^{L} \epsilon_i \left(\hat{n}_{i,\uparrow} + \hat{n}_{i,\downarrow}\right) + \sum_{i=1}^{L} \frac{B_i}{2} \left(\hat{n}_{i,\uparrow} - \hat{n}_{i,\downarrow}\right) \quad , \tag{3.98}$$

with now two different number operators $\hat{n}_{i,\uparrow}$ respectively $\hat{n}_{i,\downarrow}$ distinguishing between particles with spin up ($\uparrow$) and down ($\downarrow$) and an additional magnetic field B_i operating on site i, as already outlined in section 2.3. For the simulations in chapter 4 only Gaussian shaped external fields were used

$$F(i) = F_0 \, e^{-\frac{(x_0 - i)^2}{2\sigma^2}} \quad \text{with} \quad F_0 = \epsilon \text{ resp. } B/2 \quad , \tag{3.99}$$

generating peaks with the standard deviation of size σ with a maximum at x_0 and an amplitude of size F_0 belonging either to the electric ϵ or the magnetic field $B/2$. Gaussian shaped density perturbations were chosen, because after the splitting of the perturbation in a right and a left moving part the excitations will stay quite stable.

b.) Inserting a particle with momentum k :
The second method how to generate perturbations can be found in the paper of Ulbricht and Schmitteckert[41]. There an additional particle with a specific momentum is added/removed to the ground state by applying the creation/annihilation

---

[6] As one can imagine without motion the time evolution would be rather boring, observing just a static state over time.

operator $g^{\dagger}_{\sigma}/g_{\sigma}$

$$g^{(\dagger)}_{\sigma}(k_0) = \sum_{k} e^{\frac{(k-k_0)^2}{2\sigma_0^2}} c^{(\dagger)}_{k,\sigma} = \sum_{j=1}^{L} \left(e^{(-2\sigma_0^2\pi^2(j-x_0)^2)}\right) \left(e^{\frac{2\pi i(j-x_0)}{L}k_0}\right) c^{(\dagger)}_{j,\sigma} \quad , \tag{3.100}$$

where k are the momentum eigenstates $k \in \left\{-\pi + \frac{2\pi}{L}, \dots, \pi\right\}$, σ_0 is the width of the excitation in momentum space. The excitation will be normalized and centered around x_0

$$|\Psi^{\pm 1}\rangle = \frac{1}{\sqrt{C}} g^{(\dagger)}_{\sigma}(k_0)|\Psi\rangle \quad \text{with} \quad C = \langle\Psi|((g^{(\dagger)}_{\sigma}(k_0))^{\dagger} g^{(\dagger)}_{\sigma}(k_0)|\Psi\rangle \quad . \tag{3.101}$$

Applying the creation operator will result in a quantum state with an additional particle $|\Psi^{+1}\rangle$, whereas the annihilation operator will result in a quantum state with one particle less $|\Psi^{-1}\rangle$.

Unfortunately, this method was not optimal for investigating Andreev reflection. Oscillations occurred during time evolution on every site, the inserted particle had passed. Since Andreev reflection is only visible on these sites, the measurements were noisy. Thus, the method of creating perturbations by applying external fields was applied to all simulations in chapter 4.

3.11 Background subtraction

The phrase *background subtracted* often occurs in chapter 4. This means that additionally to the calculation of the groundstates with applied gaussian-shaped fields to generate a charge or spin perturbation, separate calculations without those fields are performed ($E_0 = 0.0, B_0 = 0.0$). Then the charge ($\hat{n}^0_{\rho}$) respectively the spin density ($\hat{n}^0_{\sigma}$) obtained from these additional calculations are subtracted from the time evolution of the perturbed groundstates at every timestep t for every site i, to smooth out oscillations [18]:

$$\langle \hat{n}_{i,\nu}\rangle(t) - \langle \hat{n}^0_{i,\nu}\rangle \quad \text{with} \quad \nu = \rho, \sigma \quad . \tag{3.102}$$

An alternative method is to subtract the initial groundstate at $t = 0$:

$$\langle \hat{n}_{i,\nu}\rangle(t) - \langle \hat{n}_{i,\nu}\rangle(t=0) \quad \text{with} \quad \nu = \rho, \sigma \quad . \tag{3.103}$$

However, this results in a large negative peak at the initial position of the perturbation x_0 for all timesteps, making the Andreev reflection peak only observable until it reaches x_0. For that reason, the method of choice was the first one.

4 Results

Now, after all theoretical reflections, we can get started with the practical part of this master thesis.

In the first part (4.1) different simulations concerning spin charge separation are performed for the Hubbard model and a closer look on the charge and the spin density for different on-site repulsions U and band fillings n is taken. Furthermore the charge and the spin velocities $u_{\rho,\sigma}$ are measured and compared to the theoretically predicted velocities found in figures 2.8 from [28]. Additionally the Wilson ratio (see equation 2.71) is calculated from the obtained charge and spin velocities and also compared with figure 2.10.

After this we change to the model of spinless fermions and perform simulations resulting in normal and Andreev-like reflections. This is achieved by adjusting the screws of the off-site interaction parameter V on the left and the right side of the interaction boundary in the right way. Results can be found in section 4.2.

Next comes a section (4.3) with simulations concerning Andreev-reflection in a repulsive Hubbard model. Simulations with different matrix dimensions χ, different excitation sizes for the charge and the spin perturbations (section 4.3.2), separate excitations of charge and spin apart from each other (section 4.3.3) and the effect of a charge perturbation on the spin channel of the model are calculated, and the dependence of results on the matrix dimension χ is again investigated (section 4.3.4).

Subsequently, simulations with an attractive Hubbard model are performed in section 4.4. Once more a comparison of normal and Andreev-reflection similar to the simulations for spinless fermions is performed, but now with a model which takes spin into account (section 4.4.1). Following this, simulations with different sizes of the on-site attraction parameter U are accomplished in section 4.4.2. Because of the observation, that no Andreev-reflection occurs for strong on-site attractions, the interaction boundary consisting of one site is changed to a linearly ascending interaction boundary over several sites. Simulations with this new linear interaction boundary are found in section 4.4.3. If the enlarged interaction boundary has the right width, the Andreev effect occurs once again.

Finally, simulations with the s-wave BCS Hamiltonian from equation 2.88 can be found in the last section 4.5.

4.1 Spin charge separation

In section 2.3.2 the phenomenon of different spin u_σ and charge velocities u_ρ due to the uncoupling of the spin and the charge degree of freedom in one-dimensional systems was described (see equation 2.65). This interesting phenomenon has recently attracted the attention of many physicists, since the realization of ultra-cold quantum gases in optical traps gives experimentalists the possibility to investigate this effect and theorists the ability to compare their results with the real world.

C. Kollath et al. made real time studies with an adaptive time-dependent density-matrix renormalization group (adaptive t-DMRG) algorithm, which is an efficient implementation of Vidal's TEBD algorithm in the DMRG framework [42, 43]. Additionally they suggested experimental realizations to make measurements of spin-charge separation possible. They found out that to obtain measurable effects for relatively small one-dimensional quantum systems, rather strong and localized perturbations have to be applied. This unfortunately violates the assumptions of Luttinger liquid theory, leading to a breakdown of spin-charge separation.

Since C. Kollath et al. still use relatively large excitation sizes, Elias Rabel analyzed in his master thesis [18] spin-charge separation generated in contrast to Kollath's work with smaller ones. Calculations of the groundstate were made in his work by an imaginary time evolution ("cooling to $T = 0$"). Afterwards time evolvement was achieved with the help of TEBD.

In the present master thesis all groundstate calculations are performed by DMRG, subsequently followed by time evolution with TEBD. Simulations with the same parameters of the simulations as in Elias Rabel's master thesis are realized, to check if the results are the same[1].

The model system used in the simulations below is the Hubbard model from equation 2.59 containing spin as well as charge degrees of freedom[2]. Perturbations were generated by application of an external field as described in section 3.10. In contrast to the work of C. Kollath, very weak electric and magnetic fields were used similar to Elias Rabel's work.

Important parameters for all simulations are the Hubbard on-site repulsion U between fermions of opposite spin, the maximum matrix dimension χ of the used MPS, the system size L, the number of particles with spin up $N_\uparrow$ respectively spin down $N_\downarrow$ and consequently the mean particle density n calculated in following way

$$n = \frac{n_\uparrow + n_\downarrow}{L} \quad .$$

The parameters for creating the perturbation are the amplitude of the electric E_0 and the magnetic field B_0, the position of the maximum of the fields and hence the perturbation's position x_0 and the excitation's width determined by the standard deviation σ of the Gaussian shaped fields.

The plots in the figures below show the charge expectation value $\langle n_\rho \rangle = \langle n_\uparrow + n_\downarrow \rangle$ respectively spin expectation value $\langle n_\sigma \rangle = \langle n_\uparrow - n_\downarrow \rangle$. The background charge/spin expectation

---

[1] Luckily the same results were obtained.

[2] Naturally due to the absence of spin, spin charge separation can not be found in the spinless fermion model.

value $\langle n_{\rho,\sigma}\rangle_0$ results from a ground state calculation with no external electric $E_0 = 0$ or magnetic $B_0 = 0$ field applied and is subtracted from the mean charge density in all plots in this section.
Also oscillations, called Friedel oscillations, occur in the plots reflecting the ground state with nonvanishing E_0 and/or B_0. To smooth out these charge and especially spin oscillations, the charge as well as the spin density are averaged over three sites.
Charge u_ρ and spin velocities u_σ are estimated by measuring the propagation of the maximum of the excitations over time and subsequent linear fitting. The velocities $u_{\rho,\sigma}$ are then the slopes of the linear fits

$$x_{\rho,\sigma}(t) = u_{\rho,\sigma} \cdot t + x_0 \tag{4.1}$$

Additionally the velocities of the fastest perturbation $u_{\rho,\sigma}$ are also measured by a linear fitting of the extreme end of the Gaussian-shaped perturbations. We will distinguish between the maximum peak and the fastest perturbation velocity by applying indices to the velocities $u_{\max}$ resectively u_{FP}.
In the limit of an infinitesimal perturbation much broader than the average inter-particle spacing, spin and charge velocities are known analytically from the Bethe ansatz (see section 2.1.1 and figures 2.8 and 2.9) and can be compared with the obtained results for $u_{\rho,\sigma}$.
Simulations with different parameter setups are performed for different Hubbard on-site repulsion with $U = 0$ and $U = 4$ and different band fillings varying from $n \approx 0.22$ to $n \approx 0.78$.
For the first experiment, the non-interacting case, values for $U = 0$ and for $n \approx 0.78$ are chosen. Concerning no on-site repulsion, the spin and the charge velocity should be the same ($u_\rho = u_\sigma$) identical to the Fermi velocity v_F found in equation 2.68.
The equality of u_ρ and u_σ can be seen in figure 4.1 and 4.2 with a three respectively a two dimensional plot of the charge on the left and the spin on the right side.
The left side of figure 4.3 shows a linear fit in Matlab of the maximum excitation peak position over time. On the right side a linear fit of the fastest perturbation is shown.
Since the hopping parameter is one ($t = 1$) for all simulations, the spin velocity should deliver the result

$$u_\rho = u_\sigma = v_F = 2 \sin\left(\frac{0.78\pi}{2}\right) = 1.88176 \quad . \tag{4.2}$$

Unfortunately the linear fit's result is $u_{\rho,\max} = u_{\sigma,\max} = (1.905 \pm 0.003)$ respectively $u_{\rho,FP} = (1.94 \pm 0.03)$ and $u_{\sigma,FP} = (1.97 \pm 0.04)$[3]. Although the result is equal for charge and spin at least concerning the margin of error, it differs from the Fermi velocity v_F.
One explanation for the different result is, that the excitation peak, even though the perturbations are small, has a slightly different charge and spin density than $n \approx 0.78$. As one can easily see in figure 4.1, the peak height is about 0.03, resulting in an overall charge/spin density of $n \approx 0.81$. Calculating the Fermi velocity for this density leads to $v_F = 1.911$. Neither the overall charge density of $n \approx 0.78$ nor the maximum density of the peak $n \approx 0.81$ delivers the right solution, but the true value for the density perturbation feels is lying somewhere in between. So the result can be seen as correct.

---

[3] The error of $u_{\rho,\max}$ and $u_{\sigma,\max}$ respectively $u_{\rho,FP}$ and $u_{\sigma,FP}$ are taken from the linfit routine in Matlab.

For the second experiment, an interacting Hubbard model was taken with an on-site repulsion of $U = 4$ and the same band filling of $n \approx 0.78$ as in the experiment before. Since $U \neq 0$, spin-charge separation is expected. The different values of u_ρ and u_σ can be seen in figure 4.4 and 4.5 with a three respectively two dimensional plot of the charge on the left and the spin on the right side.
Figure 4.7 contains a snapshot for two different time steps again at simulation time $t = 0$ (left plots) and $t = 15$ (right plots) with charge density (red lines) and spin density (black lines). Obviously u_ρ and u_σ are not the same any more as expected for an interacting Hubbard model. The results for the velocities (see figure 4.6) obtained by a linear fit are $u_{\rho,\max} = (2.086 \pm 0.003)$ and $u_{\sigma,\max} = (1.225 \pm 0.003)$ respectively $u_{\rho,FP} = (2.14 \pm 0.04)$ and $u_{\sigma,FP} = (1.26 \pm 0.03)$.
In the next experiment the particle density in the interacting Hubbard model, U is again 4, is changed to $n \approx 0.44$. This will lead again to different velocities in comparison to the second experiment, because the charge and spin velocities also depend on the particle density as can be seen in figure 2.8. Again, three and two dimensional plots of the charge and the spin density can be found in figures 4.8 and 4.9 and the linear fits to get the velocities are in figure 4.10. Note that lowering the particle density leads to stronger oscillations especially in the spin density. This affects the measuring of the maximum peak of the spin density. It can be seen in figure 4.10 that the spin peak stays at a constant point in space for about five to six timesteps. The velocities obtained from the slope of the fits are $u_{\rho,\max} = (1.786 \pm 0.002)$ and $u_{\sigma,\max} = (0.777 \pm 0.002)$ respectively $u_{\rho,FP} = (1.78 \pm 0.04)$ and $u_{\sigma,FP} = (0.99 \pm 0.02)$.
Lowering the particle density even more to approximately $n \approx 0.22$ for unchanged $U = 4$ in the interacting Hubbard model results in even stronger oscillations making a velocity measurement almost impossible. Therefore the measurements of the maximum and the fastest perturbation peak were performed by hand instead of applying an automated Matlab script in the experiments above. The results are depicted in the now familiar way from the previous experiments in the figures 4.11, 4.12 and 4.13. Due to the strong oscillations fewer peaks are taken into account for the linear fitting, which increases the fitting error obtained from Matlab. The calculated velocities are $u_{\rho,\max} = (0.97 \pm 0.02)$ and
$u_{\sigma,\max} = (0.23 \pm 0.05)$ respectively $u_{\rho,FP} = (1.07 \pm 0.02)$ and $u_{\sigma,FP} = (0.18 \pm 0.02)$.
For all experiments, the Wilson ratio (see equation 2.71) was also calculated from the measured charge u_ρ and spin u_σ velocities. The error for the Wilson ratio was obtained by the tangent error method, which results in following equation:

$$\Delta R_W = \left|\frac{\partial R_W}{\partial u_\rho}\right| \Delta u_\rho + \left|\frac{\partial R_W}{\partial u_\sigma}\right| \Delta u_\sigma = \frac{2u_\rho}{(u_\rho + u_\sigma)^2} \left\{ \left[\frac{(u_\rho + u_\sigma)}{u_\rho} + 1 \right] \Delta u_\rho + \Delta u_\sigma \right\} . \tag{4.3}$$

A summary of all results obtained from the four different simulations can be found in tables 4.1 and 4.2. Additionally, the results for the different charge and spin velocities of the maximum excitation peak are marked in figure 4.14 on top. The Wilson ratio can be found at the bottom of this figure. This makes the verification of the results easier.

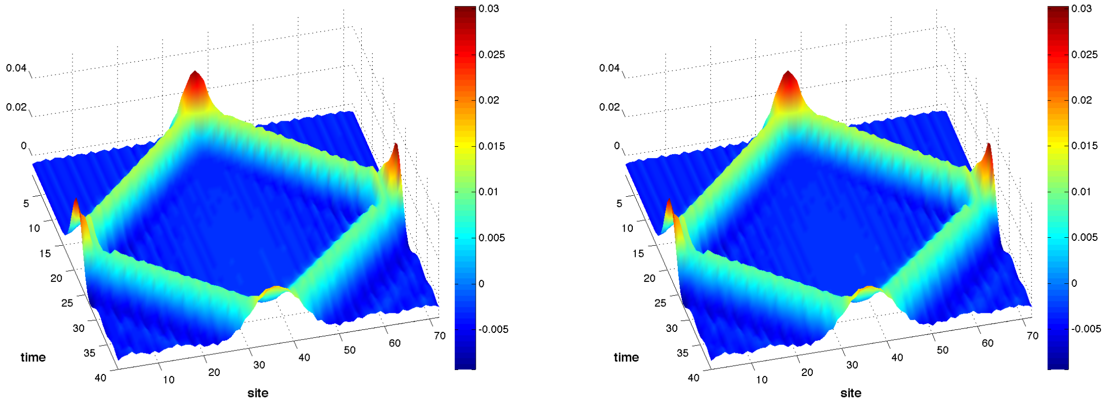

(a) Charge density

(b) Spin density

Figure 4.1: Charge and spin density averaged over 3 sites for a non-interacting Hubbard model. The background is subtracted (see section 3.11). **U=0;n=0.78;**$\chi = 80; L = 72; N_\uparrow = 28; N_\downarrow = 28; E_0 = -0.1; B_0 = 0.2; x_0 = 35; \sigma = 3$.

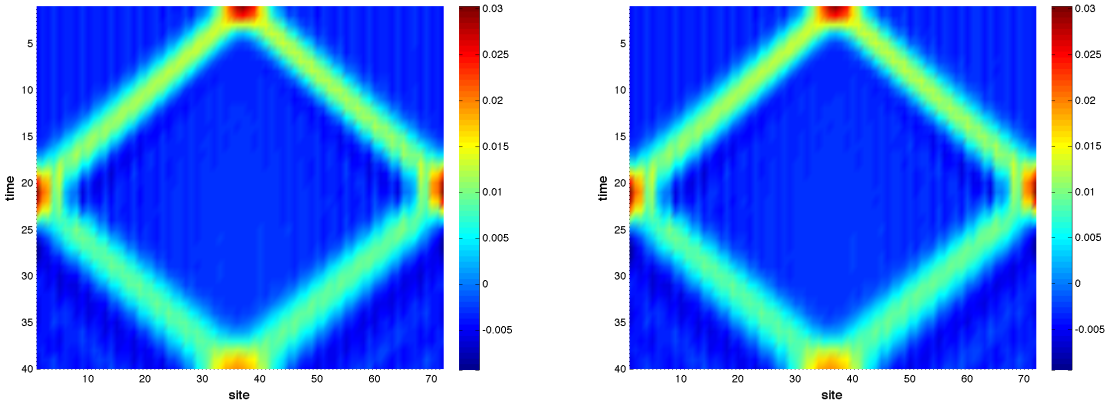

(a) Charge density

(b) Spin density

Figure 4.2: Same as figure 4.1, in a 2d plot.

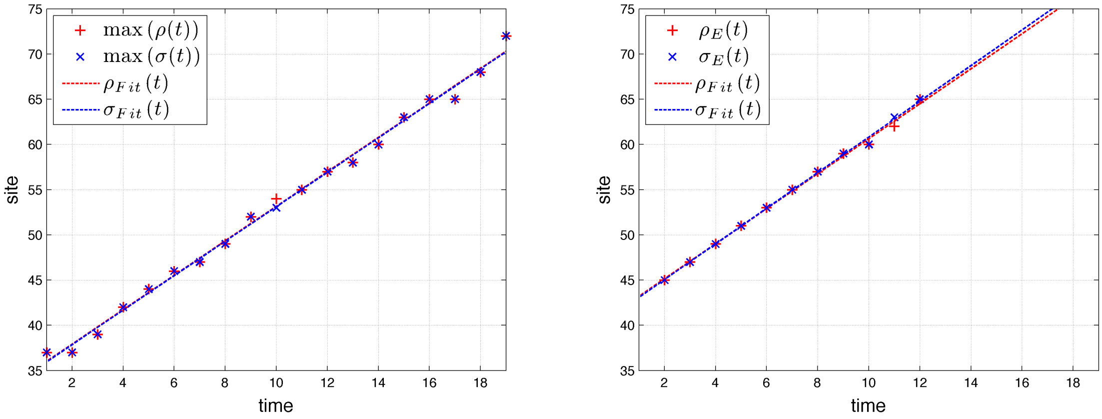

(a) Maximum Peak (b) Fastest Perturbation

Figure 4.3: Linear fit of the maximum excitation peak position for the non-interacting Hubbard model with **U=0** and **n=0.78** for charge ρ (red +) and spin σ (blue x) from figure 4.1 respectively 4.2 on the left side and the fastest perturbation peak on the right. The slope of the linear fits for the maximum peak ($\nu_{Fit}(t) = u_\nu \cdot t + d$, with $\nu = \rho, \sigma$) is $u_\rho = u_\sigma = (1.905 \pm 0.003)$. The velocities for the fastest perturbation peaks are $u_{\rho,FP} = (1.94 \pm 0.03)$ and $u_{\sigma,FP} = (1.97 \pm 0.04)$.

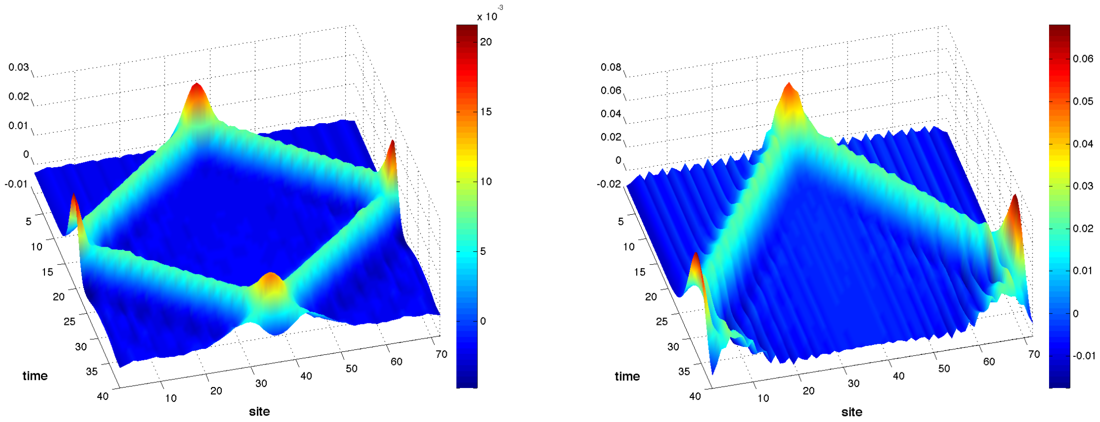

(a) Charge density (b) Spin density

Figure 4.4: Charge and spin density averaged over 3 sites for an interacting Hubbard model. The background is subtracted (see section 3.11). The vertical scale in the left subfigure extends to 20×10^{-3}. **U=4;n=0.78;**$\chi = 80; L = 72; N_\uparrow = 28; N_\downarrow = 28; E_0 = -0.1; B_0 = 0.2; x_0 = 35; \sigma = 3$.

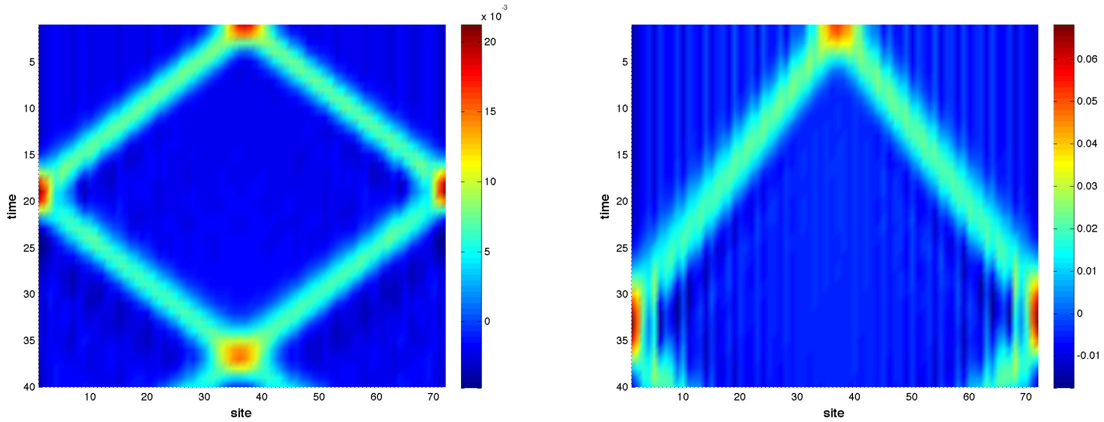

(a) Charge density

(b) Spin density

Figure 4.5: Same as figure 4.4, in a 2d plot.

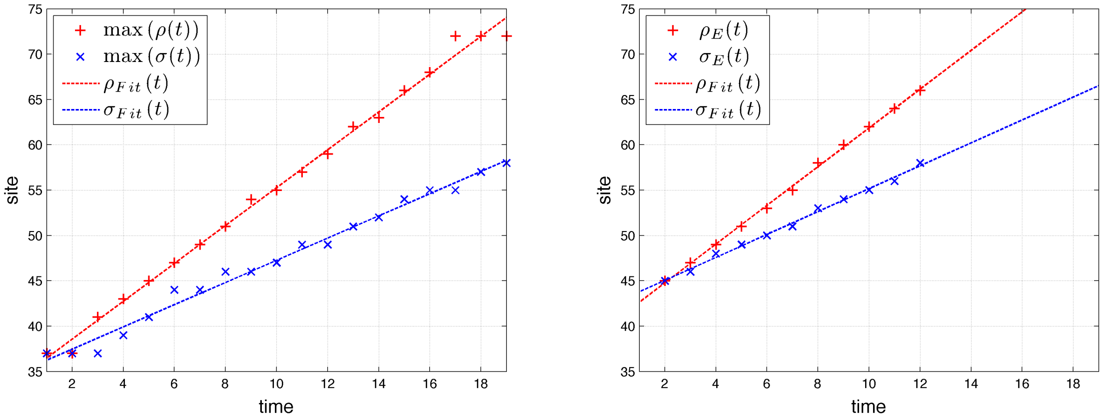

(a) Maximum Peak

(b) Fastest Perturbation

Figure 4.6: Linear fit of the maximum excitation peak position for the interacting Hubbard model with **U=4** and **n=0.78** for charge ρ (red +) and spin σ (blue x) from figure 4.4 respectively 4.5 on the left side and the fastest perturbation peak on the right. The slope of the linear fits ($\nu_{Fit}(t) = u_\nu \cdot t + d$, with $\nu = \rho, \sigma$) is $u_{\rho,\mathrm{max}} = (2.086 \pm 0.003)$ and $u_{\sigma,\mathrm{max}} = (1.225 \pm 0.003)$ respectively $u_{\rho,FP} = (2.14 \pm 0.04)$ and $u_{\sigma,FP} = (1.26 \pm 0.03)$.

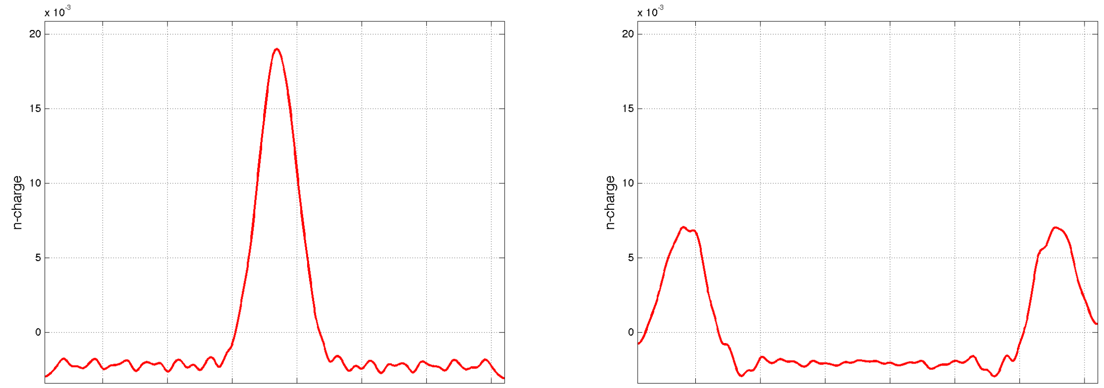

(a) Charge $t = 0$ (b) Charge $t = 15$

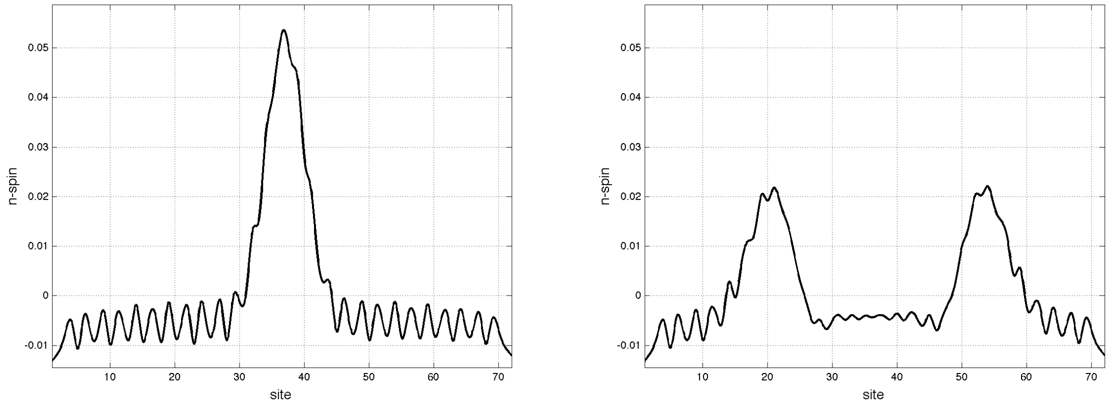

(c) Spin $t = 0$ (d) Spin $t = 15$

Figure 4.7: Snapshots of the charge density (red lines at the top) and spin density (black lines at the bottom) for the interacting Hubbard model at different simulation times t with **t=0** (left plots) and **t=15** (right plots); **U=4**; **n=0.78**; $\chi = 80; L = 72; N_\uparrow = 28; N_\downarrow = 28; E_0 = -0.1; B_0 = 0.2; x_0 = 35; \sigma = 3$. Due to the on-site repulsion U, therefore the velocities of the charge and the spin are not the same, therefor spin-charge separation is observed.

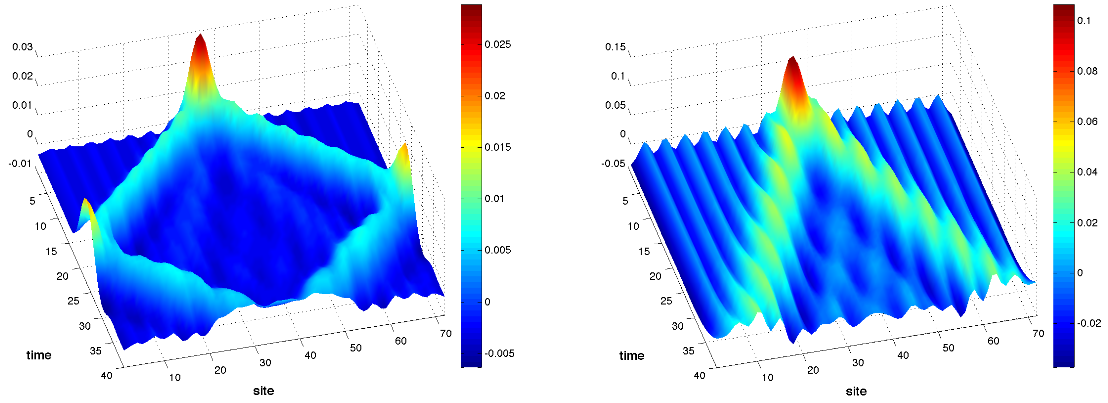

(a) Charge density (b) Spin density

Figure 4.8: Charge and spin density averaged over 3 sites for an interacting Hubbard model. The background is subtracted (see section 3.11). **U=4**; **n=0.44**; $\chi = 80$; $L = 72$; $N_\uparrow = 28$; $N_\downarrow = 28$; $E_0 = -0.1$; $B_0 = 0.2$; $x_0 = 35$; $\sigma = 3$.

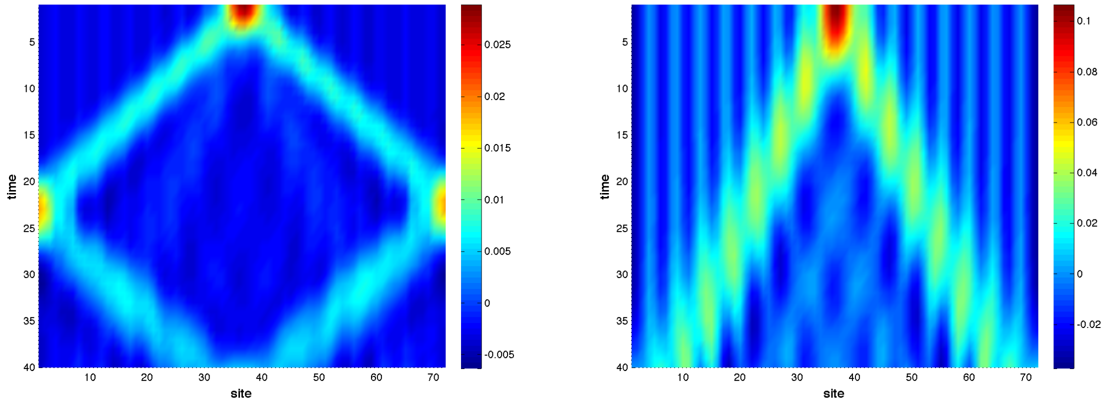

(a) Charge density (b) Spin density

Figure 4.9: Same as figure 4.8, in a 2d plot.

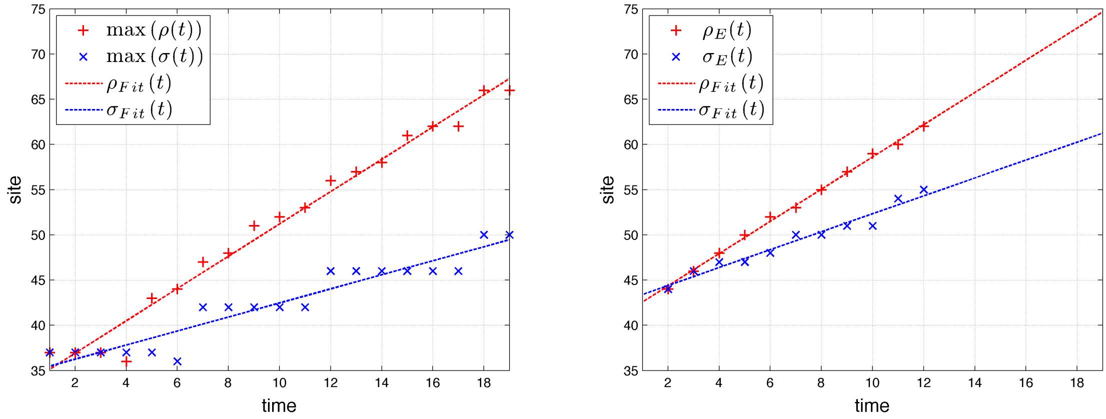

(a) Maximum Peak (b) Fastest Perturbation

Figure 4.10: Linear fit of the maximum excitation peak position for the interacting Hubbard model with **U=4** and **n=0.44** for charge ρ (red +) and spin σ (blue x) from figure 4.8 respectively 4.9 on the left side and the fastest perturbation peak on the right. The slope of the linear fits ($\nu_{Fit}(t) = u_\nu \cdot t + d$, with $\nu = \rho, \sigma$) is $u_{\rho,\max} = (1.786 \pm 0.002)$ and $u_{\sigma,\max} = (0.777 \pm 0.002)$ respectively $u_{\rho,FP} = (1.78 \pm 0.04)$ and $u_{\sigma,FP} = (0.99 \pm 0.02)$.

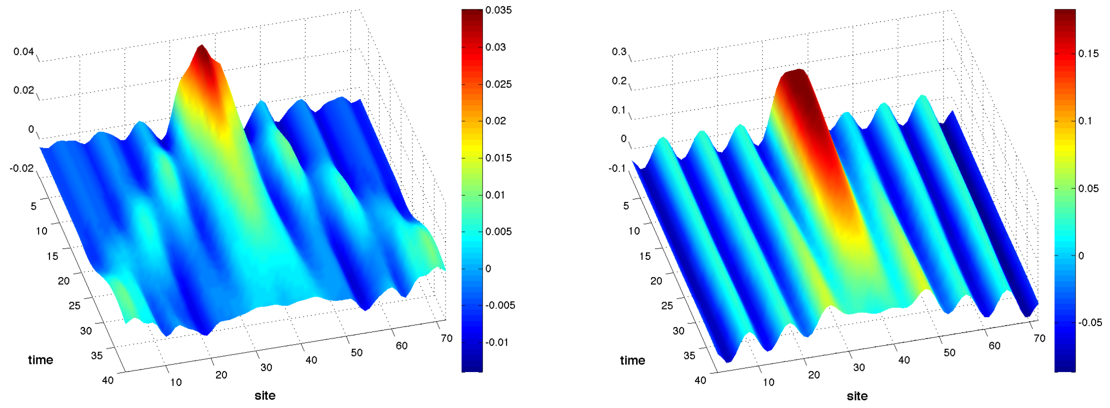

(a) Charge density (b) Spin density

Figure 4.11: Charge and spin density averaged over 3 sites for an interacting Hubbard model. The background is subtracted (see section 3.11). **U=4**; **n=0.22**$\chi = 80; L = 72; N_\uparrow = 28; N_\downarrow = 28; E_0 = -0.1; B_0 = 0.2; x_0 = 35; \sigma = 3$.

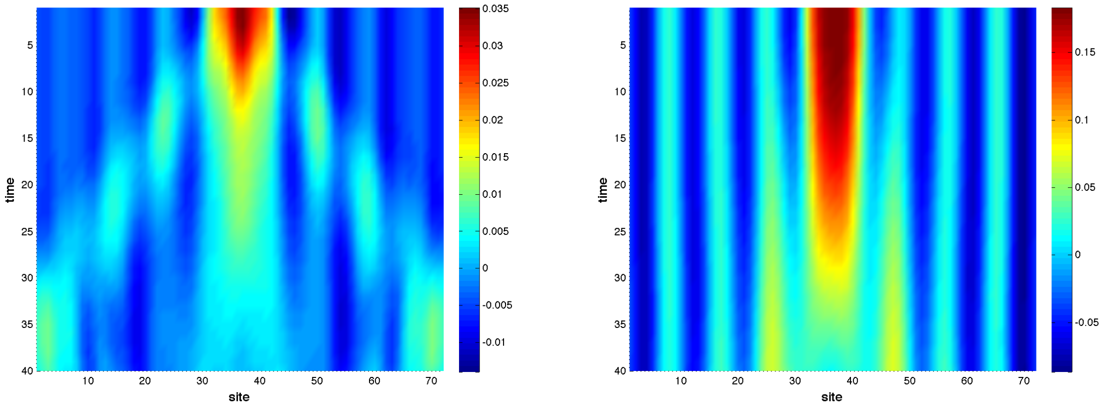

(a) Charge density

(b) Spin density

Figure 4.12: Same as figure 4.11, in a 2d plot.

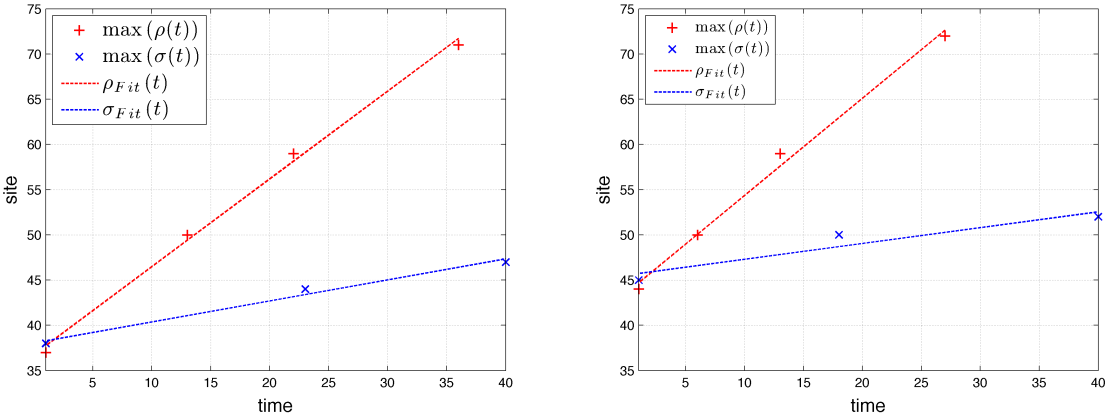

(a) Maximum Peak

(b) Fastest Perturbation

Figure 4.13: Linear fit of the maximum excitation peak position for the interacting Hubbard model with **U=4** and **n=0.22** for charge ρ (red +) and spin σ (blue x) from figure 4.11 respectively 4.12 over time on the left side and the fastest perturbation peak on the right. The slope of the linear fits is $u_{\rho,\max} = (0.97 \pm 0.02)$ and $u_{\sigma,\max} = (0.23 \pm 0.05)$ respectively $u_{\rho,FP} = (1.07 \pm 0.02)$ and $u_{\sigma,FP} = (0.18 \pm 0.02)$.

Table 4.1: Velocities and Wilson ratios of the excitation peaks. This table contains a summary of the results of the four different simulations for different on-site repulsion U and mean particle densities n found in figures 4.1 to 4.13. The values for charge $u_{\rho,\max}$ and spin velocities $u_{\sigma,\max}$ are obtained by linear fitting of the propagation of the maximum peak, the errors $\Delta u_{\rho,\sigma,\max}$ are taken from Matlab's linfit routine. The Wilson ratios $R_{W,\max}$ are calculated from $u_{\rho,\sigma,\max}$ with equation 2.71, the errors are determined by equation 4.3.

	U	n	$u_{\rho,\max}$	$\Delta u_{\rho,\max}$	$u_{\sigma,\max}$	$\Delta u_{\sigma,\max}$	R_W	ΔR_W
Exp. 1	0.0	0.78	1.905	0.003	1.905	0.003	1.000	0.003
Exp. 2	4.0	0.78	2.086	0.003	1.225	0.003	1.260	0.004
Exp. 3	4.0	0.44	1.786	0.002	0.777	0.002	1.394	0.003
Exp. 4	4.0	0.22	0.970	0.020	0.230	0.050	1.600	0.100

Table 4.2: Velocities and Wilson ratios of the fastes perturbation. Otherwise like table 4.1.

	U	n	$u_{\rho,FP}$	$\Delta u_{\rho,FP}$	$u_{\sigma,\max}$	$\Delta u_{\sigma,FP}$	$R_{W,FP}$	$\Delta R_{W,FP}$
Exp. 1	0.0	0.78	1.94	0.03	1.97	0.04	0.99	0.03
Exp. 2	4.0	0.78	2.14	0.04	1.26	0.03	1.260	0.05
Exp. 3	4.0	0.44	1.78	0.04	0.99	0.02	1.29	0.05
Exp. 4	4.0	0.22	1.07	0.10	0.18	0.10	1.70	0.10

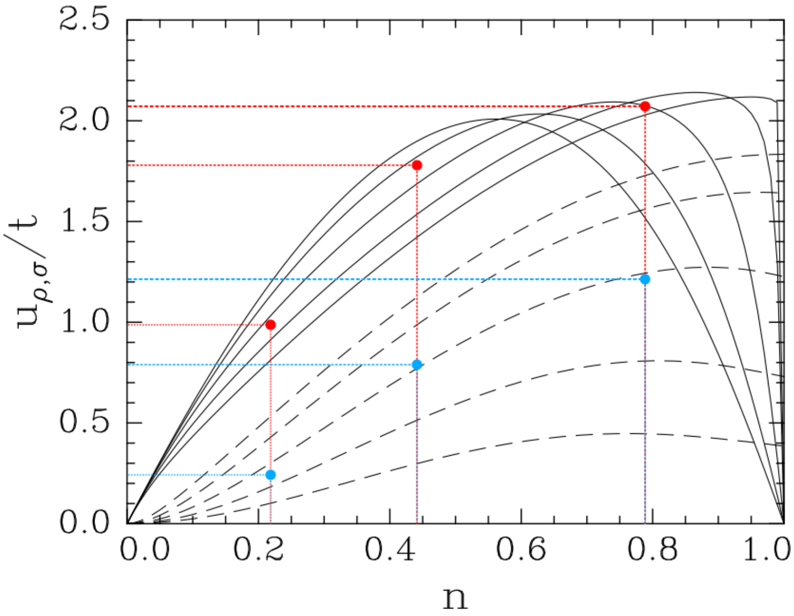

(a) Charge- and Spin velocities

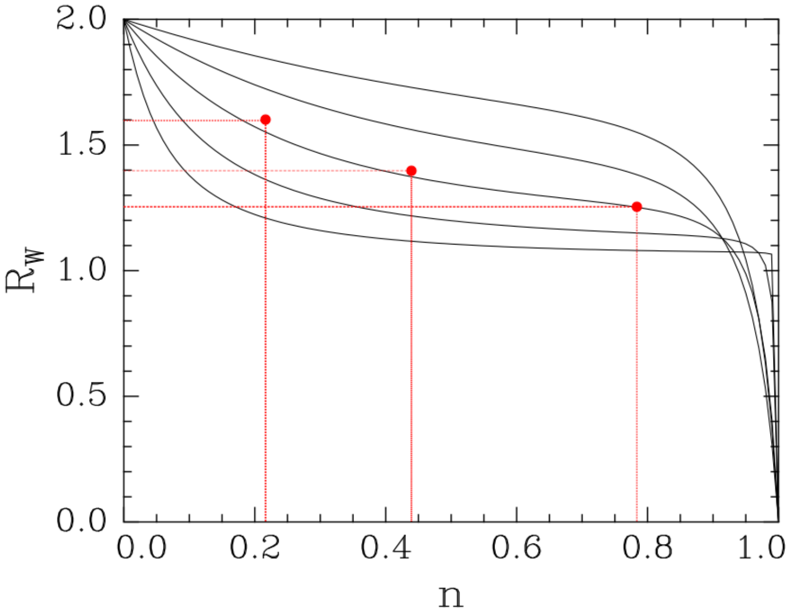

(b) Wilson ratio

Figure 4.14: In this figure the results from experiment 2 to 4 found in table 4.1 are depicted over figures 2.8 and 2.10 taken from [28]. On the top the simulated values for the charge u_ρ (red points) and spin velocities u_σ (blue points) are marked. The solid line in the middle starting from left belong to the charge velocity of $U = 4$ and also the dashed line in the middle is for $U = 4$. One can see a good agreement of the values. The Wilson ratio is shown in the plot at the bottom with $U = 4$ belonging to the middle solid line, the calculated values are depicted as red points. Again, good agreement is found between the analytical and simulated values.

4.2 Normal and Andreev-like reflection for Spinless Fermions

The first system we are going to investigate, where Andreev-like reflection occurs, is the spinless fermion model[4] (see equation 2.57).

A. J. Daley et al. [25] investigated this model[5] and proposed an experimental setup for the observation of Andreev-like reflection using cold atoms trapped in one-dimensional optical lattices. Their results were obtained by time-dependent density matrix renormalization group (TDMRG) methods, analyzing the wave packet propagation of a density propagation across a boundary in the interaction strength. In his master thesis, Elias Rabel [18] also investigated Andreev-like reflection based on the paper of A. J. Daley with slightly different numerical methods. He calculated the ground state with imaginary time evolution and afterwards the real time evolution of the quantum state was simulated with TEBD. In the following simulations, the ground state is calculated with DMRG and subsequent real time evolution with TEBD.

Important parameters for the simulation are the off-site interaction parameter $V_{L,R}$ on the left or the right side of the interaction boundary x_B, again the maximum matrix dimensions χ, the length of the one-dimensional chain L, the number of particles in the system N and thus the mean particle density $n = N/L$.

Important parameters for the charge perturbation are the amplitude of the chemical potential respectively the electric field E_0[6], the position of the maximum peak x_0 at $t = 0$ and its Gaussian width σ.

Additionally, a second external field $\hat{H}_\mathrm{R}$ is introduced:

$$\hat{H}_\mathrm{R} = E_R \cdot \theta(i - x_B) \quad , \tag{4.4}$$

with the step function $\theta(x)$ ensuring that the field only works on the right side of the interaction boundary x_B, thus the index R. The parameter E_R is adjusted in a way that the density on each side of the interaction boundary is nearly the same.

With this method, simulations in the range $|V_L - V_R| \leq t$ were performed. Outside this range, large density oscillations occur near the boundary. The hopping parameter is set to $t = 1$ for all simulations and we will take a non-interacting spinless fermion model on the left side with $V_L = 0$. The off-site interaction parameter V_R on the right side can therefore vary between $V_R = [-1, +1]$. For making a comparison of the results possible, the same parameters as mentioned in the paper of Daley or the master thesis of Rabel are taken, namely $V_L = 0$, $V_R = \pm t$, $t = 1$, $E_0 = -2t$ and $\sigma = 3$.

The Luttinger parameter K_i in the limit $\frac{aV_i}{v_f} \geq 1$ with the lattice spacing a and the Fermi velocity v_F can be approximated in the following way [25]

$$K_i = \frac{1}{\sqrt{1 + \frac{aV_i}{v_F}}} \quad . \tag{4.5}$$

---

[4] Also known as spin-polarized fermions or hard-core bosons in the literature.

[5] Although Daley and et al. described their model as an extended Hubbard model with off-site interactions for spin-polarized fermions (or hardcore bosons), it is nothing more than an euphemism for the spinless fermion model.

[6] Note that a magnetic field would not affect spinless fermions, therefore this parameter is omitted here.

The reflection coefficient γ can then be calculated with equation 2.58. If $\gamma < 0$, the transmitted amplitude through the interaction boundary will be larger than the incident amplitude, resulting in a hole reflected back.
In the following experiments, plots with $V_L = 0$ and $V_R = \pm t$ with $t = 1$ are shown. For the region left of the interaction boundary with no interaction at all, the Luttinger parameter is $K_L = 1$ according to equation 4.5. For the repulsive off-site interaction parameter $V_R = 1$ on the right side, the denominator in equation 4.5 is larger, leading to an decreasing Luttinger parameter compared to the non-interacting case $K_R < K_L$. Then the reflection coefficient will be positive $\gamma > 0$ resulting in a normal reflection of an excitation. The attractive off-site interaction $V_R = -1$ on the other hand leads to an increase in the Luttinger parameter at the interaction boundary $K_L < K_R$, resulting in a negative reflection coefficient $\gamma < 0$, meaning excitations are transmitted with larger amplitude $1 - \gamma$ compensated by a hole traveling in the opposite direction. This is analogous to the Andreev reflection at normal metal-superconductor boundaries. Plots of the density varying with time at each site can be found in figure 4.15 for $V_R = 1$ and in figure 4.16 for $V_R = -1$. In both figures it can be seen that the initial density perturbation splits up into a right- and a left-moving part. The right moving peak is the important one, since it travels in the direction of the interaction boundary. As expected, the repulsive off-site interaction $V_R = 1$ leads to normal reflection whereas the attractive one with $V_R = -1$ results in hole-like reflection. In figure 4.17, the same results are shown again, now from above. It can also be observed that the two transmitted peaks propagate at different velocities, as expected for different interaction parameters. Again a linear fit as in section 4.1 was applied at the maximum peaks of the perturbation after the interaction boundaries and the velocities for both cases were calculated. For the normal reflection the charge velocity is $v_N = (2.90 \pm 0.01)$ and the charge velocity of the Andreev-like reflection is $v_A = (1.27 \pm 0.06)$ (see figure 4.19). In figure 4.18, the normal and Andreev-like reflection are both shown averaged over sites 70 to 75, as a function of time.

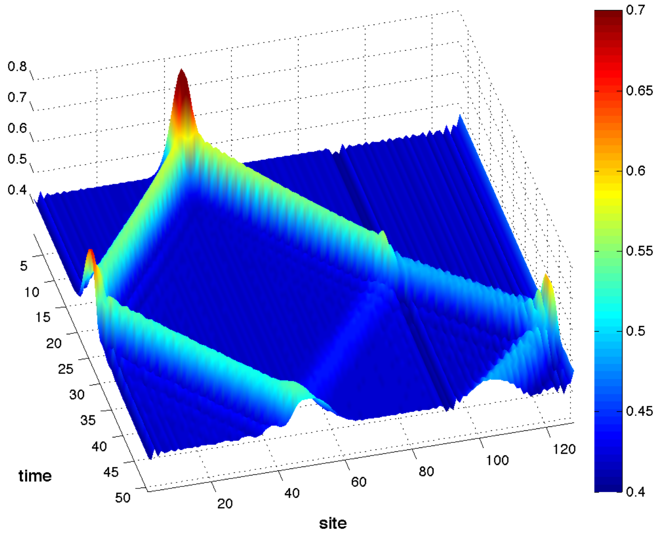

Figure 4.15: Charge density averaged over 3 sites for the spinless fermion model. $V_L = 0; V_R = 1; \chi = 200; L = 128; N = 56; n = 0.44; x_B = 91; E_R = 0.6; E_0 = -2.0; x_0 = 45; \sigma = 3$; **Normal reflection** occurs, since the charge density perturbation hits the interaction boundary coming from a non-interacting region with $V_L = 0$ into a repulsive region with $V_R = 1$.

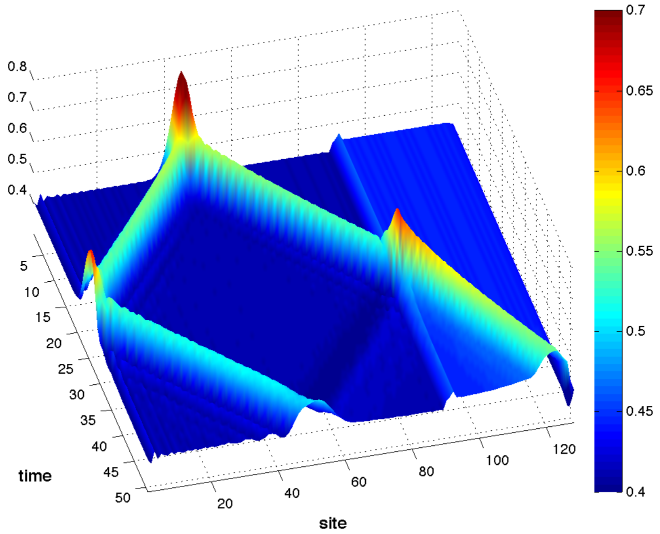

Figure 4.16: Charge density averaged over 3 sites for the spinless fermion model. Same parameters as in figure 4.15, except for $V_R = -1$ and $E_R = -0.6$. **Andreev-like reflection** occurs, since the charge density perturbation hits the interaction boundary coming from a non-interacting region with $V_L = 0$ into an attractive region with $V_R = -1$.

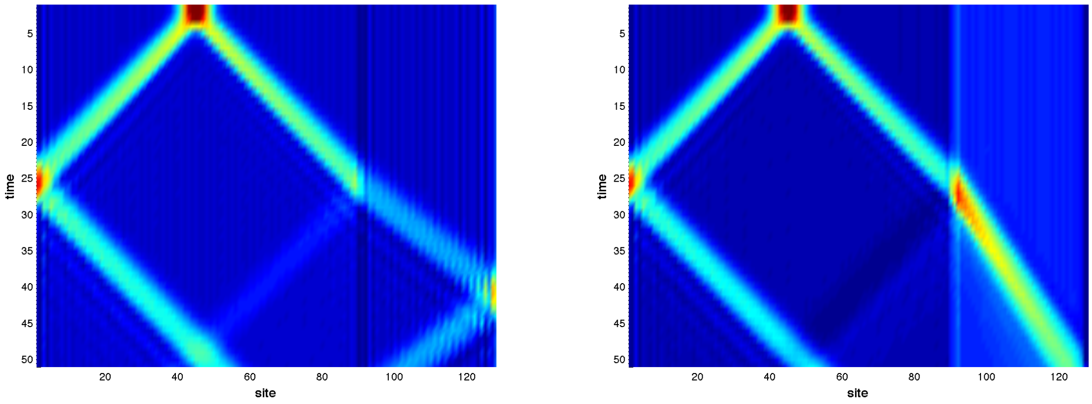

(a) Normal reflection

(b) Andreev-like reflection

Figure 4.17: Comparison of figure 4.15 and figure 4.16 viewed from above. The occurence of a **normal reflection** (left plot) and an **Andreev-like reflection** (right plot) can clearly be seen as the charge density peak hits the interaction boundary after which repulsive respectively attractive interaction occurs. Also the different heights and velocities of the perturbation after the interaction boundary are observable.

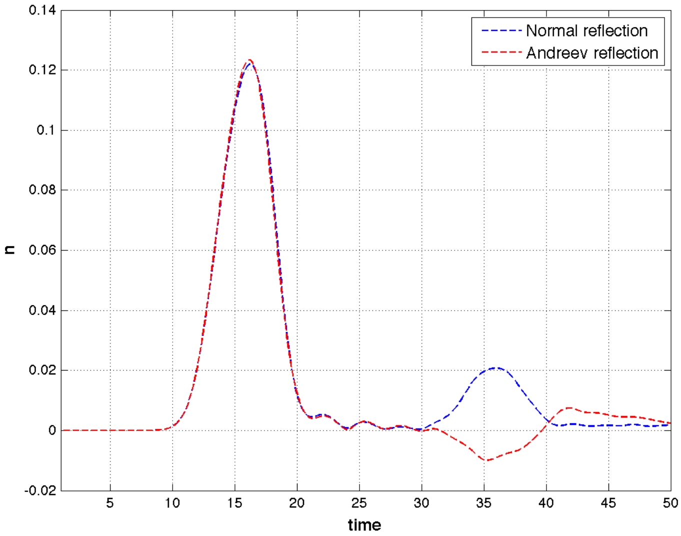

Figure 4.18: This figure shows the charge density over time averaged over sites 70 to 75 for the normal reflection ($V_L = 0, V_R = 1$; blue line) and the Andreev-like reflection ($V_L = 0, V_R = -1$; red line). The occurence of a normal, lower density reflection (blue line) and a reflected hole excitation corresponding to a lower particle density at timesteps $t = 30$ to $t = 40$ is obvious. The background, the groundstate calculated with $E_0 = 0.0$, was substracted to assure a better comparability of the two different simulations.

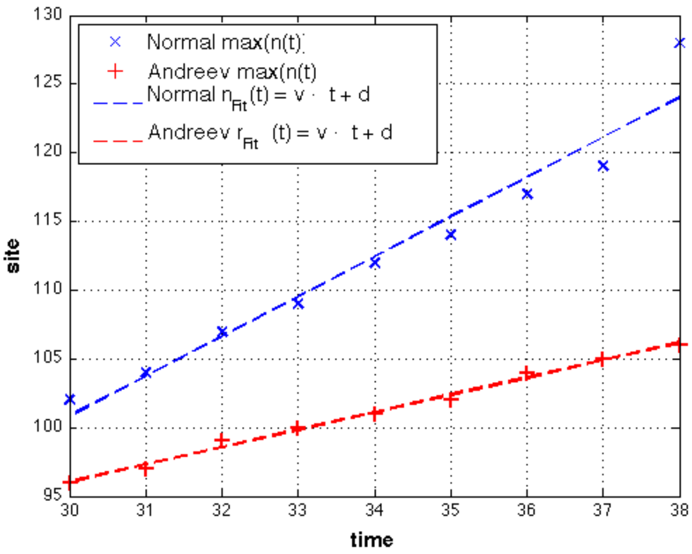

Figure 4.19: Linear fit of the maximum excitation peak position before the scattering, for the cases of **normal reflection** (red +) and **Andreev-like reflection** (blue x) from figure 4.15 respectively 4.16 over time. The slope of the fits is $v_N = (2.90 \pm 0.01)$ respectively $v_A = (1.27 \pm 0.06)$.

4.3 Andreev-reflection in repulsive Hubbard model

In this section, fermions with spin within a Hubbard Hamiltonian 2.59 are treated by simulating a propagation traveling from a repulsively interacting region on the left with $U_L = 8.0$ to a non-interacting region with $U_R = 0.0$. In section 4.3.4, we will also investigate Andreev reflection between two repulsive regions. The interaction boundary x_B is again located between site 90 and 91. The amplitude of the reflections will be quite small, since from $|t/U| \ll 1$ an effective interaction term $V_{i,\text{eff}}$ obtained from perturbation theory [25] follows with $|V_{i,\text{eff}}| \ll t$. Luckily, with numerical simulations provided by MPS techniques, systems beyond the validity of perturbation theory can be investigated.

Charge and spin perturbations are excited again with a Gaussian shaped electric respectively magnetic field, with amplitudes $E_0 = -1.0$ and $B_0 = 0.025$ at site $x_0 = 65$ and $\sigma = 3$. The magnetic field amplitude to generate a spin wave propagation is chosen much weaker than the electric field term, according to Rabel's master thesis [18]. Although the perturbations in this master thesis are twice as small as in [18], the ratio of the electric and the magnetic field amplitude is still the same. In sections 4.3.3 and 4.3.4 we will also investigate separate excitations of spin and charge.

In figure 4.20, one can see that charge and spin degree of freedom are not completely independent from another: an indentation due to the propagating charge is observed in the spin. This signal may be due to numerical issues, see section 4.3.4.

Because of the spin rotational invariance of the Hubbard model, the Luttinger liquid parameter for the spin K_σ is equal to 1 for every possible value of U, leading to a reflection coefficient of $\gamma = 0$. Thus no reflection, neither normal nor Andreev, occurs for the spin degree of freedom (see figure 4.20). The Luttinger parameters for the charge $K_{\rho,L}$ at $U_L = 8.0$ and for the mean fermion density $n \approx 0.5$ can be obtained from figure 2.7 and is approximately $K_{\rho,L} = 0.62$, the parameter for $U_R = 0.0$ is $K_{\rho,R} = 1$. This results in a reflection coefficient of $\gamma = -0.23$, leading to Andreev reflection as can be seen in figure 4.21. Figure 4.22 shows the convergence of the charge signal at time. The reflection coefficient obtained from figure 4.22 results in $\gamma = -0.25$.

Next is the study of the time evolution of the entanglement entropy. For a certain point in time, one can calculate the entanglement entropy between site i and site $i + 1$. It is given by equation 3.14. The base of the logarithm is here 2, the binary logarithm, in contrast to the work of Elias Rabel who took the natural logarithm. In figure 4.23 one sees the entanglement entropy for cuts at each bonds, calculated at $\chi = 1000$. The reflection at the boundary can also be observed in the entanglement entropy.

Figure 4.24 shows the double occupancy per site ($|\uparrow\downarrow\rangle$), where the propagation in the non-interacting Hubbard model on the right side of the interaction boundary is in contrary to the repulsive model on the left really more superconducting-like.

Indeed the density of double occupied states increase as the propagation passes the interaction boundary, showing a Cooper-pair like behavior. Besides the density of not-occupied states ($|0\rangle$) is shown in figure 4.25, resulting in a higher holon (empty state) density being reflected at the interaction boundary, corresponding to the Andreev reflection of a hole.

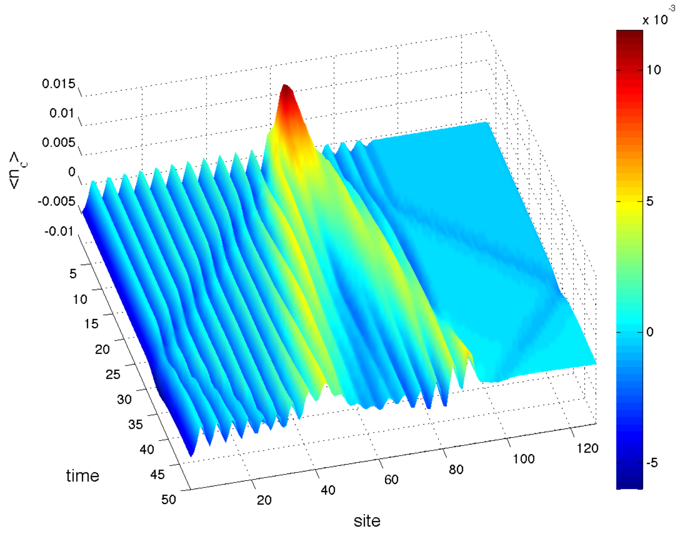

Figure 4.20: Andreev-reflection at an interaction boundary dividing a repulsive Hubbard model from a non-interacting one at site $x_B = 91$: $U_L = 8.0, U_R = 0.0$; $L = 128$, $N_\uparrow = 32, N_\downarrow = 32, n \approx 0.5, E_0 = -1.0, B_0 = 0.025, \sigma = 3, x_0 = 65, \chi = 1000, \tau = 0.05$; **Spin density** n_σ averaged over 3 sites and the background is subtracted (see section 3.11). The vertical scale extends to 10×10^{-3}.

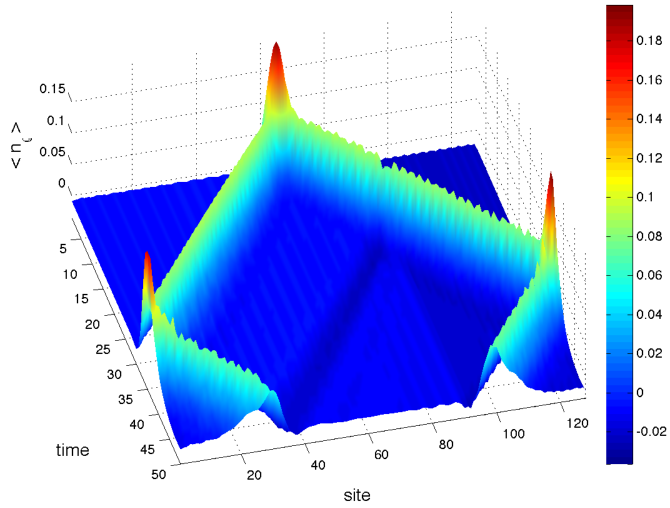

Figure 4.21: Andreev-reflection at an interaction boundary dividing a repulsive Hubbard model from a non-interacting one at site $x_B = 91$: $U_L = 8.0, U_R = 0.0$; $L = 128$, $N_\uparrow = 32, N_\downarrow = 32, n \approx 0.5, E_0 = -1.0, B_0 = 0.025, \sigma = 3, x_0 = 65, \chi = 1000, \tau = 0.05$; **Charge density** n_ρ averaged over 3 sites and the background is subtracted (see section 3.11). See also figure 4.22.

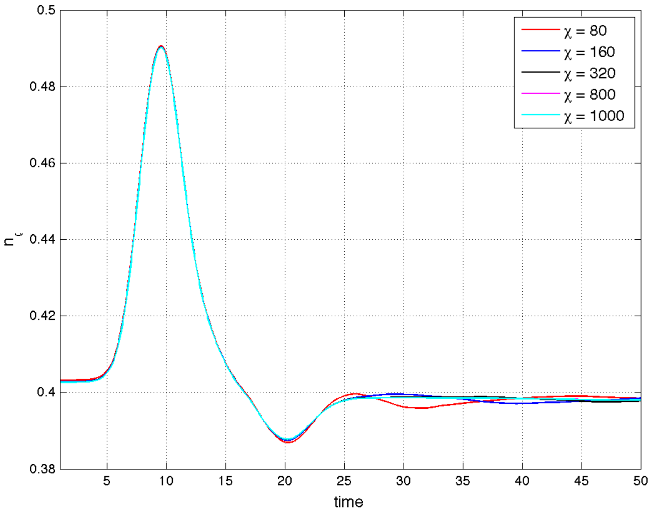

Figure 4.22: This figure shows the **charge density** over time for different matrix dimensions varying from $\chi = 80$ to $\chi = 1000$ averaged over sites 80 to 85 for Andreev reflection as a propagating charge perturbation hits the interaction boundary at site $x_B = 91$ between a repulsive ($U_L = 8.0$) and a non-interacting ($U = 0.0$) Hubbard model. The backscattered hole excitations can be clearly seen between timestep $t = 15$ and $t = 25$.

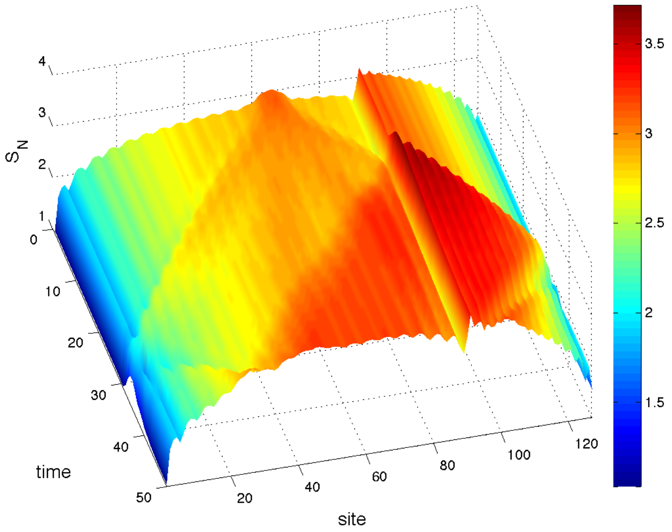

Figure 4.23: Andreev-reflection at an interaction boundary dividing a repulsive Hubbard model from a non-interacting one at site $x_B = 91$: $U_L = 8.0, U_R = 0.0$; $L = 128$, $N_\uparrow = 32, N_\downarrow = 32, n \approx 0.5, E_0 = -1.0, B_0 = 0.025, \sigma = 3, x_0 = 65, \chi = 1000, \tau = 0.05$; **Entanglement entropy** S_N calculated between the sites i and $i + 1$.

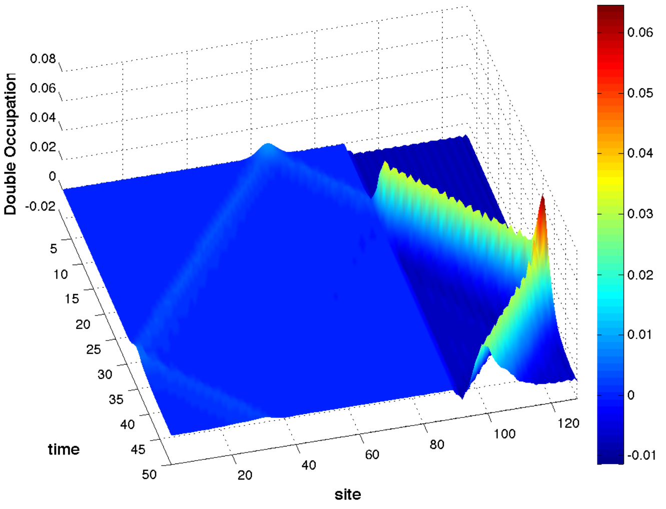

Figure 4.24: Andreev-reflection at an interaction boundary dividing a repulsive Hubbard model from a non-interacting one at site $x_B = 91$: $U_L = 8.0, U_R = 0.0$; $L = 128$, $N_\uparrow = 32, N_\downarrow = 32, n \approx 0.5, E_0 = -1.0, B_0 = 0.025, \sigma = 3, x_0 = 65, \chi = 1000, \tau = 0.05$; Measurement of **double occupied states** ($|\psi_i\rangle = |\uparrow\downarrow\rangle$). The background is subtracted (see section 3.11).

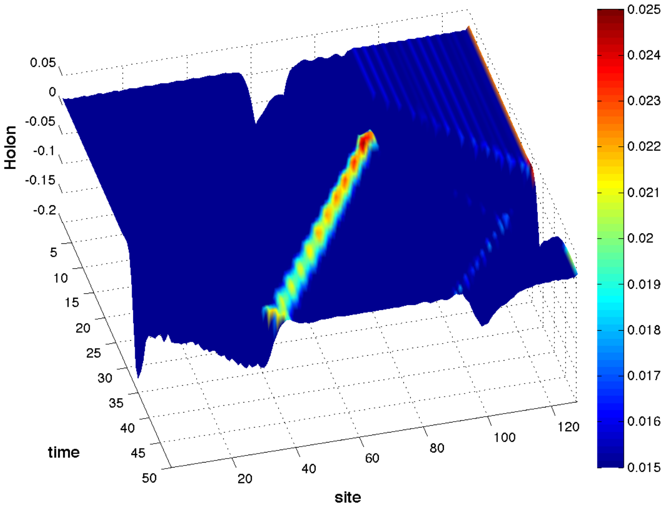

Figure 4.25: Andreev-reflection at an interaction boundary dividing a repulsive Hubbard model from a non-interacting one at site $x_B = 91$: $U_L = 8.0, U_R = 0.0$; $L = 128$, $N_\uparrow = 32, N_\downarrow = 32, n \approx 0.5, E_0 = -1.0, B_0 = 0.025, \sigma = 3, x_0 = 65, \chi = 1000, \tau = 0.05$; Measurement of the **holon density** (non-occupied states ($|\psi_i\rangle = |0\rangle$)). The background is subtracted (see section 3.11).

4.3.1 Convergence in matrix dimension χ

For estimating the reliability of the simulations, different maximum matrix dimensions χ were investigated, varying from $\chi = 80$ to $\chi = 1000$. The absolute difference in the particle densities from the calculation with $\chi = 1000$ and lower matrix dimension ($\chi = 80, 160, 320, 800$) were obtained. They are shown in figure 4.26. Note, the parameter χ is used for both, the DMRG groundstate calculation and the TEBD real-time evolution. Additionally the maximum difference at each timestep is depicted in a semi-log plot in figure 4.27. The obtained values for the maximum difference $\max(d_\chi)$ are $\max(d_{80}) = 0.0361$, $\max(d_{160}) = 0.0100$, $\max(d_{320}) = 0.0032$ and $\max(d_{800}) = 2.0071 \cdot 10^{-4}$.

Figure 4.22 shows the convergence of the charge signal at time for the different matrix dimensions χ averaged over sites 80 to 85. All charge density plots for all different matrix dimensions χ nearly look the same, except the plot for $\chi = 80$ having a second negative peak after the first Andreev peak between times $t = 28$ and $t = 35$. But for the remaining matrix dimensions the difference between the curves is hard to estimate by the human eye.

A comparison of the entanglement entropy for the different matrix dimensions χ at the interaction boundary measured between site 90 and 91 can be found in 4.28. The entanglement entropy increases as the perturbation hits the boundary. Subsequently, more entanglement is created between both parts of the system. The higher the matrix dimension χ the more Schmidt values contribute to the sum in 3.14 and subsequently the more entanglement an MPS quantum state can carry. The data converges at $\chi \gtrsim 800$, showing that the matrix dimension of $\chi = 1000$ used in the main data is sufficient.

Furthermore the maximal truncated weight w_{max} between two measurement steps at times t and $t + \tau$ is plotted over time in figure 4.29 and compared between $\chi = 80$, $\chi = 160$, $\chi = 320$, $\chi = 800$ and $\chi = 1000$. The maximum of the truncated weight between site i and site $i + 1$ is simply calculated by $w_{\text{max}}(t, t + \tau) = \max_i (w_i(t, t + \tau))$. We see that a higher matrix dimension leads to a reduction of the truncated weight. One can also notice that the truncated weight increases sharply at the time when the perturbation hits the boundary. In figure 4.30 one can find the maximum of the truncated weight w over all sites and all times as a function of the maximum matrix dimension χ. Additionally an exponential fit is performed with $f_{\text{fit}}(\chi) = a \cdot e^{b\chi}$, leading to the fit coefficients $a = (1.522 \cdot 10^{-5})$ in the 95% confidence bounds $[3.429 \cdot 10^{-6}, 2.702 \cdot 10^{-5}]$ and $b = (-0.006693)$ in the confidence interval $[-0.01324, -0.0001413]$.

Note that in section 4.3.4, we will see that the trace of the charge signal visible in the spin sector in figure 4.20 may be due to remaining convergence issues in χ.

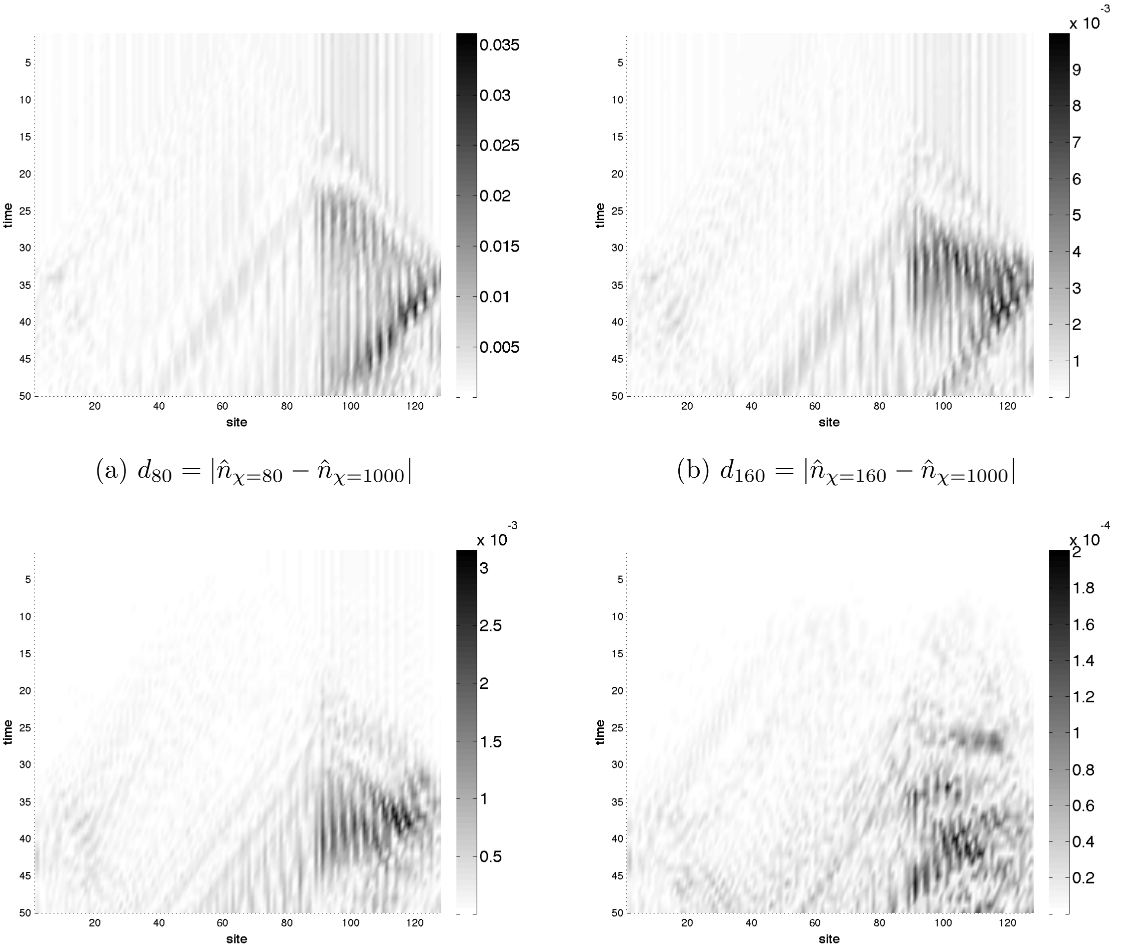

(a) $d_{80} = |\hat{n}_{\chi=80} - \hat{n}_{\chi=1000}|$

(b) $d_{160} = |\hat{n}_{\chi=160} - \hat{n}_{\chi=1000}|$

(c) $d_{320} = |\hat{n}_{\chi=320} - \hat{n}_{\chi=1000}|$

(d) $d_{800} = |\hat{n}_{\chi=800} - \hat{n}_{\chi=1000}|$

Figure 4.26: **Absolute difference** of the **charge density** between calculations with the maximum calculated matrix dimension of $\chi = 1000$ and $\chi = 80$ (top-left), $\chi = 160$ (top-right), $\chi = 320$ (bottom-left), $\chi = 800$ (bottom-right) for simulations of the Andreev reflection between a repulsive $U_L = 8.0$ and a non-interacting $U_R = 0.0$ Hubbard model. Note the different vertical scales.

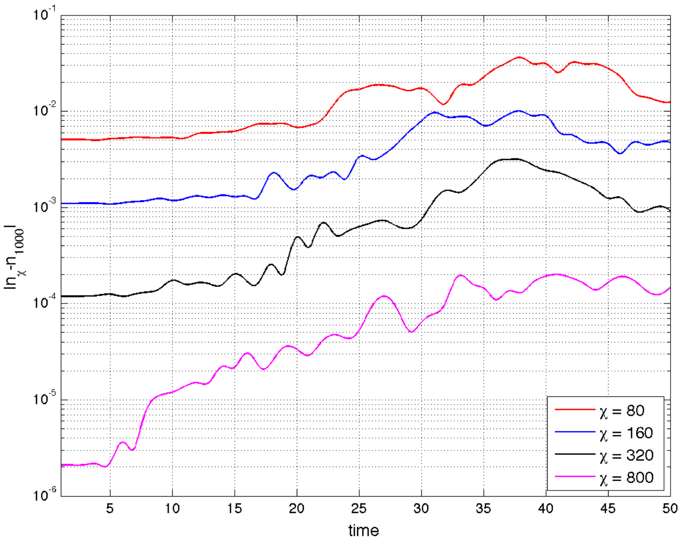

Figure 4.27: **Semi-logarithmic** plot of the **maximum absolute difference** between calculations with different χ.

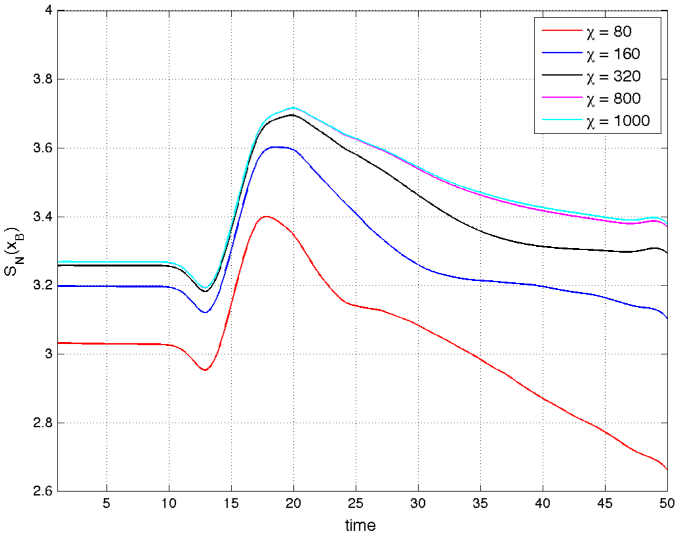

Figure 4.28: Andreev-reflection at an interaction boundary dividing a repulsive Hubbard model from a non-interacting one at site $x_B = 91$. **Entanglement entropy** S_N measured at the interaction boundary x_B for different matrix dimensions χ varying from 80 to 1000. $U_L = 8.0$, $U_R = 0.0$, $L = 128$, $N_\uparrow = 32$, $N_\downarrow = 32$. Note that the data converges at $\chi \gtrsim 800$.

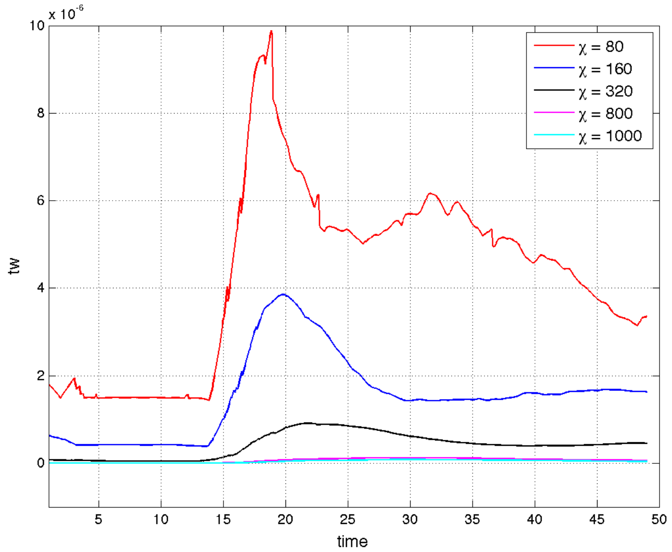

Figure 4.29: Maximum of the **truncated weight** *tw* over all sites as a function of time shown for different matrix dimensions χ from 80 to 1000. Simulations with parameters $U_L = 8.0$, $U_R = 0.0$, $L = 128$, $N_\uparrow = 32$, $N_\downarrow = 32$. The vertical scale extends to 10×10^{-6}.

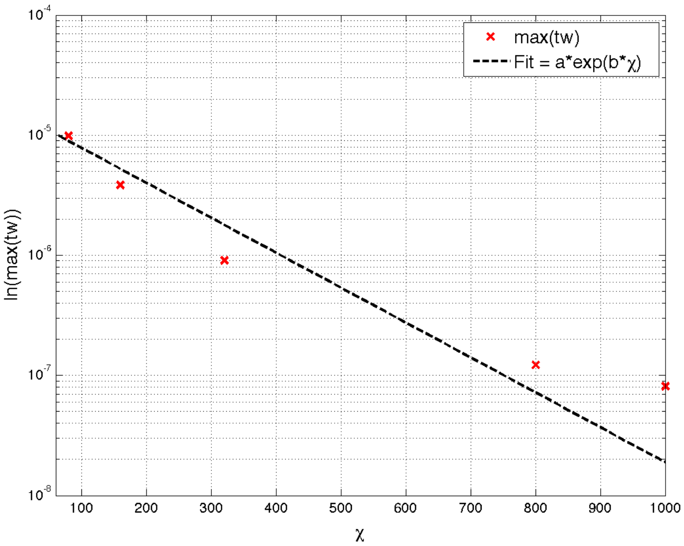

Figure 4.30: Semi-logarithmic plot of the maximum values of the **truncated weight** over all sites and all timesteps taken from figure 4.29 as a function of the maximum matrix dimension χ. Additionally an exponential fit is performed with $f_{\text{fit}}(\chi) = a \cdot e^{b\chi}$, leading to the fit coefficients $a = (1.522 \cdot 10^{-5})$ in the 95% confidence bounds $[3.429 \cdot 10^{-6}, 2.702 \cdot 10^{-5}]$ and $b = (-0.006693)$ in the confidence interval $[-0.01324, -0.0001413]$.

4.3.2 Effect of different excitation sizes

In this section, the transition of charge and spin perturbations from a repulsive Hubbard model 2.59 ($U_L = 8.0$) to a non-interacting one ($U_R = 0.0$) are investigated, like in the section before. But instead of estimating the influence of the maximum MPS matrix dimension χ, we are now observing the influence of the size of the perturbation peaks. Thus we generate different sizes of excitations by varying the amplitude of the applied electric (E_0) and magnetic (B_0) Gaussian-shaped fields. The maximum of the fields is located at site x_0 with a standard deviation of σ. Starting point for the simulations are amplitudes of $E_0 = -2.0$ and $B_0 = 0.05$. This amplitudes were halved until they reach the minimum amplitude values of $E_0 = -0.125$ and $B_0 = 0.003125$ and simulations were performed for every amplitude value resulting from the halving process in between. In all simulations the background (simulations with $E_0 = 0.0$ and $B_0 = 0.0$) is subtracted. Therefore one could not see the different band fillings $n_{\rho,i} = \left(\hat{n}_{i,\uparrow} + \hat{n}_{i,\downarrow}\right)/L$ on the left ($n_L \approx 0.4$) and on the right side ($n_R \approx 0.72$) of the interaction boundary $x_B = 91$. In figure 4.33 the background density, where no fields for the excitations are applied, is depicted, where one can see the different charge densities. In later simulations an additional electric field E_L was applied to guarantee similar band fillings on both sides.
Figure 4.31 shows the charge density for the biggest (left plot with $E_0 = -2.0$ and $B_0 = 0.05$) and the smallest (right plot with $E_0 = -0.125$ and $B_0 = 0.003125$) applied external field sizes. In booth cases Andreev-reflection is observed. The scale of the z-axis of the plots is the same, to better bring out the difference of the perturbation peaks, but the color range is different, to enhance the visibility of the Andreev-reflection.
The same plotting settings (same scale of the z-axis, different range of the colors) are also applied to the spin density plots (4.32). The biggest excitation is again located on the left, the smallest one on the right. One can see that the higher the charge perturbation, the higher the oscillations in the spin density. The spin density gets more peaky compared to the background density in case of the large perturbation. What's more is the effect of the charge perturbation on the spin channel of the system. Clearly a negative peak propagating with the same velocity as the charge perturbation can be seen as a footprint in the spin channel despite the relatively high matrix dimension of $\chi = 400$[7]. If the amplitudes of the excitations become smaller, the imprint of the charge perturbation on the spin density becomes much smaller, resulting in the spin density propagation better coming to light (right plot).
The charge density averaged over sites 75 to 80 depicted over time for the different excitation sizes is shown in figure 4.34. When the applied fields are stronger, the peaks of the excitations are higher. This results of course in a greater hole-like response of the Andreev-reflection. The measured reflection coefficients in figure 4.34 result in $\gamma = -0.186$ for $E_0 = -2.0$ and $\gamma = -0.183$ for $E_0 = -0.125$[8]. Due to the fact that a higher charge perturbation consists of more fermions and the total number of particles in the system is fixed, the band-filling of the charge background is slightly low at high excitation sizes than on low ones (see figure 4.34). In figure 4.35 the plots from figure 4.34 are normalized to the height of the first peak passing the observed sites. The small difference in the charge

---

[7] Investigations of the effect of the maximum matrix dimension χ on the spin density fluctuation can be found in section 4.3.4

[8] The reflection coefficient in this section is different to the coefficient in section 4.3 ($\gamma \approx -0.23$), due to the different band fillings on the left and on the right side of the interaction boundary.

velocities for different excitation strengths (higher charge perturbations, lower background band-filling) yields different arrival-times of the maximum peaks. Nevertheless, one can see that Andreev-reflection is observable for all investigated charge propagation sizes and that the reflected hole is of almost the same size[9].

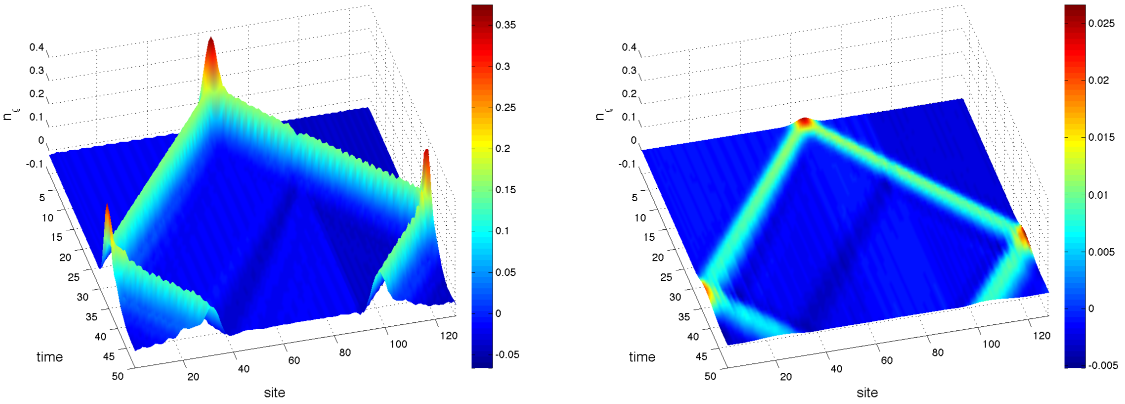

(a) Charge density
$E_0 = -2.0; B_0 = 0.05$

(b) Charge density
$E_0 = -0.125; B_0 \approx 0.003$

Figure 4.31: Fermions with spin: Andreev-reflection at an interaction boundary at site $x_B = 91$: $U_L = 8.0, U_R = 0.0$; $L = 128$, $N_\uparrow = 32, N_\downarrow = 32, n \approx 0.5, \sigma = 3, x_0 = 65, \chi = 400, \tau = 0.05$ for different excitation sizes $\mathbf{E_0}$**= -2.0**; $\mathbf{B_0}$**= 0.05** (left) and $\mathbf{E_0}$**= -0.125**; $\mathbf{B_0}$**= 0.003125** (right); **Charge density** n_ρ averaged over 3 sites, background subtracted (see section 3.11).

---

[9] Note that the size of the Andreev-reflection is also related to the Luttinger liquid parameter K_ρ (see equation 2.58). Because of the different particle densities of the background due to the excitation, K_ρ also varies, as can be seen in figure 2.7.

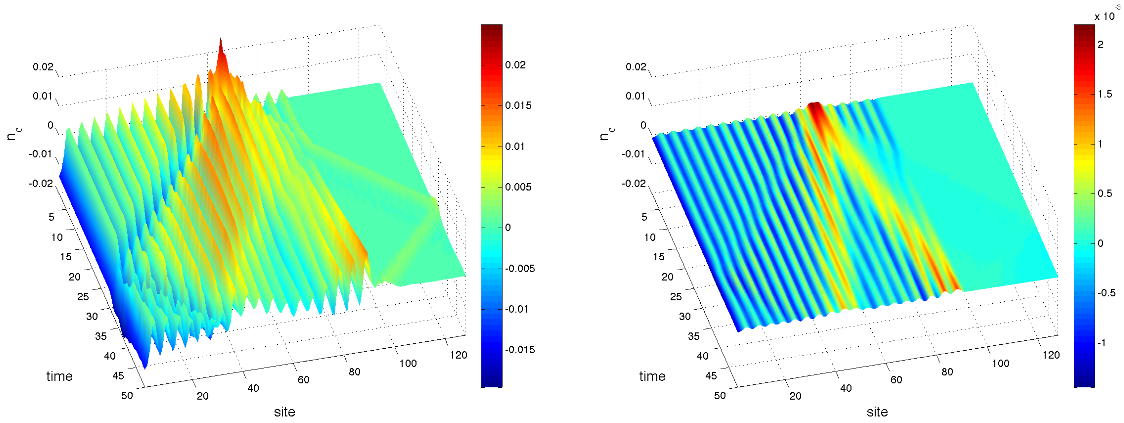

(a) Spin density
$E_0 = -2.0; B_0 = 0.05$

(b) Spin density
$E_0 = -0.125; B_0 \approx 0.003$

Figure 4.32: Fermions with spin: Andreev-reflection at an interaction boundary at site $x_B = 91$: $U_L = 8.0, U_R = 0.0$; $L = 128$, $N_\uparrow = 32, N_\downarrow = 32, n \approx 0.5, \sigma = 3, x_0 = 65, \chi = 400, \tau = 0.05$ for different excitation sizes $\mathbf{E_0 = -2.0; B_0 = 0.05}$ (left) and $\mathbf{E_0 = -0.125; B_0 = 0.003125}$ (right); **Spin density** n_σ averaged over 3 sites, background subtracted (see section 3.11). The vertical scale in the right subfigure extends to 2.2×10^{-3}.

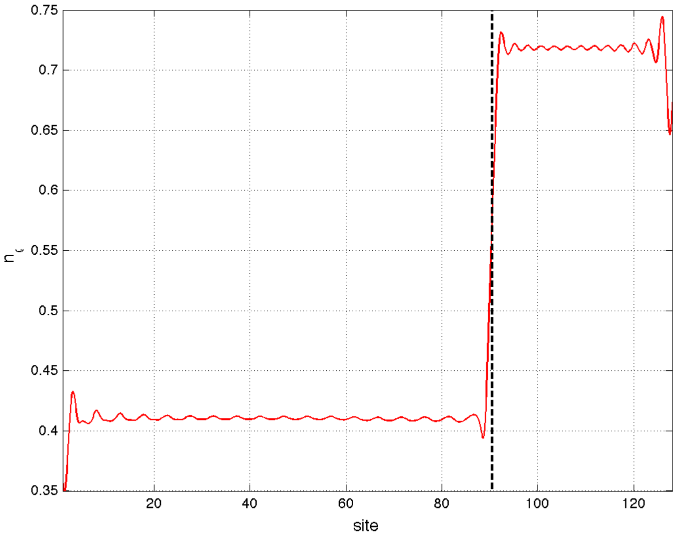

Figure 4.33: Background for the charge density n_ρ averaged over 3 sites with an interaction boundary at $x_B = 91$, which separates the repulsive Fermi-Hubbard model with $U_L = 8.0$ and the non-interacting region with $U_R = 0.0$. The charge density on the left site is approximately $n_L \approx 0.41$ and $n_R \approx 0.72$ on the right. $L = 128$, $N_\uparrow = 32, N_\downarrow = 32, n \approx 0.5, \chi = 400$.

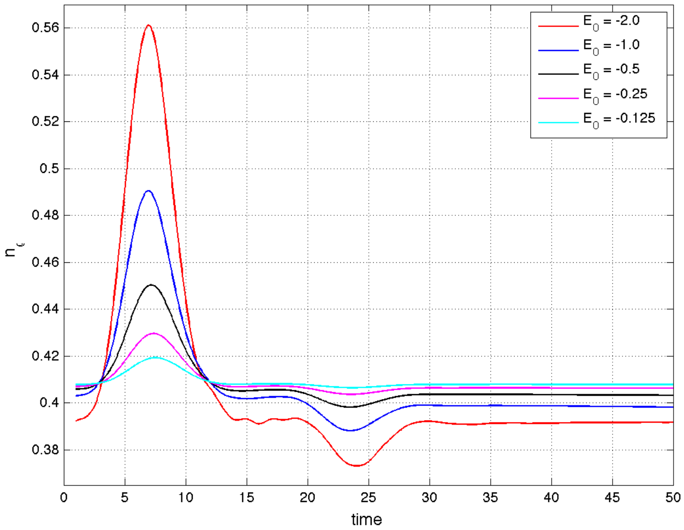

Figure 4.34: Fermions with spin: Andreev-reflection at an interaction boundary at site $x_B = 91$: $U_L = 8.0, U_R = 0.0$; $L = 128$, $N_\uparrow = 32, N_\downarrow = 32, n \approx 0.5, \sigma = 3, x_0 = 65, \chi = 400, \tau = 0.05$ for different excitation sizes from $E_0 = -2.0$ to $E_0 = -0.125$; Charge density n_ρ over time averaged over sites 75 to 80. The measured reflection coefficients result in $\gamma = -0.186$ for $E_0 = -2.0$ and $\gamma = -0.183$ for $E_0 = -0.125$.

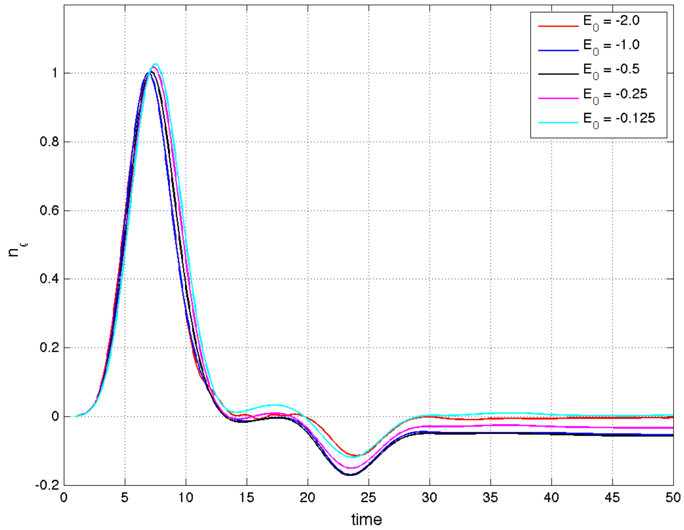

Figure 4.35: Same as figure 4.34, with the height of the peak normalized.

4.3.3 Separate Excitation of Charge and Spin

In the last section (sec. 4.3.2) we have seen that a large perturbation in the charge channel of the Hubbard model has an effect on the spin channel and vice versa. This is investigated more accurate in this section. Until now we have applied excitations on both, the charge and the spin channel, at the same time. Hence the idea is to apply electric and magnetic fields apart from each other and look at the effects on the charge and the spin density. In figure 4.36 the charge density for a large excitation with only an electric field with amplitude $E_0 = -2.0$ (left plot) and a large excitation with only a magnetic field with amplitude $B_0 = 0.05$ (right plot) is presented.

In figure 4.37 the spin density is shown with only a charge perturbation generated in the left plot and a only spin perturbation achieved in the plot to the right.

Logically the charge excitation provides the familiar picture with Andreev-reflection for the charge density in figure 4.36 on the left, and the spin excitation shows the expected behavior on the spin density as can be seen in figure 4.37 on the right. But there is also an effect of the large charge perturbation on the spin channel (see figure 4.36 on the right). Furthermore there is an effect of the spin perturbation on the charge density (see figure 4.37 on the left). In both cases, the excitations in the "wrong" channel are a most a few percent of the main channel. Note that $\chi = 400$ for these calculations, and see also figure 4.39.

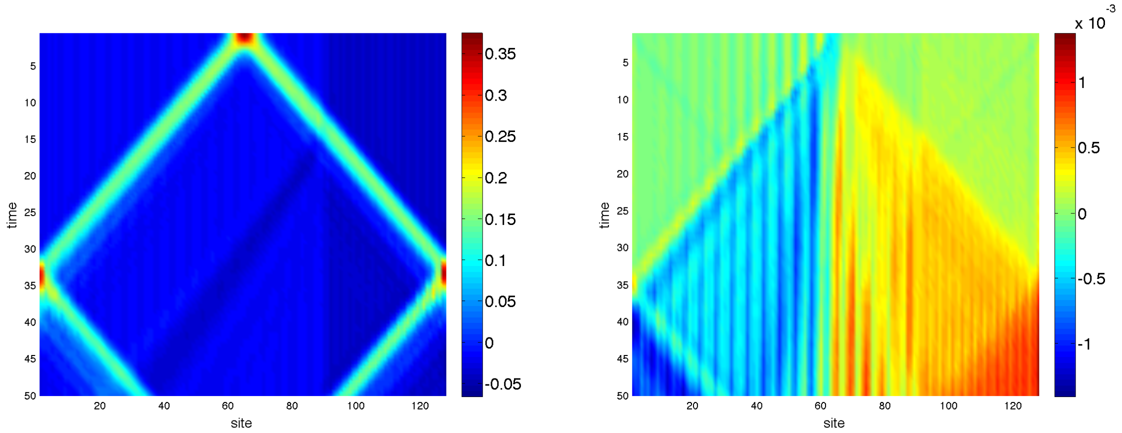

(a) Charge density; Charge excitation

(b) Charge density; Spin excitation

Figure 4.36: Fermions with spin: Andreev-reflection at an interaction boundary at site $x_B = 91$: $U_L = 8.0, U_R = 0.0$; $L = 128$, $N_\uparrow = 32, N_\downarrow = 32, n \approx 0.5, \sigma = 3, x_0 = 65, \chi = 400, \tau = 0.05$ for different excitation for only the charge channel $E_0 = -2.0; B_0 = 0.0$ (left) and only the spin channel $E_0 = 0.0; B_0 = 0.05$ (right); Charge density n_ρ averaged over 3 sites, background subtracted (see section 3.11). The vertical scale in the right subfigure extends to 1.2×10^{-3}.

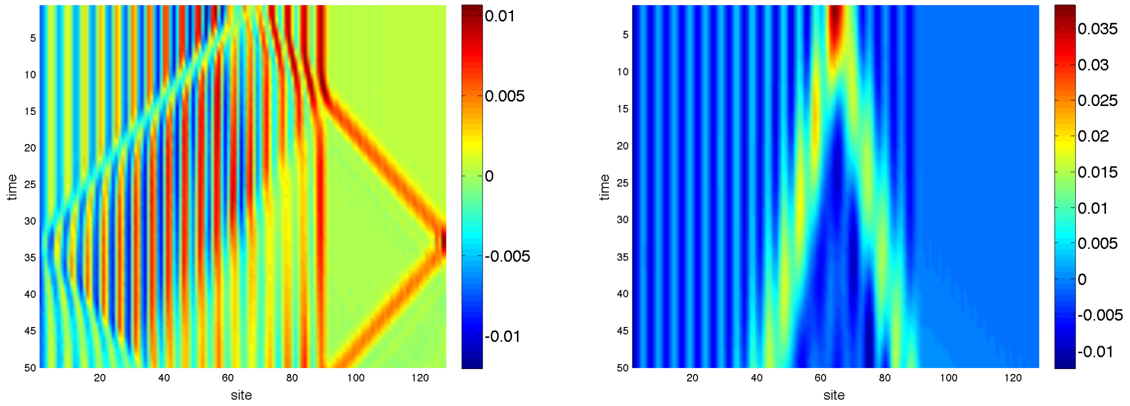

(a) Spin density; Charge excitation

(b) Spin density; Spin excitation

Figure 4.37: Fermions with spin: Andreev-reflection at an interaction boundary at site $x_B = 91$: $U_L = 8.0, U_R = 0.0$; $L = 128$, $N_\uparrow = 32, N_\downarrow = 32, n \approx 0.5, \sigma = 3, x_0 = 65, \chi = 400, \tau = 0.05$ for different excitation for only the charge channel $E_0 = -2.0; B_0 = 0.0$ (left) and only the spin channel $E_0 = 0.0; B_0 = 0.05$ (right); Spin density n_σ averaged over 3 sites, background subtracted (see section 3.11).

4.3.4 Andreev scattering between two repulsive regions, and influence of the Charge on the Spin for different χ

In this section the effect of a pure charge excitation on the spin density is investigated for different MPS matrix dimensions χ. For this, a charge excitation on site $x_0 = 65$ with amplitude $E_0 = -1.0$ and $\sigma = 3.0$ is applied on a repulsive Hubbard model with an interaction boundary on site $x_B = 91$ separating areas with $U_L = 10.0$ and $U_R = 2.0$. Note that this time different on-site repulsions than in the simulations before are used. Also an additional external electric field E_L is applied to the left side of the interaction boundary.

$$\hat{H}_{\mathrm{L}} = E_L \cdot \theta\left(x_B - i\right) \quad , \tag{4.6}$$

where x_B is the interaction boundary, i denotes the current site, E_L is amplitude of the external electric field and θ is the step function. The size of this field is properly chosen to get approximately the same size of particle density n on the left n_L and on the right n_R side of the system ($E_L = 0.06$).

The charge density of the simulation with the maximum investigated matrix dimension of $\chi = 1000$ is depicted in figure 4.38. As before, Andreev reflection can clearly be observed, now as the charge travels from a region with on-site repulsion $U_L = 10.0$ to a region with weaker on-site *repulsion* $U_R = 2.0$.

The spin density of simulations with different matrix dimensions going from $\chi = 80$ to $\chi = 1000$ are represented in figure 4.40. As one can see, increasing the matrix dimension lowers the effect of the charge perturbation on the spin density. At first a high effect on the spin density can be seen for low $\chi = 80$ (figure 4.40) plot (a) respectively $\chi = 160$ (figure 4.40 plot (b)). As the matrix dimension rises to $\chi = 320$ (plot (c)), the effect gets smaller, until for high matrix dimensions ($\chi = 640$ (plot (d)) or $\chi = 1000$ (plot (e))) only numerical noise is observed. The maximum absolute value of the spin density, which should be zero because of the absence of an applied magnetic field, as a function of the matrix dimension χ is shown as a semilogarithmic plot in figure 4.39. Apparently, the higher the matrix dimension χ is, the smaller the effect in the spin density. Thus, the excitations with charge velocity observed in the earlier results appear to be (at least mostly) a numerical issue, and are not just due to a large size of excitation. Note that in figure 4.40 this affects not only the signal with charge velocity, but also spin oscillations in the initial state.

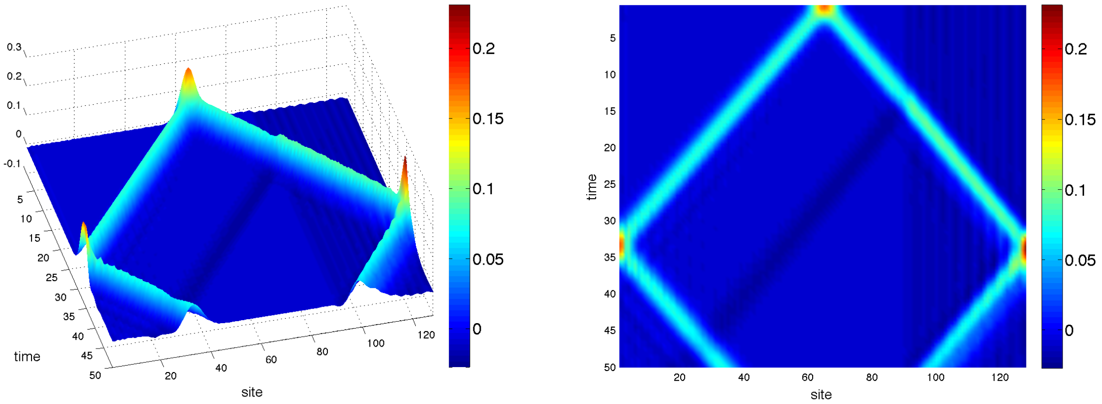

(a) Charge density (b) Charge density

Figure 4.38: Fermions with spin: Andreev-reflection at an interaction boundary at site $x_B = 91$: $\mathbf{U_L = 10.0, U_R = 2.0}$; $L = 128$, $N_\uparrow = 32, N_\downarrow = 32, n \approx 0.5, \sigma = 3, x_0 = 65, \chi = 1000, \tau = 0.05, E_0 = -1.0; B_0 = 0.0; E_L = 0.06$. Charge density averaged over three sites, background subtracted (see section 3.11).

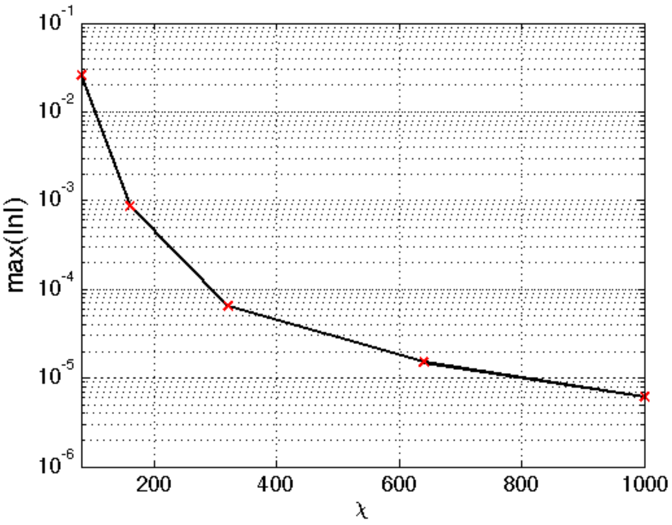

Figure 4.39: Effect of the charge density on the maximal absolute value of the spin density $(\max(|n|))$ as a function of the matrix dimension χ depicted as a semilogarithmical plot.

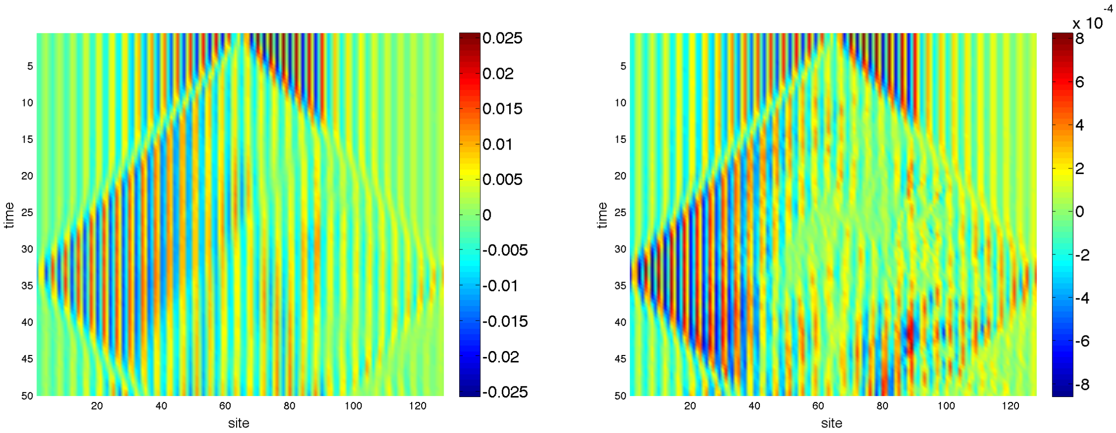

(a) Spin density
$\chi = 80$

(b) Spin density
$\chi = 160$

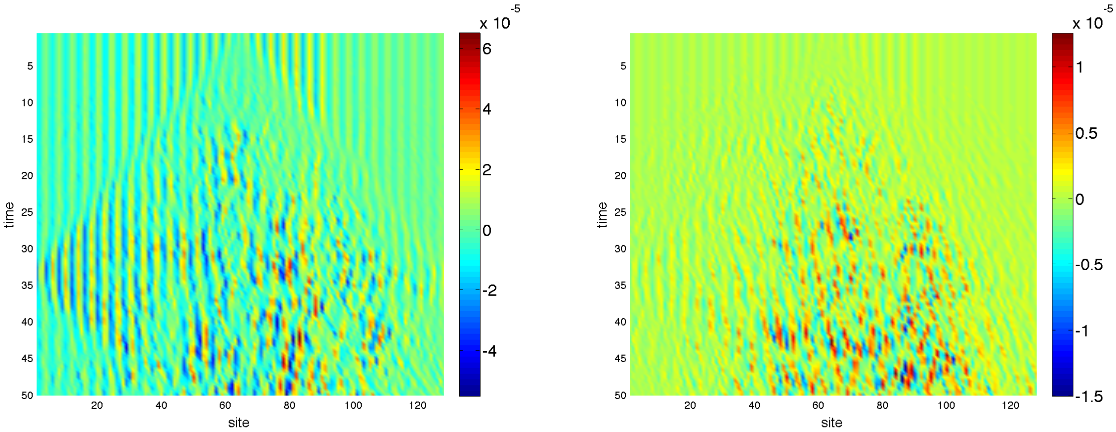

(c) Spin density
$\chi = 320$

(d) Spin density
$\chi = 640$

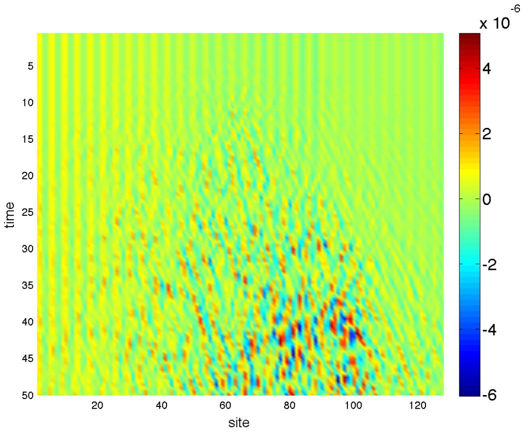

(e) Spin density
$\chi = 1000$

Figure 4.40: Fermions with spin: Andreev-reflection at an interaction boundary at site $x_B = 91$ for different matrix dimensions χ going from 80 to 1000 with no magnetic field applied. $U_L = 10.0, U_R = 2.0$; $L = 128$, $N_\uparrow = 32, N_\downarrow = 32, n \approx 0.5, \sigma = 3, x_0 = 65, \chi = 1000, \tau = 0.05, E_0 = -1.0; B_0 = 0.0; E_L = 0.06$. **Spin density averaged over three sites, background subtracted** (see section 3.11). Note the different vertical scales.

4.4 Andreev-reflection in the attractive Hubbard model

4.4.1 Normal and Andreev-reflection

For the following simulations, an attractive Hubbard model with negative on-site interaction ($U < 0$) is taken into account. In this model, fermions form bound states with energy $|U|$, so called hard core bosons. If a fermion jumps to a neighboring site, a pair of fermions has to break, leading to a effective hopping term with $t_{eff} \propto \frac{t^2}{U}$. Two different on-site attractions are applied on the model, U_L left of the interaction boundary and U_R on the right site. Because of the different on-site attraction terms, different particle densities appear between the two regions. Therefore an additional external electric field E_R is applied on the right side of the model over the whole simulation time to obtain approximately the same particle densities.

The side of the model with a more negative on-site attraction is the more superconducting one. The side with the less negative on-site attraction becomes more metal-like in comparison with the other one. According to equation 2.72, Andreev-reflection will occur for a transition from a non-interacting region respectively a region with weak on-site attraction to a region with stronger on-site attraction. On the contrary, normal reflection will occur for transitions from regions with strong attraction to regions with weak or non attraction.

To show this, simulations similar as for the spinless fermion model in section 4.2 were made for the attractive Hubbard model. Only charge perturbations were excited, by applying only a Gaussian-shaped electric field omitting the application of a magnetic field for the spin density at first.

Normal reflection is shown in figure 4.41 as the charge perturbation crosses the interaction boundary of an attractive Hubbard model on the left with $U_L = -2.0$ to a region with no interaction at all on the right ($U_R = 0.0$). Additionally, the charge density in the region with on-site attraction on the left is more peaky than on the right. This is because of the fact that in the more attractive region the fermions would tend to build pairs caused by the energy gain of fermion bound states in the attractive Hubbard model.

Andreev-reflection can be seen in figure 4.42. In this figure the charge perturbation comes from a non-interacting region to a region with an on-site attraction term of size $U = -2.0$. Now the more peaky area is the region on the right side of the interaction boundary.

For a better comparison the results for the normal and the Andreev-reflection for the attractive Hubbard model are shown from above next to each other in figure 4.43 (normal reflection on the left, Andreev-reflection on the right).

The charge density over time averaged over sites 76 to 80 is shown in figure 4.44. Because of the different interaction parameters and therefore the different heights of the charge peaks, the curves have first been normalized to the peak maximum of the incident perturbation. The positive normal and the negative Andreev-reflection peaks are clearly observable. Due to the different attractions the velocities of the peaks are also slightly different. As predicted from Luttinger liquid theory, the peak for the normal reflection coming from an attractive region is a little bit slower than the Andreev-reflection peak, which is located in a region with no interaction. From figure 4.44 the reflection coefficient results in $\gamma_A = -0.14$ for the Andreev and in $\gamma_N = 0.20$ for the Normal reflection. The reflection coefficient obtained from figure 2.9 and equation 2.72 yields $\gamma_{N/A} = +/-0.12$.

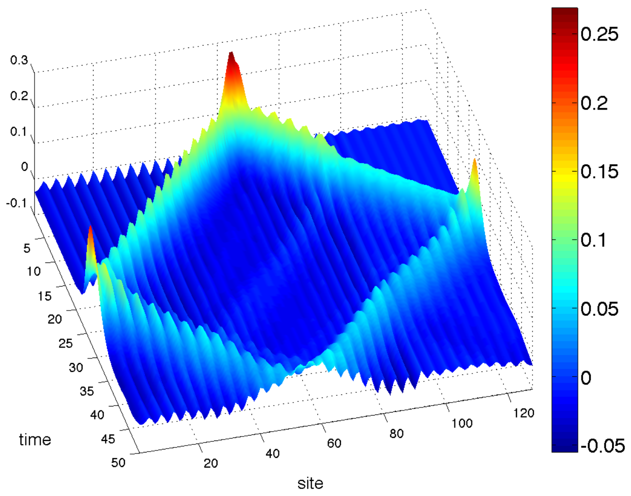

Figure 4.41: Charge density averaged over 3 sites for an attractive Hubbard model. $U_L = -2.0; U_R = 0.0; \chi = 640; L = 128; N_\uparrow = 32; N_\downarrow = 32; n = 0.5; x_B = 91; E_R = 0.0.5265; E_0 = -0.5; x_0 = 65; \sigma = 3$; **Normal reflection** is observed, as the charge density perturbation hits the interaction boundary coming from a interacting region with attractive interaction $U_L = -2.0$ into a non-interacting region with $U_R = 0.0$. Background subtracted (see section 3.11).

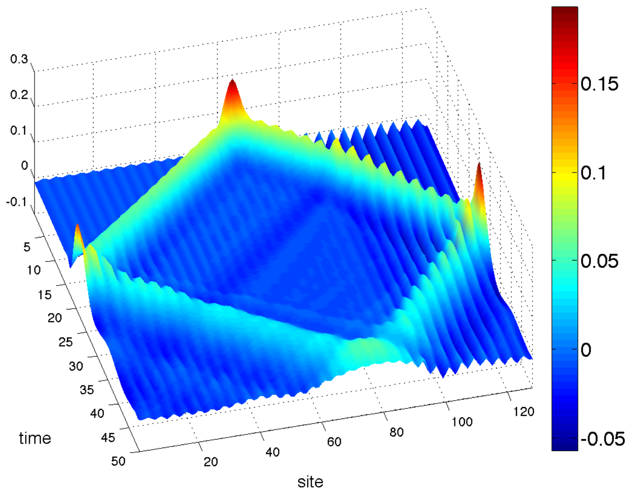

Figure 4.42: Charge density averaged over 3 sites for an attractive Hubbard model. $U_L = 0.0; U_R = -2.0; \chi = 640; L = 128; N_\uparrow = 32; N_\downarrow = 32; n = 0.5; x_B = 91; E_R = -0.55; E_0 = -0.5; x_0 = 45; \sigma = 3$; **Andreev-reflection** is observed, as the charge density perturbation hits the interaction boundary coming from a non-interacting region with $U_L = 0$ into an attractive region with $U_R = -2.0$. Background subtracted (see section 3.11).

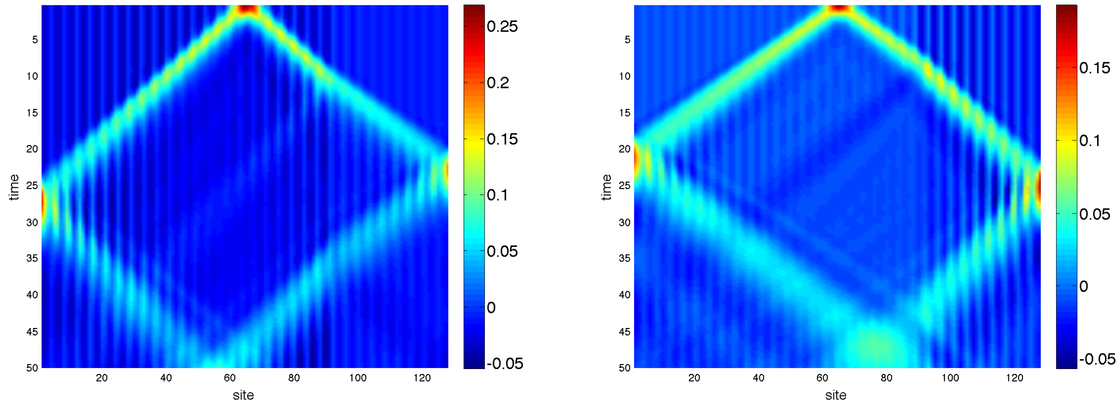

(a) Normal reflection
Charge density

(b) Andreev-like reflection
Charge density

Figure 4.43: Comparison of figure 4.41 and figure 4.42 viewed from above. The occurence of a **normal reflection** (left plot) and an **Andreev-reflection** (right plot) can clearly be seen as the charge density peak hits the interaction boundary. Also the different heights and velocities of the perturbation before and after the interaction boundary are observable.

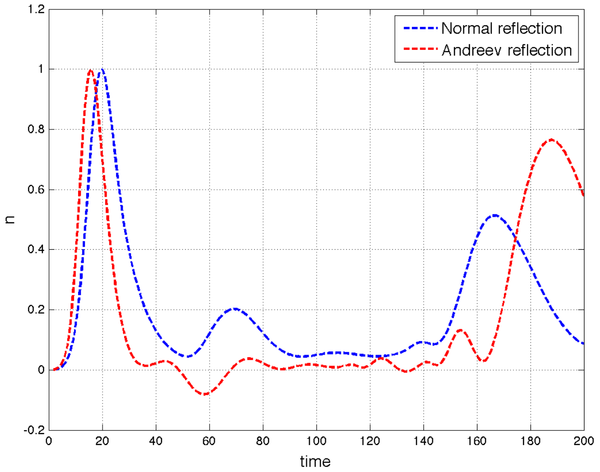

Figure 4.44: This figure shows the charge density over time averaged over sites 76 to 80 for the normal reflection ($U_L = -2.0, U_R = 0.0$; blue line) and the Andreev reflection ($U_L = 0.0, U_R = -2.0$; red line). The occurence of a normal, lower density reflection (blue line) and a reflected hole excitation corresponding to a lower particle density at timesteps $t = 12$ to $t = 22$ is obvious. The two density perturbations have slightly different velocity based on the different on-site attractions they experience. The background is substracted and the curves are normalized to the height of the maximum of the incident peak to assure a better comparability of the two different simulations.

Spin excitations

In contrast to generating a charge perturbation, one can also apply a magnetic field to the model, to generate only a spin perturbation. This is done for simulations depicted in figures 4.45 and 4.46, where the spin density is shown for this case. The amplitude of the magnetic fields is $B_0 = 0.025$ for both simulations. Results are shown in figure 4.45 and figure 4.46. As expected, only normal reflections occur. When the spin perturbation is in an attractive region, its amplitude becomes smaller over time (especially visible in figure 4.46) since in the present canonical ensemble, with equal total numbers of up and down spins it is energetically favourable for the spin excitation to spread and form bound pairs with spin zero. This can be seen in figure 4.45 on the left region and in figure 4.46 on the right, where the on-site attraction is $U = -2.0$. A comparison of both simulations in bird's-eye perspective could be found in figure 4.47, where the case with $U_L = -2.0$ and $U_R = 0.0$ is on the left respectively the one with $U_L = 0.0$ and $U_R = -2.0$ is on the right.

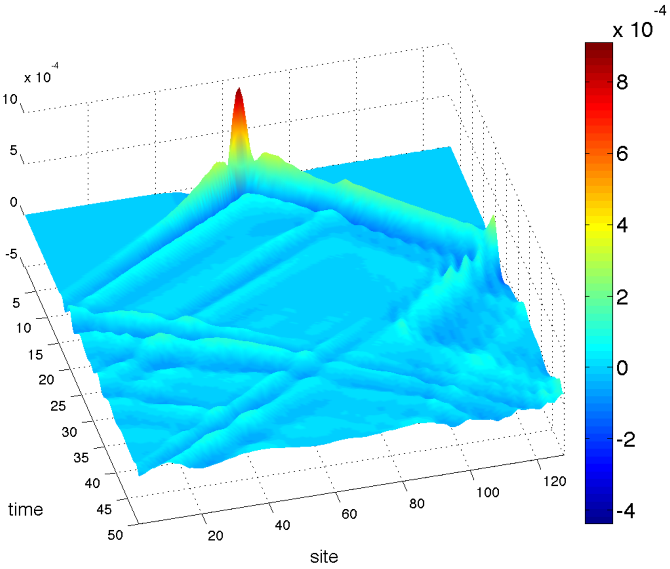

Figure 4.45: Spin density averaged over 3 sites for an attractive Hubbard model. $\mathbf{U_L}$**=-2.0**; $\mathbf{U_R = 0.0}$; $\chi = 640; L = 128; N_\uparrow = 32; N_\downarrow = 32; n = 0.5; x_B = 91; E_R = 0.0.5265; B_0 = 0.025; x_0 = 65; \sigma = 3$. The spin density decays in the attractive region on the left of the interaction boundary due to the forming of fermion pairs with no spin. In the non-interacting region on the left the spin density stays constant. The background is subtracted (see section 3.11).

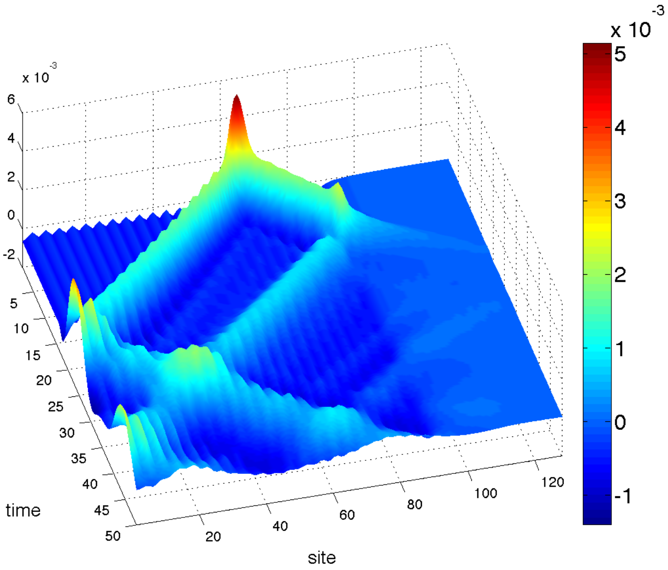

Figure 4.46: Spin density averaged over 3 sites for an attractive Hubbard model. $\mathbf{U_L{=}0.0}; \mathbf{U_R = \text{-}2.0}; \chi = 640; L = 128; N_\uparrow = 32; N_\downarrow = 32; n = 0.5; x_B = 91; E_R = -0.55; B_0 = 0.025; x_0 = 45; \sigma = 3$. In the non-interacting region on the left of the interaction boundary x_B, the spin density stays constant. As the spin perturbation crosses the interaction boundary, it decays as a consequence of pair building due to the energetically more favourable fermion pairing. The background is subtracted (see section 3.11).

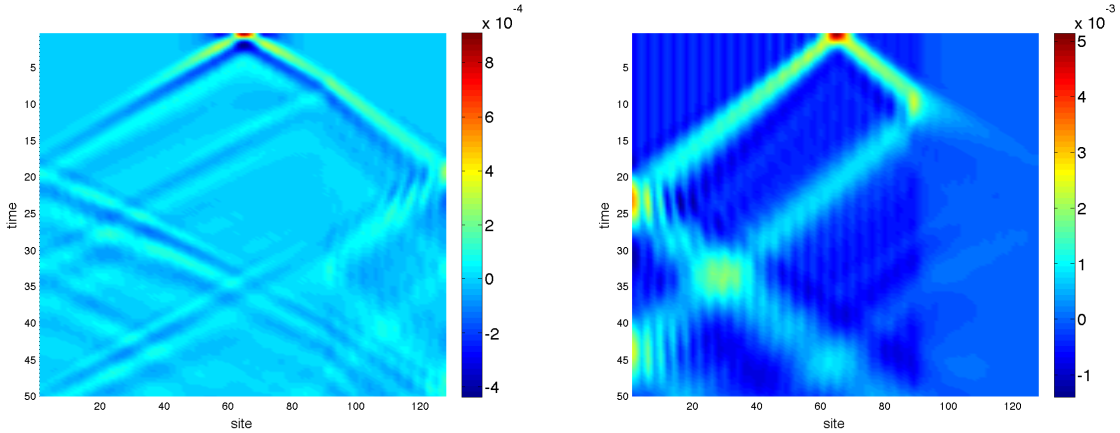

(a) $U_L = -2.0; U_R = 0.0$
Spin density

(b) $U_L = 0.0; U_R = -2.0$
Spin density

Figure 4.47: Comparison of figure 4.45 and figure 4.46 viewed from above. Note the decay of the spin perturbations in the attractive regions due to fermion pair building. The vertical scale in the left subfigure extends to 9×10^{-4} and to 5×10^{-3} in the right.

4.4.2 Different on-site attraction strengths

The appearance of Andreev reflection when a charge perturbation crosses the interaction boundary between a non-interacting region to a region with on-site attraction was shown in the section before. But what happens if the on-site attraction gets stronger?

At first, the stronger the on-site attraction gets, the stronger the pairing of fermions with opposite spin will become. This will result in a peakier charge density on the attractive side. Second, the charge velocity u_ρ will also change. A bigger on-site attraction will result in a slower propagation of the perturbation. But with higher and higher on-site interaction a third effect also occurs.

This effect becomes visible in simulations with a non-interacting Hubbard Hamiltonian $U_L = 0.0$ on the left side of the interaction boundary at $x_B = 91$ and different on-site attraction parameters U_R on the right side, which were performed varying from $U_R = -2.0$ to $U_R = -8.0$. The Hubbard model is of system size $L = 128$ and quarter-filling $n = 0.5$ with an equal number of fermions with spin up and down ($n_\uparrow = n_\downarrow = 32$). To get an equally distributed particle density over the whole system, an additional external field E_L is applied on the left side. The perturbation is only a perturbation in the charge density generated by a Gaussian-shaped electrical field of size $E_0 = -0.5$ with standard deviation $\sigma = 3.0$, which is turned off as the time evolution starts.

The results of the simulations can be found in figures 4.48 to 4.50. It can clearly be seen that the higher the attraction becomes the peakier the attractive region is, based on the pair building of the fermions. Also the different charge velocities u_ρ emerge as predicted. The mysterious third effect is, that as the attraction gets higher, the negative Andreev-reflection peak is overlayed by a positive reflection peak. Therefore no Andreev-reflection can be seen for on-site attractions greater than $U_R = -4.0$, i.e. greater than the bandwith. A possible explanation for the positive peak may be that at large attraction, the energy gain in creating a cooper pair is larger than the combined (kinetic) energies of the incoming particle and the potential reflected hole, making an immediate local Andreev reflection unfavorable, and a regular reflection more likely. Also, a bound pair is likely to exist directly at the boundary in a strongly attractive system, increasing the likelyhood of reflection. In the next section, a method is presented which makes Andreev-reflection observable even for strongly attractive Hubbard models.

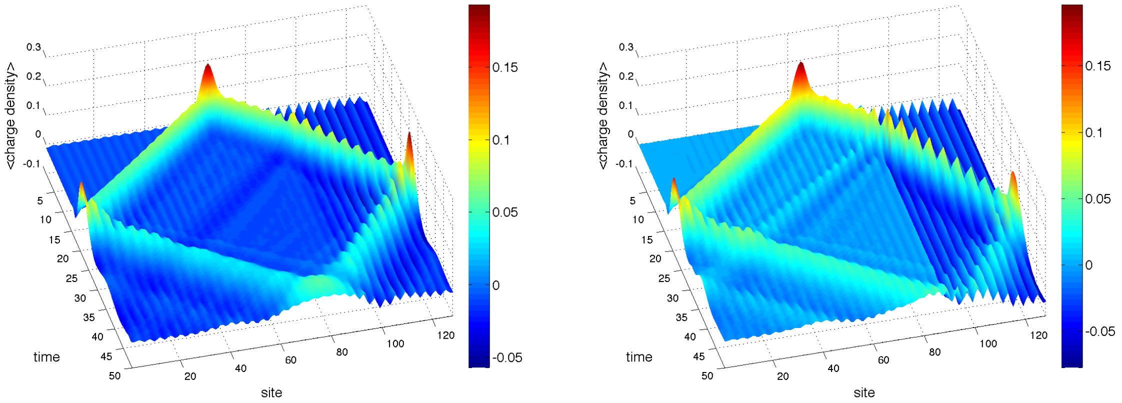

(a) $U_R = -2.0$ (b) $U_R = -4.0$

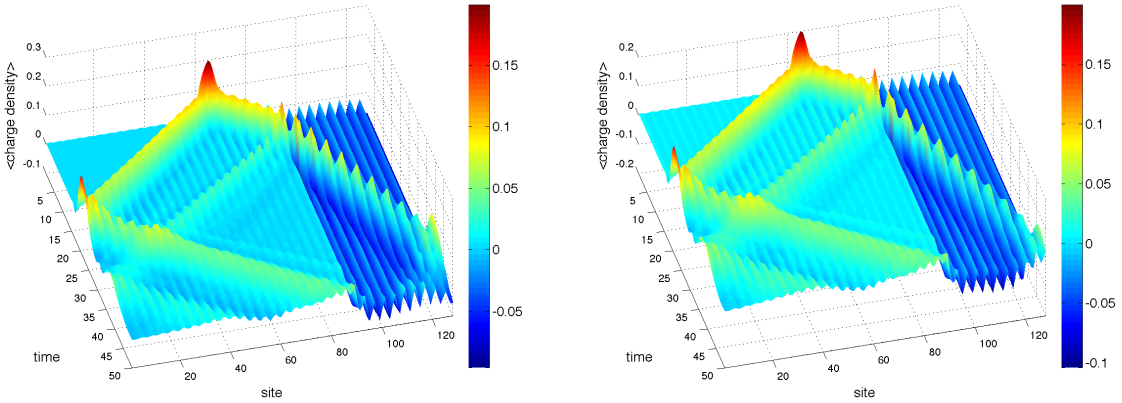

(c) $U_R = -6.0$ (d) $U_R = -8.0$

Figure 4.48: Three dimensional plot of the time evolution of a charge perturbation travelling from a non-interacting region $U_R = 0.0$ of the Hubbard Hamiltonian on the left of an interaction boundary x_B to a region with an attractive on-site interaction parameter $U_R < 0$, which varies from $U_R = -2.0$ to $U_R = -8.0$ for the single plots from the top left to the bottom right. For simulations with an on-site attraction greater than $U_R = -4.0$, no Andreev-reflection occurs. The charge density is averaged over three sites, the background has been subtracted (see section 3.11). Additional simulation parameters: $\chi = 620; N = 128; n_\uparrow = 32; n_\downarrow = 32; x_B = 91; E_0 = -0.5; B_0 = 0.0; ; x_0 = 65; \sigma = 3.0; E_L = -0.55; \tau = 0.05$.

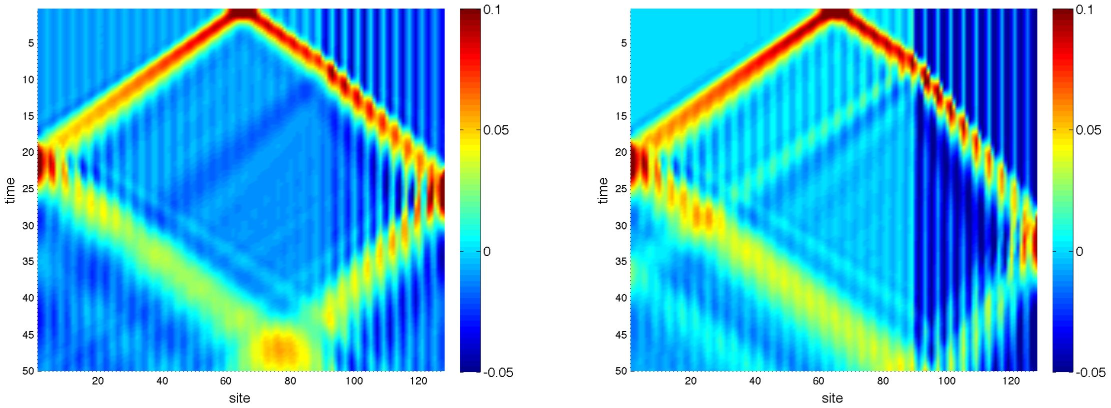

(a) $U_R = -2.0$ (b) $U_R = -4.0$

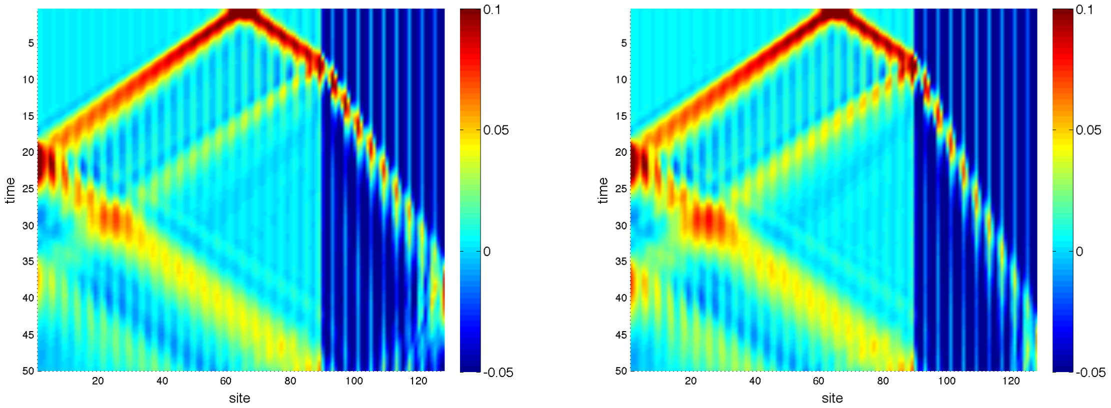

(c) $U_R = -6.0$ (d) $U_R = -8.0$

Figure 4.49: Same as figure 4.48, as 2d plots.

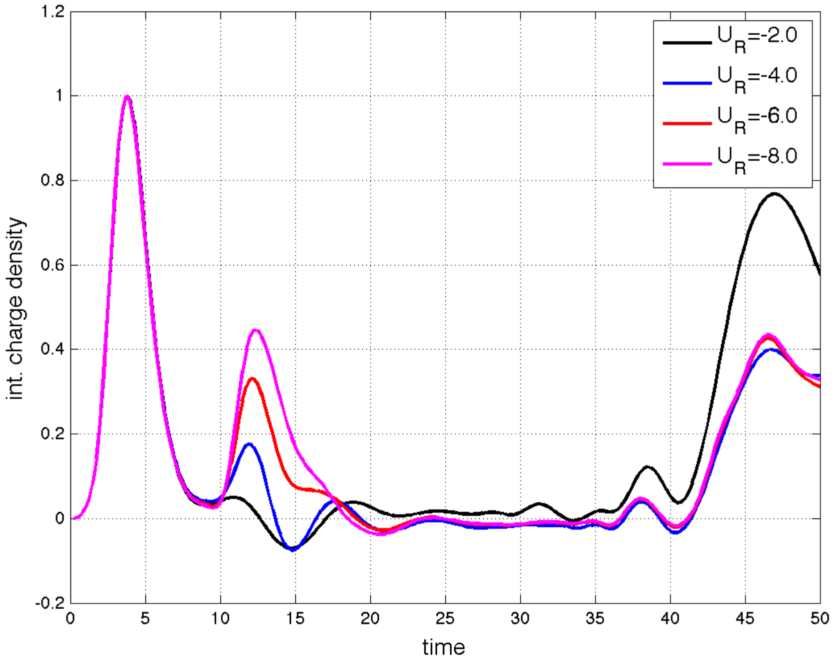

Figure 4.50: This figure shows the charge density averaged over sites 75 to 80 for the simulations shown in figures 4.48 and 4.49. For small on-site attractions ($U_R = -2.0$) Andreev-reflection is observed, but with stronger U_R the negative Andreev-reflection peak is overlapped by a positive reflection peak. The background is subtracted and the perturbations are normalized to the same initial peak height to assure better comparability of the different simulations.

4.4.3 Linear Interaction Boundary

In all former simulations the on-site repulsions respectively attractions changed abruptly. Hence the interaction boundary consisted of one site only. This sudden change of the on-site terms in the Hubbard Hamiltonian lead to strongly bound fermion pairs directly behind the interaction boundary in very attractive regions. Thus no Andreev-reflection was observed due to the reflection of the incoming fermions at these strongly bound fermion pairs. The idea is now to weaken the abrupt change of the interaction parameters by changing the on-site interaction parameter not on a single site, but linearly on a region consisting of several sites M_B. The linear change of an interaction boundary can also be found in [25]. We define a site dependent linear change parameter $F(i)$ in the following way:

$$\begin{array}{lll} F(i) = 0 & \text{for} & i < x_B \\ F(i) = \frac{(i-x_B)}{M_B} & \text{for} & x_B \leq i \leq x_B + M_B \\ F(i) = 1 & \text{for} & i > x_B + M_B \ . \end{array}$$

With the help of $F(i)$ we can easily generate a linear change in the on-site interaction parameter U_i

$$U_i = U_L + (U_R - U_L) \cdot F(i) \quad . \tag{4.7}$$

Because of the site dependence of the on-site interaction especially at the interaction boundary, we have also to apply a linear change in the external electric field E_R, which sets up approximately the same particle density on the left and the right site of x_B

$$E_i = E_R \cdot F(i) \quad . \tag{4.8}$$

Simulations concerning the charge peak propagation from a non-interacting Hubbard model ($U_L = 0.0$) to a model with strong on-site interactions ($U_R = -6.0$) have been made. These are the same interaction parameters as in figure 4.48 plot (c), where no Andreev-reflection could be observed. However the beginning of the interaction boundary was shifted to $x_B = 85$. Furthermore, because we are just interested in the effect of a linear interaction boundary on the charge density, a smaller matrix dimension of $\chi = 80$ was deployed. Results of simulations for different widths of a linear interaction boundary starting at x_B and varying from $M_B = 0$ to $M_B = 10.0$ can be found in figures 4.51 and 4.52. If the interaction boundary consists only of one site, no Andreev-reflection appears, as previously stated. But increasing the width of the interaction boundary until approximately $M_B = 6.0$, we clearly see a hole-like reflection peak as expected by the Andreev effect. Increasing the width even more, a second Andreev-reflection peak occurs. This could be ascribed to either Andreev-reflection in different regions of the interaction boundary or oscillation effects inside the boundary.

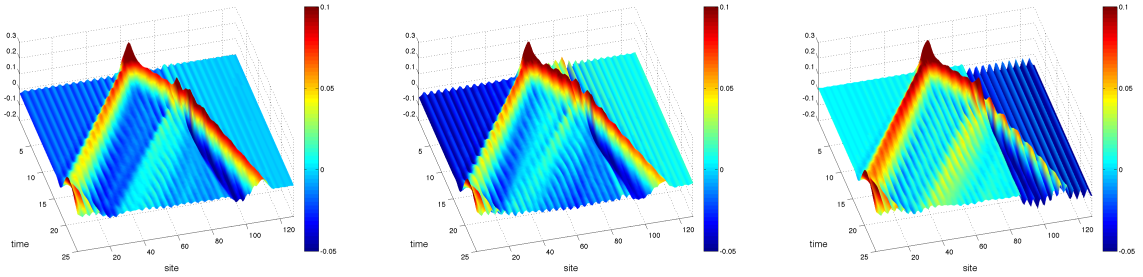

(a) $M_B = 0.0$ (b) $M_B = 1.0$ (c) $M_B = 2.0$

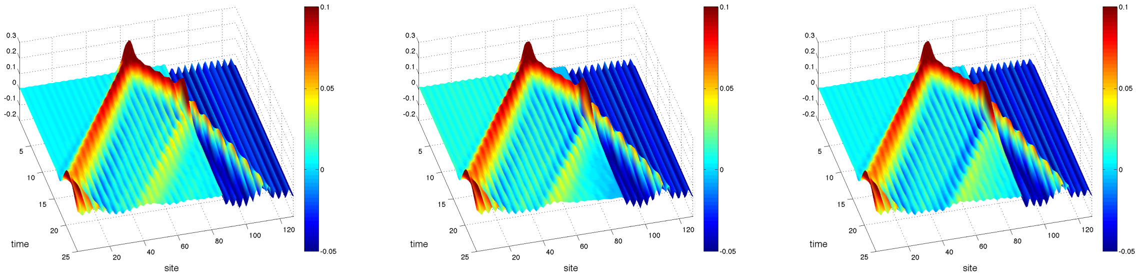

(d) $M_B = 3.0$ (e) $M_B = 4.0$ (f) $M_B = 5.0$

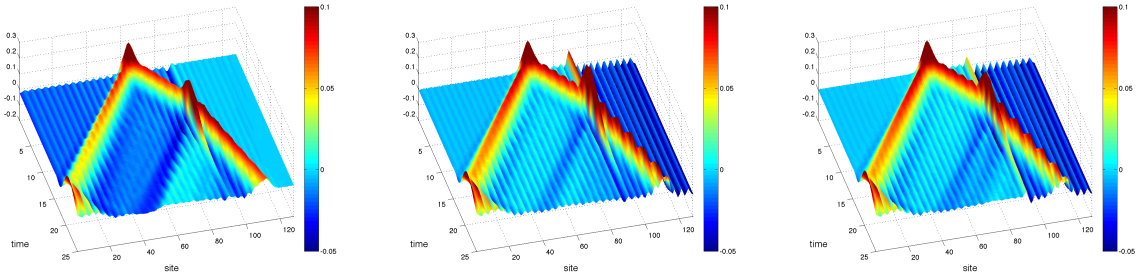

(g) $M_B = 6.0$ (h) $M_B = 7.0$ (i) $M_B = 8.0$

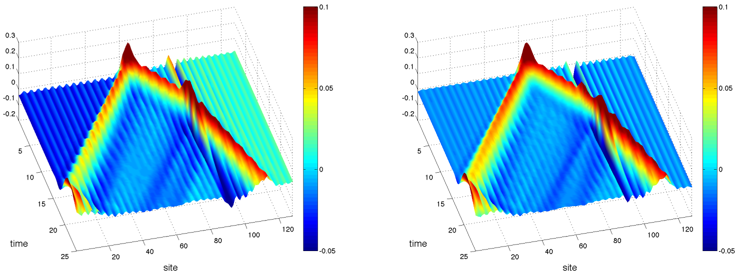

(j) $M_B = 9.0$ (k) $M_B = 10.0$

Figure 4.51: Different lengths of the linear interaction boundary M_B for the transition of a charge perturbation from a non-interacting ($U_L = 0.0$) to a strongly attractive Hubbard model ($U_R = -6.0$). The charge density is averaged over three sites, the background is subtracted (see section 3.11). Parameters for the simulation are $\chi = 80; \tau = 0.05; N = 128; n_\uparrow = 32; n_\downarrow = 32; n = 0.5; U_L = 0.0; U_R = -6.0; x_B = 86; E_R = -2.066; x_0 = 65; \sigma = 3.0; E_0 = -0.5; B_0 = 0.0$.

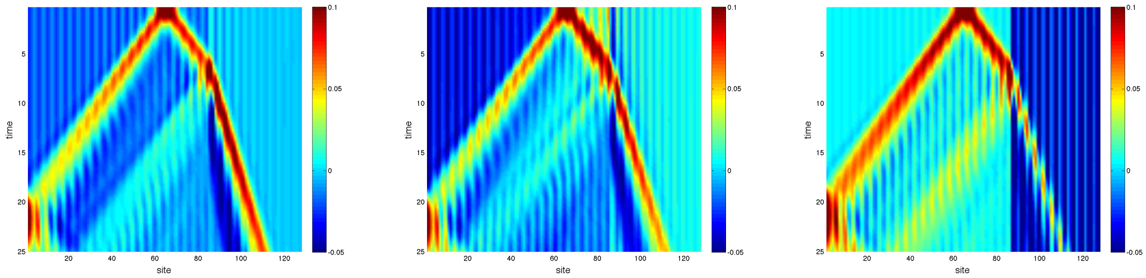

(a) $M_B = 0.0$ (b) $M_B = 1.0$ (c) $M_B = 2.0$

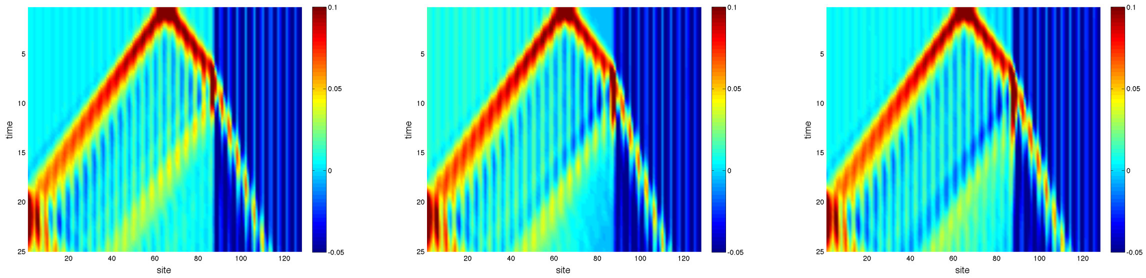

(d) $M_B = 3.0$ (e) $M_B = 4.0$ (f) $M_B = 5.0$

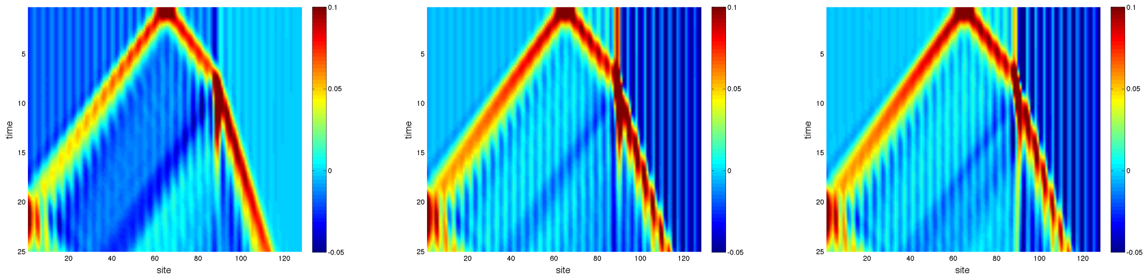

(g) $M_B = 6.0$ (h) $M_B = 7.0$ (i) $M_B = 8.0$

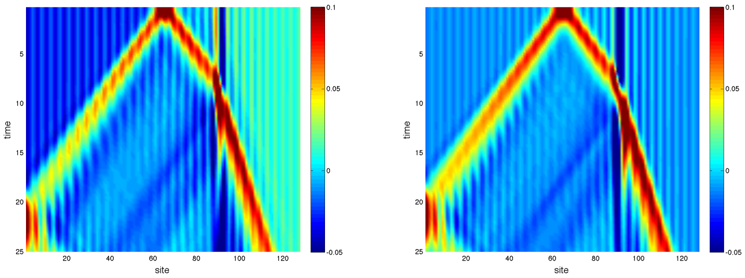

(j) $M_B = 9.0$ (k) $M_B = 10.0$

Figure 4.52: Same as figure 4.51, as 2d plots.

4.5 BCS superconductor

The last simulations are ones with an s-wave BCS superconductor Hamiltonian as found in equation 2.88. The interaction boundary is at site $x_B = 91$, where the γ-parameter of the s-wave superconductor changes from $\gamma_L = 0.0$ to $\gamma_R = 0.05$. $\gamma_L = 0.0$ represents a non-interacting region and $\gamma_R = 0.05$ is the case of a superconducting region. A perturbation is again generated by applying a Gaussian-shaped electrical field with a amplitude of $E_0 = -0.1$ and a standard deviation of $\sigma = 3.0$ at site $x_0 = 65$ at $t = 0$. At $t > 0$ the additional field is once more turned off. One difficulty arises from the fact that there is no particle conservation for this specific Hamiltonian due to the Cooper pair creation terms $\hat{c}^\dagger_{i,\uparrow}\hat{c}^\dagger_{i,\downarrow}$ and their complex conjugate. Although there is a fixed particle density of approximately $n = 0.5$ ($n_\uparrow = n_\downarrow = 32$) at the start of the ground state calculation with DMRG, particles are lost during the ground state simulation. Therefore an additional external electrical field E_{all} is applied over the whole system, to adjust a particle density of approximately $n \approx 0.25$. For the simulations of the BCS superconductor a maximum matrix dimension of $\chi = 320$ was employed.

The charge density plots averaged over three sites with subtracted background are found in figure 4.53. A three dimensional plot is on the left side, a two dimensional plot in bird's-eye perspective is located on the right. As the charge perturbation hits the interaction boundary at $x_B = 91$, Andreev-reflection is observed. Additionally, the charge density averaged over sites 70 to 75 as a function of time is depicted in figure 4.54. The reflected hole is rather big for the small applied perturbation peak. This also gets to debt because of the not constant particle density. Approximately around timestep $t \approx 20$, where the perturbation hits the interaction boundary, charge disappears in the system. The loss of the charge density can also be seen in figure 4.58 on the left side, where the total particle density is depicted over time.

The spin density is also shown in figure 4.55. Due to the fact that no external magnetic field is applied to the system, no spin density perturbation is created and therefore it is not observed in the figure, as was expected. The total spin density of the simulation is depicted in figure 4.58 on the right. Because of the conservation of the spin density in the s-wave superconductor, it should be constant over the simulation. The slight increase of the spin density in the plot showing the total spin density is likely due to numerical inaccuracies, because the magnitude of the increase is just about $\Delta N_\sigma \approx 10^{-8}$.

The entanglement entropy is represented in figures 4.56 as a three dimensional plot. The maximum of the entanglement entropy is also depicted in figure 4.57. Strangely enough the entanglement entropy decreases over simulation time. This could be ascribed to the loss of particles as the perturbation crosses the interaction boundary. The maximum truncated weight (right side of figure 4.57) also decreases around $t \approx 20$ due to this effect. One can also see an increase of the total particle density around the end of the simulation (figure 4.58 left side) after the signal at the superconducting side has completely scattered from the boundary.

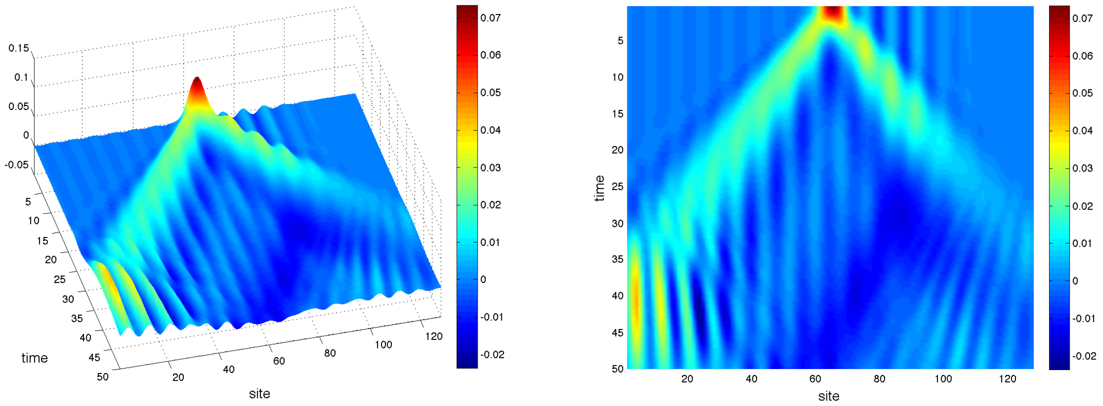

(a) Charge density

(b) Charge density

Figure 4.53: Charge density plot of the simulation of Andreev-reflection in a BCS superconductor model with an interaction boundary at site $x_B = 91$ separating areas with $\gamma_L = 0.0$ and $\gamma_R = 0.05$. Additional simulation parameters are $\chi = 320; \tau = 0.05; N = 128; n_{\uparrow} = 32; n_{\downarrow} = 32; U_L = 0.0; U_R = 0.0; E_{all} = 1.85; x_0 = 65; \sigma = 3.0; E_0 = -0.1; B_0 = 0.0$. The charge density is averaged over three sites, background is subtracted (see section 3.11).

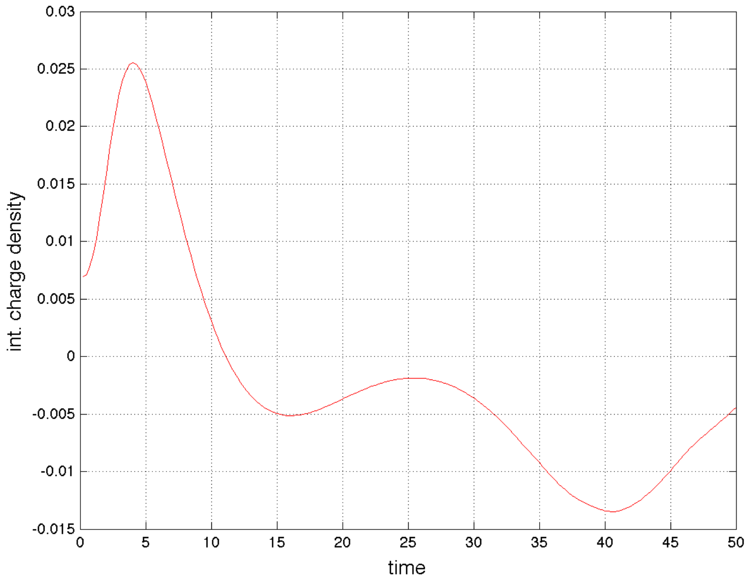

Figure 4.54: Charge density averaged over sites 70 to 75 depicted over time. A negative, hole-like peak is observed caused by Andreev-reflection.

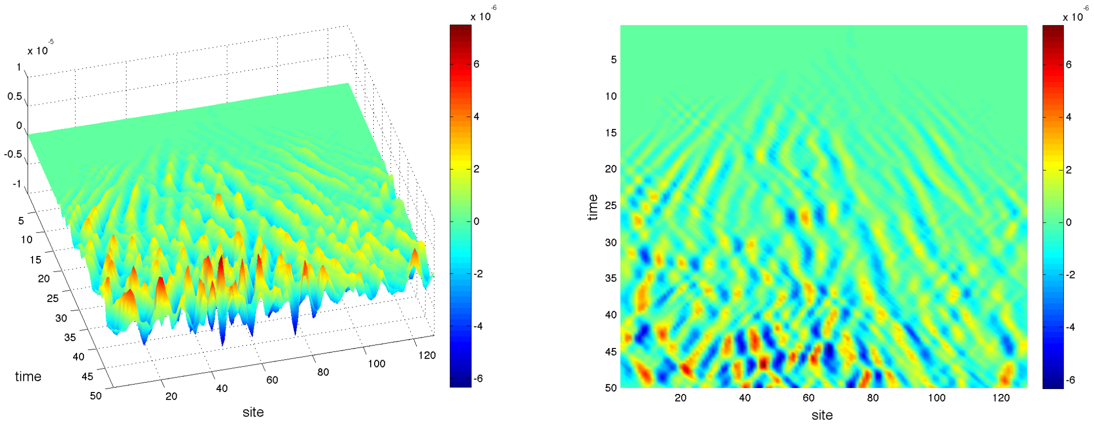

(a) Spin density (b) Spin density

Figure 4.55: Spin density plot of the simulation of the BCS superconductor model with an interaction boundary at site $x_B = 91$ separating areas with $\gamma_L = 0.0$ and $\gamma_R = 0.05$. As no spin density perturbation is applied ($B_0 = 0.0$), no spin signal can be seen. Additional simulation parameters are $\chi = 320; \tau = 0.05; N = 128; n_\uparrow = 32; n_\downarrow = 32; U_L = 0.0; U_R = 0.0; E_{all} = 1.85; x_0 = 65; \sigma = 3.0; E_0 = -0.1$. The spin density is averaged over three sites, background is subtracted (see section 3.11). The vertical scale in the subfigures extends to 7×10^{-6}.

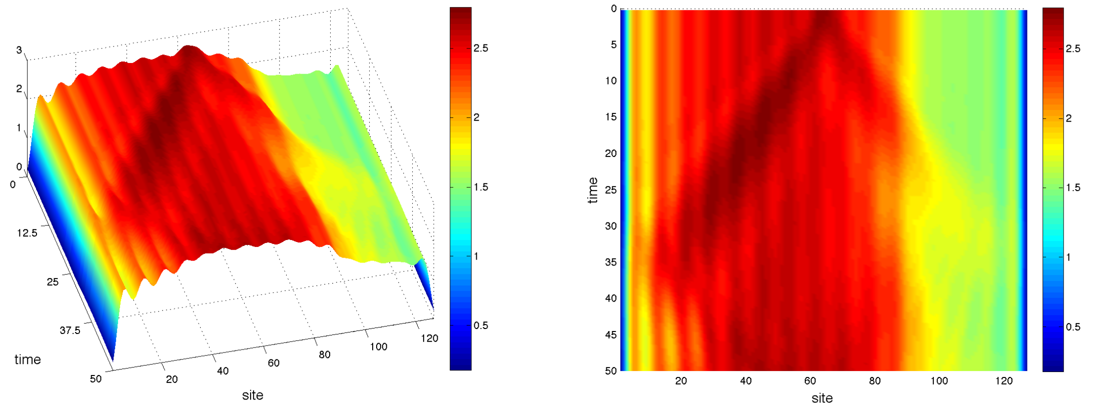

(a) Entanglement entropy (b) Entanglement Entropy

Figure 4.56: Three dimensional plot of the entanglement entropy S_N (left side) of the simulation of the BCS superconductor. On the right side S_N is represented in bird's-eye view.

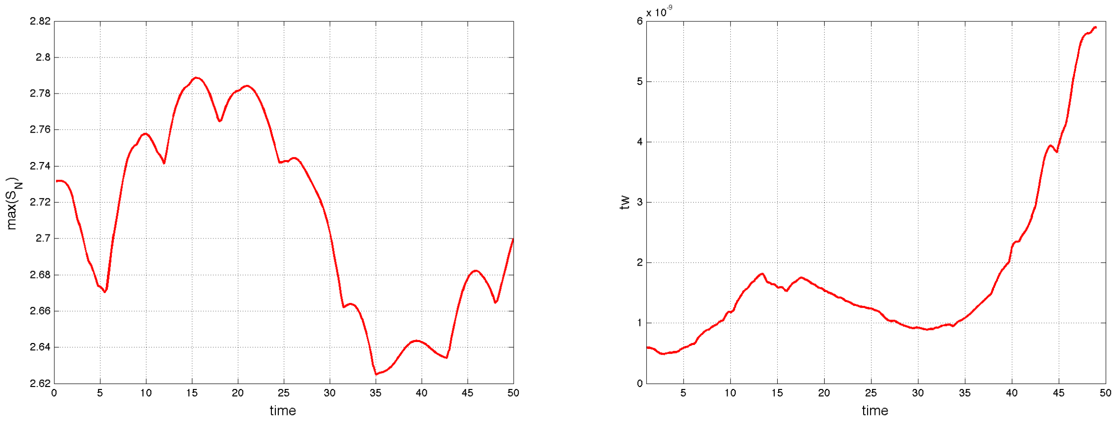

(a) Maximum S_N (b) Maximum TW

Figure 4.57: Maximum of the entanglement entropy S_N on the left and maximum of the truncated weight TW on the right of the simulation of the BCS superconductor. S_N and TW decrease around $t \approx 20$ due to particle loss as the charge perturbation hits the interaction boundary. The vertical scale in the right subfigure extends to 6×10^{-9}.

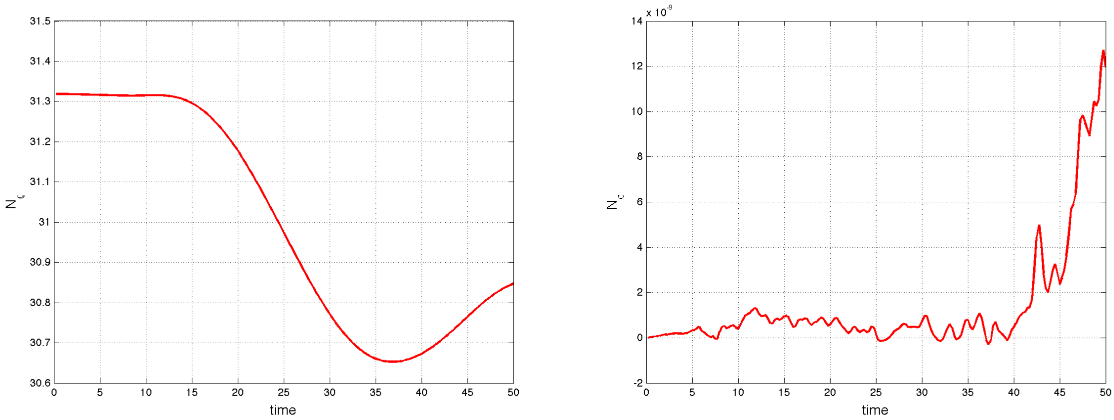

(a) Total particle density N_ρ (b) Total spin density N_σ

Figure 4.58: Total particle density $N_\rho = \sum_{i=1}^{L} (\hat{n}_{i,\uparrow} + \hat{n}_{i,\downarrow})$ on the left and total spin density $N_\sigma = \sum_{i=1}^{L} (\hat{n}_{i,\uparrow} - \hat{n}_{i,\downarrow})$ on the right depicted over time. As one can see, the spin density is preserved, except for numeric fluctuations, while the particle density varies over time as one expects for a s-wave-BCS-superconductor. The vertical scale in the right subfigure extends to 14×10^{-9}.

5 Conclusions

In this thesis, Andreev reflection was investigated. This effect occurs at metal to superconductor boundaries for transcending electrons due to the building of Cooper pairs in the superconductor, leading to a backscattered hole into the metal.

All simulations were performed in one-dimensional quantum systems with open boundary conditions.

Theoretically there are no superconductors in one dimension, but with the help of site dependent on-site attractive potentials we showed that it is possible to produce model systems that behave like there is a metal - superconductor boundary. Hence Andreev reflection emerged.

There is good reason to reduce the dimensionality of the investigated systems to one, because for one dimension the most precise and efficient methods to calculate ground states and to simulate their dynamical behavior exist. To this end the formalism of matrix product states (MPS) was introduced as a special representation of general quantum states (see chapter 3). This opened up the way for a groundstate calculation method, the density matrix renormalization group (DMRG), which can be formulated in the MPS language. For the time evolution of such MPS, the time-evolving block decimation algorithm was used.

First, before concentrating on the Andreev reflection, we started by investigating another interesting effect only observable in one dimension, the spin-charge separation (section 4.1). At non-zero on-site repulsion to $U = 4$ different velocities in the charge and in the spin channel (figures 4.4 to 4.6) occur, as theoretically predicted. Furthermore changing the band-filling n of the model from $n \approx 0.78$ down to $n \approx 0.22$ results in different velocities for the same interaction parameter $U = 4$. This is shown in figures 4.8 to 4.13. A summary of the corresponding results can be found in the tables 4.1 and 4.2. Additionally the resulting velocities were compared to calculated velocities obtained by the Bethe ansatz from literature [28]. The analytical and the simulated results show good agreement (see figure 4.14).

Then Andreev reflection was inspected first for the spinless fermion model. We saw that Andreev reflection occurs for an electron traveling from a non-interacting region to an attractive one (figure 4.16), whereas entering a repulsive region leads to normal reflection (figure 4.15).

For the second investigated system the spin degree of freedom was added leading to the Hubbard model. At first we examined a Hubbard model with on-site repulsion showing again Andreev reflection as an electron crosses the interaction boundary from a repulsive to a non-interacting region (figure 4.21). In figures 4.24 and 4.25 one can clearly see that the transmitted signal consists of electron pairs and the reflected peak is an electron hole. Simulations with different matrix dimensions χ ranging from $\chi = 80$ to $\chi = 1000$ showed that the higher the dimension, logically the smaller the truncated weight and the higher the entanglement a quantum state can carry. Results are well converged at

$\chi = 800 - 1000$. Although simulations got more precise with growing matrix dimension, Andreev reflection could already be qualitatively observed for small matrix dimensions (figures 4.28 to 4.30).

Similar simulations have been performed for an attractive Hubbard model showing again normal respectively Andreev reflection (figures 4.41 to 4.47). Simulations with different on-site attraction strengths can be found in section 4.4.2. When the step in the on-site attraction is very large and abrupt between the two different regions, the simulations showed that the Andreev reflection peak is overlayed by a positive peak possibly resulting from a strongly bounded electron pair sitting at the interaction boundary due to Friedel oscillations. This additional peak can be avoided by applying a linearly increasing interaction boundary, i.e., by varying the on-site attraction linearly over several sites instead an abrupt change (see section 4.4.3). When the interaction boundary consists of more than five sites, Andreev reflection was again clearly visible.

Finally, simulations with a more realistic superconductor model, the Bardeen-Cooper-Schrieffer (BCS) Hamiltonian were performed. Although there is no charge conservation in an s-wave BCS superconductor model, Andreev reflection also appears in this model (see section 4.5 respectively figures 4.53 to 4.58).

Acknowledgements

Everyone how has written a master thesis or similar work knows about the ordeal coming with it. The battle against an army of white pages, blearily eyes while finding a mistake in almost endless lines of code or the times, when mathematic equations would simply not reveal their secrets. Hence the support of human beings is of extreme importance to not become totally desperate and for that reason some of them are mentioned here.

First I want to thank Hans Gerd Evertz for his supervision of this thesis. He has been always helpful in his usual calm manner and every time I had a question, he was there to answer it and mixing it with funfacts and anecdotes about physicists, quantum mechanics and the beginning of computer age.

Special thanks also to my desk neighbor Martin Ganahl, whose C++ routines laid the foundation of this master thesis. Furthermore he always had time to explain me his code, quantum mechanical things or tricks to manipulate matrix product states.

I also want to thank the whole Institute of Theoretical and Computational Physics for the pleasant working atmosphere and its caring staff, where I had the honor to work for nearly three years.

To kill two birds with one stone I want to thank all my friends at once. They were always ready to distract me with endless late night discussions in woozy bars, when I needed it. Also they were a strong moral support.

Especially I want to thank my family not only for their financial support (although this is also important) but also for their moral support and letting me know, that they are proud of me.

And last but not least the greatest thanks to the person this master thesis is dedicated to, my beloved Stephanie. She always covered my back in stressful times and cheered me up, when I was down and that all in her patient and adorable way of being.

Bibliography

[1] Michael Karbach and Gerhard Müller.
"Introduction to the Bethe Ansatz I",
arXiv:cond-mat/9809162, 1998

[2] Michael Karbach, Kun Hu and Gerhard Müller.
"Introduction to the Bethe Ansatz II",
arXiv:cond-mat/9809163, 1998

[3] S. R. White.
"Density matrix formulation for quantum renormalization groups",
Phys. Rev. Lett. 69, 2863, 1992

[4] S. R. White.
"Density-matrix algorithms for quantum renormalization groups",
Phys. Rev. B 48, 10345–10356, 1993

[5] J.Eisert, M. Cramer and M.B. Plenio.
"Colloquium: Area laws for the entanglement entropy",
Rev. Mod. Phys. 82 (2010) 277, 2010

[6] S. Östlund and S. Rommer.
"Thermodynamic Limit of Density Matrix Renormalization",
Phys. Rev. Lett. 75, 3537-3540, 1995

[7] J.Dukelsky, M.A. Martin-Delgado, T. Nishino and G. Sierra.
"Equivalence of the Variational Matrix Product Method and the Density Matrix Renormalization Group applied to Spin Chains",
arXiv:cond-mat/9710310, 1997

[8] Kenneth G. Wilson.
"The renormalization group: Critical phenomena and the Kondo problem",
Rev. Mod. Phys. 47, 773-840, 1975

[9] Ulrich Schollwöck.
"The density-matrix renormalization group in the age of matrix product states",
Annals of Physics 326 (2011) 96-192, 2011

[10] Steven R. White and Adrian E. Feiguin.
"Real-Time Evolution Using the Density Matrix Renormalization Group",
Phys. Rev. Lett. 93, 076401, 2004

[11] Guifré Vidal.
"Efficient Classical Simulation of Slightly Entangled Quantum Computations",
Phys. Rev. Lett., 91(14):147902, 2003

[12] Guifré Vidal.
"Efficient simulation of one-dimensional quantum many-body systems",
Phys. Rev. Lett. 93, 040502, 2004

[13] Immanuel Bloch.
"Ultracold quantum gases in optical lattices",
Nature Physics 1, 23 - 30, 2005

[14] Immanuel Bloch, Jean Dalibard and Wilhelm Zwerger.
"Many-body physics with ultracold gases",
Rev. Mod. Phys., 80, 885 - 964, 2008

[15] Peter Pippan.
"The density matrix renormalization group and matrix product states",
Master thesis - TU Graz - Institute of Theoretical and Computational Physics, 2006

[16] Martin Jakob Ganahl.
"Simulation of Spin Transport in One Dimensional Quantum Heisenberg Spin 1/2 Systems in Real Time",
Master thesis - TU Graz - Institute of Theoretical and Computational Physics, 2010

[17] Valentin Zauner.
"Time Evolution of a Comoving Window: Simulation of Local Signals on Infinite One-Dimensional Spin Chains",
Master thesis - TU Graz - Institute of Theoretical and Computational Physics, 2011

[18] Elias Rabel.
"Numerical Time Evolution of 1D Quantum Systems",
Master thesis - TU Graz - Institute of Theoretical and Computational Physics, 2010

[19] Thierry Giamarchi.
"Quantum Physics in One Dimension",
volume 121 of International Series of Monographs on Physics, Oxford University Press, 2004

[20] X.-W. Guan.
"Algebraic Bethe ansatz for the one-dimensional Hubbard model with open boundaries",
arXiv:cond-mat/9908054, 1999

[21] P. Jordan and E. Wigner.
"Über das Paulische Äquivalenzverbot",
Zeitschrift für Physik 47, No. 9., pp. 631-651., 1928

[22] Alexander F. Andreev.
"Thermal conductivity of the intermediate state of superconductors",
Sov. Phys. JETP 19, 1964

[23] B. Pannetier and H. Courtois.
"Andreev Reflection and Proximity effect",
arXiv:cond-mat/9912024v2, 1999

[24] I. Safi and H. J. Schulz.
"Transport in an inhomogeneous interacting one-dimensional system",
Phys. Rev. B, 52(24):17040-17043, 1995

[25] A. Daley, P. Zoller and B.Trauzettel.
"Andreev-Like reflections with cold atoms",
Phys. Rev. Lett., 100(11):110404, 2008

[26] Hans Gerd Evertz.
"Analytische Behandlung von Vielteilchenproblemen: Hubbard- und Heisenbergmodell",
Lecture Notes - TU Graz - Institute of Theoretical and Computational Physics, 2004

[27] H. J. Schulz.
"Fermi liquids and non-Fermi liquids",
arXiv:cond-mat/9503150, 1995

[28] H.J. Schulz.
"Interacting fermions in one dimension: from weak to strong correlation",
arXiv:cond-mat/9302006, 1993

[29] Thierry Giamarchi and B. Sriram Shastry.
"Persistent currents in a one-dimensional ring for a disordered Hubbard model",
Phys. Rev. B, 51(16):10915-10922, 1995

[30] I. Safi and H. J. Schulz.
"Interacting electrons with spin in a one-dimensional dirty wire connected to leads",
Phys. Rev. B, 59(4):3040-3059, Jan 1999

[31] Essler, Fabian H. L., et al.
"The One-Dimensional Hubbard Model",
1st ed. Cambridge: Cambridge University Press, 2005.

[32] W. Meissner and R. Ochsenfeld.
"Ein neuer Effekt bei Eintritt der Supraleitfähigkeit.",
Naturwissenschaften, 21(787), 1933

[33] Emanuel Maxwell.
"The isotope effect in the superconductivity of mercury",
Phys. Rev., 78(4):477, 1950

[34] C.A. Reynolds, B. Serin, W.H. Wright and L.B. Nesbitt.
"Superconductivity of isotopes of mercury",
Phys. Rev., 78(4):487, 1950

[35] J. Bardeen, L. N. Cooper and J. R. Schrieffer.
"Microscopic Theory of Superconductivity" ,
Phys. Rev. 108, 1175-1204, 1957

[36] Nikolai Bogoliubov.
"On the theory of superfluidity",
J. Phys. (USSR), 11. p. 23, 1947

[37] F. Verstraete, J.I. Cirac and V. Murg.
"Matrix Product States, Projected Entangled Pair States, and variational renormalization group methods for quantum spin systems",
arXiv:quant-ph/0907.2796v1, 2009

[38] P. Pippan, S.R. White and H.G. Evertz.
"Efficient matrix-product state method for periodic boundary conditions",
Phys. Rev. B, 81, 081103, 2010

[39] S. Rommer and S. Östlund.
"Class of ansatz wave functions for one-dimensional spin systems and their relation to the density matrix renormalization group",
Phys. Rev. B 55, 2164-2181, 1997

[40] I. Omelyan, I. Mryglod, R. Folk.
"Optimized Forest-Ruth- and Suzuki-like algorithms for integration of motion in many-body systems",
arXiv:cond-mat/0110585, 2001

[41] Tobias Ulbricht and Peter Schmitteckert.
"Is spin-charge separation observable in a transport experiment?",
EPL (Europhysics Letters), 86(5):57006, 2009

[42] Corinna Kollath and Ulrich Schollwöck.
"Cold Fermi gases: a new perspective on spin-charge seperation",
New Journal of Physics, 8 (2006) 220, 2006

[43] C. Kollath, U. Schollwöck, and W. Zwerger.
"Spin-charge separation in cold fermi gases: A real time analysis",
Phys. Rev. Lett., 95(17):176401, 2005